Magnetic Noise Sensing and Nanomechanical Transducers for Spin Qubits

Magnetic Noise Sensing and Nanomechanical Transducers for Spin Qubits

a dissertation presented
by
Arthur Dov Safira
to
The Department of Physics

in partial fulfillment of the requirements
for the degree of
Doctor of Philosophy
in the subject of
Physics

Harvard University
Cambridge, Massachusetts
September 2018

Thesis advisor: Professor Mikhail Lukin Arthur Dov Safira

Magnetic Noise Sensing and Nanomechanical Transducers for Spin Qubits

Abstract

Nitrogen-Vacancy (NV) centers have shown great promise as magnetometers and as quantum information processors. NV centers have proven to be very well-isolated and extremely localized quantum systems that couple naturally to external magnetic fields. In this thesis, that sensitivity to magnetic fields and otherwise long relaxation time is utilized as a probe near other magnetic-field-generating sources to gain insight into the underlying physics within those sources. Specifically, we show how the NV center can be used to observe a change in the Johnson magnetic field noise outside of conductors due to variations in the electron mean free path within the metal.

Furthermore, great progress in engineering two-qubit gates between NV centers is also demonstrated. One avenue towards such a spin-spin coupling is to properly engineer an interaction between each separate NV with a mechanical oscillator; the resulting dynamics give rise to an effective interaction between NV centers. In light of the NV center's natural coupling to magnetic fields, one method to couple NV centers and resonators is through magnetically functionalizing the resonators. In this thesis, we demonstrate the engineering of very well-isolated (high quality factor)

magnetically-functionalized resonators ($Q > 4 \times 10^5$), and also reach new highs in magnetic field gradients in such systems integrated with NV centers, both crucial parameters in the final fidelity of two-qubit gates.

Separately, initial studies on a new potential quantum platform is presented: that of levitated magnets over superconductors. Such systems have the potential to have very high quality factors, and can be used as novel sensors, a new transducer for NV center entanglement, and to test fundamental gravitational quantum theories. Experimental progress reported here indicates a good understanding of the underlying levitation physics as well as motional spectra, quality factors, and motional nonlinearities.

Finally, spin-off work in developing a strong software interface for the lab, pylabcontrol, is also discussed. Adoption of such software can make a big impact within the community, in terms of reducing redundant software development, make experimental work more repeatable, and improving general quality of life within the general experimental physics community.‘

Contents

1 Introduction 1
1.1 The Nitrogen-Vacancy Center . . . 2
1.1.1 Mechanical Resonators . . . 3
1.1.2 Levitating Micromagnets . . . 5
1.2 The NV center for Magnetic Field Sensing . . . 5
1.2.1 Electron Spin Resonance . . . 6
1.2.2 AC Pulse-Sequence Magnetometry . . . 7
1.2.2.1 Hahn Echo . . . 7
1.2.2.2 XY-8 pulse sequences . . . 8
1.2.3 Spin Relaxation Noise Magnetometry . . . 9
1.3 Future Applications and Outlook . . . 9

2 Johnson Noise Near Metal Films 12
2.1 Introduction . . . 13
2.2 Experimental Results . . . 13
2.3 SOM . . . 25
2.3.1 Experimental materials and methods . . . 25
2.3.1.1 Averaging, number of points, and wait times for relaxation measurements . . . 26
2.3.2 Fabrication and metrology . . . 26
2.3.2.1 Single-crystal silver deposition and characterization . . . 26
2.3.2.2 Characterization of silver film grain size . . . 27
2.3.2.3 Diamond surface characterization . . . 29
2.3.2.4 Fabrication of devices for temperature-dependent studies 30
2.3.3 Johnson Noise Theory . . . 32
2.3.3.1 Spin decay rate near a conducting metallic half-space . . . 32
2.3.3.2 Reflection coefficients . . . 33
2.3.3.3 Quasi-static approximation . . . 34
2.3.3.4 NV magnetic dipole orientation . . . 35
2.3.3.5 Three-level system dynamics . . . 36
2.3.3.6 Non-local corrections to the decay rate . . . 36
2.3.4 Spectral dependance of Johnson noise . . . 38
2.3.5 NV T_1 statistics . . . 39

2.3.5.1 Extraction of relaxation rates and distances under polycrystalline silver . . . 40
2.3.5.2 NVs under single-crystal silver . . . 43

3 Towards Strong Mechanics-NV Interactions **46**
3.1 Introduction . . . 47
3.2 Experiment . . . 48
3.3 Setup . . . 48
3.4 High Quality Factor Loaded Resonators . . . 50
3.5 Poor Gradients from Resonators with Deposited Cobalt magnets . . . 52
3.6 Improved Gradients with Resonators with Neodynium microbeads . . . 54
3.7 Future Work and Conclusions . . . 57

4 Initial Studies into Levitated Micromagnets **58**
4.1 Introduction . . . 59
4.2 Theory . . . 60
4.2.1 Method of Frozen Images . . . 60
4.2.2 Potential . . . 62
4.2.3 Properties . . . 63
4.3 Experiment . . . 64
4.3.1 Setup . . . 64
4.3.2 Analysis . . . 66
4.4 Future Work and Conclusion . . . 67

5 pylabcontrol: Laboratory Equipment Control for Scientific Experiments **69**
5.1 Introduction . . . 70
5.2 Philosophy . . . 71
5.2.1 Smart Default Behavior . . . 71
5.2.2 Repeatability . . . 72
5.2.3 Ease of Use . . . 73
5.3 Prior Work . . . 74
5.4 Installation . . . 74
5.5 Usage . . . 75
5.5.1 Typical lab workflow . . . 75
5.5.2 Using pylabcontrol: Instruments . . . 75
5.5.2.1 Using pylabcontrol: Parameters . . . 77
5.5.3 Scripts . . . 78
5.5.3.1 optional Script uses . . . 79
5.5.4 Data analysis . . . 79
5.6 GUI . . . 80

5.6.1 Advanced Features . . . 82
5.7 Future Work . . . 83
5.8 Conclusion . . . 84

Appendix A Appendix A: Cleanroom Recipes **85**
A.1 Patterned Silicon Nitride Membranes . . . 86
A.1.1 Resist Spinning . . . 86
A.1.2 Exposure . . . 88
A.1.3 Development . . . 89
A.1.4 SiN Etching . . . 89
A.1.5 Resist Removal . . . 90
A.1.5.1 Normal Removal (Remover-PG) . . . 90
A.1.5.2 Aggressive Removal (Piranha) . . . 90
A.1.6 Second Run . . . 91
A.1.7 Si Etching in KOH . . . 91
A.2 Silicon Nitride Doubly-Clamped Beams . . . 93
A.3 Resonator Magnet Integration . . . 94
A.4 Material Ramp . . . 94

Appendix B Appendix B: In-depth Theoretical Derivation of Johnson Noise from Material Half-spaces **96**
B.1 Overview . . . 97
B.2 Fluctuation-Dissipation Theorem . . . 97
B.3 A Glimpse of The Electromagnetic Green's Function . . . 100
B.4 Putting it All Together . . . 102
B.5 The Electromagnetic Green's Function . . . 103
B.6 Green's Function Primer . . . 103
B.7 Electric Dipole to Magnetic dipole . . . 114
B.8 The Loss Rate . . . 115
B.9 Master Equation . . . 117
B.10 Spin Relaxation Rate . . . 118
B.11 The loss rate . . . 119

Appendix C Appendix C: In-Depth Theory of Spin-Spin Interactions via Mechanical Resonators **127**
C.1 Theory . . . 128
C.1.1 NV-NV Entanglement, No Noise . . . 128
C.1.2 NV-NV Entanglement, With Unwanted External Interactions . . . 129

List of Figures

2.1 **Probing Johnson noise with single spin qubits. (A)** The thermally induced motion of electrons in silver generates fluctuating magnetic fields ($\vec{\mathbf{B}}$), which are detected using the spin of a single NV. The NV is polarized and read out through the back side of the diamond. **(B)** The NV spin is polarized into the $|m_s = 0\rangle$ state using a green laser pulse. Spin relaxation into the $|m_s = \pm 1\rangle$ states is induced by magnetic field noise at ∼2.88 GHz. After wait time τ the population left in $|0\rangle$ is read out by spin-dependent fluorescence. All measurements shown were performed at low magnetic fields ($\Delta \gg g\mu_B B_{||}/\hbar$). **(C)** Spin relaxation data for the same single shallow implant NV before silver deposition (open blue squares), with silver deposited (red circles), and after the silver has been removed (open blue triangles). **(D)** Spin relaxation for a single NV close to a silver film prepared in the $|m_s = 0\rangle$ state (red circles), and in the $|m_s = -1\rangle$ state (open orange circles). **(Inset)** Spin relaxation for a single native NV in bulk diamond in the $|m_s = 0\rangle$ state (blue circles), and in the $|m_s = -1\rangle$ state (open light blue circles). 16

2.2 **Distance dependence of NV relaxation close to silver. (A)** A gradual SiO_2 ramp (slope of ∼.2 nm/micron) is grown on the diamond surface, followed by a 60 nm silver (Ag) film. **(B)** The NV relaxation rate is measured as a function of position along the ramp, which is then converted to distance to the film. At each point 5-10 NV centers are measured, and the minimum rate measured is plotted (red circles). The red dashed line shows the expected relaxation rate with no free parameters after accounting for the finite silver film thickness. **(Inset)** Thickness of the ramp as a function of lateral position along the diamond sample (blue curve). The red crosses correspond to the positions along the sample where the measurements were taken. 18

2.3 **Temperature dependence of NV relaxation close to polycrystalline silver. (A)** The measured relaxation rate T_1 of a single NV spin under a polycrystalline silver film as a function of temperature (red data points). The conductivity of the silver film as a function of temperature shown in **B** is included in a fit to Eq. 2, with the distance to the film as the single free parameter (red dashed line). The extracted distance is 31±1 nm. **(B)** The conductivity of the 100 nm thick polycrystalline silver film deposited on the diamond surface is measured as a function of temperature. **(Inset)** Grain boundaries within the polycrystalline silver film, imaged using electron backscatter diffraction (EBSD). The average grain diameter is 140 nm, with a standard deviation of 80 nm. 19

2.4 **Temperature dependence of NV relaxation close to single-crystal silver. (A)** Measured conductivity of single-crystal (blue curve) and polycrystalline (red curve, same as Fig. 3B) silver as a function of temperature. **(Inset)** Electron backscatter diffraction image of the single-crystal silver film showing no grain boundaries, and the observed diffraction pattern. **(B)** Relaxation of a single NV spin under single-crystal silver as a function of temperature (blue squares). Eq. 2 is fit to the data from 200-295 K (blue dashed line). A non-local model is fit to the data (blue solid line), the extracted distance between the NV and the silver surface is 36±1 nm. **(C)** Cartoon illustrating the relevant limits, where the noise is dominated by diffusive electron motion (left, $l \ll d$), and ballistic motion (right, $l \gg d$). **(D)** The same data as **B** was taken for 23 NVs at varying distances from the film. The T_1 of each NV at 103 K (top) and 27 K (bottom) is plotted against the extracted depth (blue triangles). The non-local model (solid colored lines) saturates at a finite lifetime determined by Eq. 3 (bottom, dashed black line), while the local model does not (dashed colored lines). 24

2.5 Single-crystal AFM and TEM characterization. **(A)** AFM image of a typical single-crystal silver surface grown for this work. The scan indicates a ∼1 nm RMS roughness over a 4 μm × 4 μm range, thus allowing for good diamond-silver contact. **(B)** A TEM image of a typical silver sample, where the growth direction is from left to right and the silver is capped with a titanium capping layer resulting in the brighter region on the right of the image. The image reveals single-crystallinity of the silver up to the surface. 28

2.6 **Single-crystal and polycrystalline silver Inverse Pole Figures (IPF).** Using electron backscatter diffraction imaging in an SEM, we image the local crystal orientations of our silver films, and measure the average grain size. **(A)** Data for a 2 μm $\times$ 2 μm area of evaporated silver on 5 nm of SiO_2 on (100) silicon. The crystal variations along the direction perpendicular to the sample can cause mixed diffraction signals, and the crystal orientation fits in those regions have low confidence and result in an IPF with unphysical pixel-to-pixel variations in the crystal orientation (left region of image). **(B)** EBSD data for the same size region for single-crystal silver. No grain boundaries are visible. **(C)** Color scale conversion legend to map color to silver crystal orientation. 29

2.7 AFM and profilometer characterization of diamond surface. **(A)** An AFM image of the surface of the diamond used for the single-crystal silver measurements. The scan indicates a $\sim$1 nm RMS roughness over a 10 μm $\times$ 10 μm range, thus allowing for good diamond-silver contact. **(B)** A profilometer scan of the surface of the diamond sample. 30

2.8 Johnson noise spectral dependance. We apply static magnetic fields to shift the NV spin transition frequencies. When polarized in the $|\pm1\rangle$ state, the relaxation rate of the NV center is sensitive to the magnetic field noise at the frequency $\omega_\pm$ given by Eq. S26. The red triangle corresponds to the decay rate extracted from the data shown in Fig. 1D of the main text. . . . 40

2.9 NV decay rates near single-crystal silver with non-local fits. **(A)** Data for an NV in the same region (region A) as the NV in Figure 4B of the main text. The extracted distance from the fit is $z = 33 \pm 2$ nm. This was the smallest extracted distance we observed for the single-crystal silver measurements. **(B)** Data for an NV in region B, where we expect NVs to be farther away from the silver film than in region A. The extracted distance from the fit is $z = 88 \pm 2$ nm **(C)** Data for an NV in region C, where we expect the largest separation between the NV and the metal film. The extracted distance is $z = 141 \pm 4$ nm. **(D)** The same data as in Figure 4D, measured T_1 versus extracted distance for two temperatures, 103 K (top) and 27 K (bottom), color coded by sample region (blue triangles in region A, pink squares in region B, gray circles in region C). 44

3.1 Diamond-Nanomechanics Device Fabrication Process. (a) First, a simple photolithography step creates a gold microwave coplanar waveguide on a silicon nitride-on-silicon substrate. (b) Electron-beam lithography is used to define long beams in the silicon nitride near the coplanar waveguide centerpin. These beams are underetched using a silicon KOH etch. (c) Next, a a FIB with manipulator is used to place down a spherical bead onto the beam; the bead is either stuck electrostatically or via a localized platinum deposition. In initial studies, stencil lithography was used to deposit metal via e-beam lithography (see Appendix). (d) A diamond is placed on top of the entire area with NV's close to its bottom surface. The entire device is wirebonded onto a separate PCB. 49
3.2 Resonator Quality Factors with and without Magnet Load. Under cryogenic conditions and with a nanomagnet placed in the center, the double-clamped silicon nitride resonators exhibited large quality factors ($> 4 \times 10^5$). The above resonator is one that was thicker than necessary for the final experiment, and the quality factor may improve more upon using thinner quality factor resonators. 51
3.3 Poor Gradients from Cobalt Nanomagnets. (top-left) A confocal fluoresence image of the diamond over a magnetic bar. Arrows indicate the path the diamond makes as it is pushed on the surface of the device. (top-right) Exampe ESR spectrum of NV's tracked as they are passed over the magnetic bar. (bottom-left) Measured magnetic fields of NV's along their trajectories. (bottom-right) Inferred Magnetic field gradients along the given trajectories. The Magnetic field gradients do not exceed 500 T/m. 53
3.4 **Measuring the coupling between NV's and resonator via Pulse Sequences**. (top) An XY-8 pulse sequence is used to filter most frequencies of external magnetic field; in the case when the pulses are in unison with an external field, the resulting phase building results in spin contrast. (bottom) The resulting spin contrast is fit to a model indicating a high (4×10^3 T/m) magnetic field gradient. 55
3.5 Measuring the coupling between diamond and resonator with an ensemble diamond. (a) A spherical micromagnet with diamond of 2.2 um is on a mechanical resonator. The blue outline indicates the positions along which ESR is measured (b) The resulting ESR scan. (c) The measured magnetic field field and magnetic field gradient as a function from distance to center, including dipole fit. (d) An example ESR spectrum. 56

4.1 Method of Frozen Images. To model a dipole above a type-II superconductor, two image dipoles are used to derive the response field in the upper half space. 61

4.2 Example Trapping Potential for a Magnetic Dipole over a Type-II superconductor. The plot was derived assuming a cooldown height of 120 um. . . 63
4.3 Levitated Magnet Setup. A single micron-scale bead is placed on a silicon nitride membrane. After the YBCO is cooled, the membrane is lowered until the bead comes off the membrane and is levitated and pinned. A microscope objective is mounted above the sample and data is taken with a camera. Notably, the smooth, sloped sides the membrane structure allow for imagining mirror images of the bead, allowing z-mode imaging. 65
4.4 Levitated Magnet Motional Mode Spectrum. Applying a Fourier transform to the random motion of the bead reveals a number of motional modes, identified by later driving at these frequencies and studying the resulting video data. 67
4.5 Levitated Magnet Z-mode Anharmonicity. The z-mode motion of the bead is found to have an amplitude-dependent frequency, consistent with the frozen image dipole model. 68

5.1 The pylabcontrol GUI. (top left) The Script, Probes. Instruments, and Datasets pane. Here, parameters of Scripts and Instruments can be quickly changed, and datasets can be looked at later. (bottom left) History and GUI settings. The History contains all output from the log, and GUI settings include paths for where scripts and current GUI settings are saved. (top right, bottom right) Plotting areas for scripts and datasets, including basic interactive tools (magnification, panning). 81

A.1 **Magnet Fabrication on Mechanical Resonators** A stencil mask is carefully placed using UV curing glue above the mechanical resonators. Metal is evaporated onto the mask and exposed resonator area. 94
A.2 **Silica ramp fabrication procedure. (A,B)** Following a 5 nm uniform CVD pre-deposition of SiO_2, a silica layer of gradually increasing thickness is fabricated on a diamond sample by placing a raised coverslip (raised $\sim$ 300 μm) over the diamond, and growing the silica layer via an anisotropic CVD process. **(C)** A final 60 nm layer of silver is deposited on the ramp, so that NV centers at different points along the diamond are different distances away from the silver film. 95

List of Tables

2.1 Number of averages, number of measured points, and range of evenly spaced wait times for the T_1 measurements presented in each figure. 26
2.2 T_1 statistics for 16 of the NVs shown in Figure 4 of the main text (corresponding to the blue triangles in Figure 2.9D), in the absence of silver. 41
2.3 Mean optical excited state lifetimes by spatial region for the NVs show in Figure 4 of the main text and Figure 2.9D. 45

Acknowledgments

Those who regularly interact with me know that few things seemingly phase me in my day-to-day life. Part of that is just who I am, but a big part of that is also the people in my life.

In how much I've changed throughout grad school, I undoubtedly have my sister, Ariela, to thank the most. Somehow, we are very different and very alike in all the ways you want someone to be in your life: alike in ability to level with one another, get points across, and just have conversation, while different in our passions, views, and execution. Most PhD students find themselves in a social and psychological bubble that can often lead to unhealthy levels of distress; Ariela is that person in my life that reminds me the stakes are all exaggerated and there are far more important things to spend emotional energy on. I hope I can do an even better job of it after graduate school, but for my level of maturity within graduate school, I have her to thank.

Next, I have my girlfriend Nicole to thank, and for something totally different: Nicole has had to deal so much with me over the years. She has helped me through situations that were only really tough because of poor decisions I've made, she's made career and location changes for me, and she's even partially responsible for my per-

sonal career change, with which she will move once again. I don't consider this a "normal" amount of commitment to our relationship, and she deserves an endless amount of credit on that end. Because of her, a large portion of my personal life was mostly "working fine", which was likely a hugely necessary crutch during these years of my life (and probably in many years to come). I also want to mention how much of an embodiment of love she is, too: in my day-to-day life in which so many people regularly have high expectations, it genuinely helps so much to go home to someone who doesn't care about all that.

As a researcher, I have a great many people throughout Harvard to thank. Even among PhD programs (around the world), the underlying culture within Harvard (and perhaps especially the Lukin group) is one that has a relatively a high standard of understanding and skill. Because of that, I feel my combination of knowledge, intuition, and abilities are unique to me in a way that I'm not sure another person would exist with them. My advisor, Misha, has a lot to be thanked for in that vein: he is second-to-none in academic expectation. I have been lucky in my PhD in that I have had a lot of freedom — more than the average PhD student — because of the financial and research support Misha has given the projects I was on. I'm not sure this sort of PhD exists anywhere else, honestly. Misha deserves a lot of credit for it.

During my first few years in graduate school I worked with Shimon; I have him to thank for most of my NV fundamentals as well as most of my hands-on optics skills. That was readily apparent when Aaron joined the lab a few years later, when I tried

to pass those down. Aaron has gone through a lot with me, including a night of coding in which we both got sick (a “hackathon”); I need to thank him for tolerating me. Jan also deserves credit for tolerating my decisions over the years, for seemingly having an unlimited patience, and how hard he can work on just faith that certain projects will work out. Emma deserves credit for her determination in lab, and how often she rightfully questions the motivations behind our actions in lab. I’ve learned a whole lot from those I work closely with =).

The whole of the Lukin group deserves praise of the great depth of knowledge that exists within the group, and just how easy it was to learn something new day in, day out. The technical support that exists at Harvard — namely, Stan and Jim — have also taught me quite a lot (from knowing nearly nothing).

My parents both weren’t wealthy or particularly educated, and there’s something to be said about how much of an outlier I am within my family. It would be wrong not to point out their influence in my life, and what a strange mix of them I’ve ended up becoming. I have my mother’s strict sense of accomplishment and my father’s general attitude to thank for who I am today.

Lastly, many who know me know that I do my best to preserve the social relationships in my life; my PhD would have been different if not for the relationships in my life. I thank every person who I got to know just a little better during graduate school.

Citations to previously published work

Parts of this dissertation cover research reported in the following articles:

1. Kolkowitz, S., Safira, A., High, A.A., Devlin, R.C., Choi, S., Unterreithmeier, Q.P., Patterson, D., Zibrov, A.S., Manucharyan, V.E., Park, H., Lukin, M.D., Probing Johnson noise and ballistic transport in normal metals with a single-spin qubit. Science. 2015 Mar 6;347(6226):1129-32. doi: 10.1126/science.aaa4298. Epub 2015 Jan 29.

1

Introduction

As a technological tool, the Nitrogen Vacancy (NV) center has held promise for the past a decade or so, both as a sensor and for quantum information processing; this thesis includes work that continues to push the boundaries along these fronts. This introduction presents a brief introduction to the NV center, focusing on the elements of the NV center applicable to the work discussed in later chapters in this thesis, as well as a discussion for how it could find its way as a used in a more impactful and widespread fashion within society.

1.1 The Nitrogen-Vacancy Center

An NV center is a type of defect in an otherwise pristine, regular diamond (carbon) lattice. Specifically, it is a defect in which a carbon atom is substituted with a nitrogen atom, and a neighboring carbon atom is missing (vacant). In usual studies of solid state quantum mechanics, one would usually quickly focus on the electron energy levels due to a periodic potential, the result of which are hugely spread out wave electron wave functions and energy band diagrams. An NV center, however, precisely breaks that periodic potential, and as a result, allows for there to be a local electron wave function, similar to quantum dots [46]. Fittingly, an NV center is often considered a molecule within a lattice, and can be treated with many of the tools developed within AMO physics [17].

The spin substates of an NV center are viewed as a promising tool for quantum

information processing for the following reasons:

- Initialization. Upon illumination with green light, the NV center spin sublevels will equilibrate such that most of the population is in the $|0\rangle$ sublevel.
- Spin Readout. In the most basic scheme, the NV center can be easily read out by carefully measuring the number of red photons emanating from the NV center during green light illumination. Other schemes, including single-shot readout schemes, also exist [38], but only the simplest is used in this thesis.
- Long coherence times. A big limiting factor in the majority of quantum technology development is that of outside interactions limiting the timescales over which any coherent interactions can occur before random interactions cause you to lose track of the state of the system. For the NV center, the spin relaxation times could be made quite long (≈ 1 s, but suspected to be higher) [7].
- Single-qubit manipulation. As with any spin, magnetic fields can manipulate them; since NV centers are trapped within their host lattice, it can often be relatively easy to bring them near microwave circuit structures to perform single-qubit rotations.

A notable missing element is that of two-qubit interactions, which is the biggest motivator for three years of work done represented this thesis. Although a few schemes exist in the path towards engineerable two-qubit interactions, this thesis focuses on one that makes use of another quantum system that has seen great advances in recent years, mechanical resonators.

1.1.1 Mechanical Resonators

Great progress has been made in recent years in improving the purity of mechanical resonator systems across a very wide range of sizes [5]. From a device perspective,

several different incarnations of masses in harmonic potentials have been fabricated that have pushed the limits of the dissipation mechanisms to ultra-high values, such as that of silicon nitride string resonators ($Q > 10^6$ [51]), silicon mechanical crystals ($Q > 10^{10}$ [37]), and silicon nitride membranes ($Q > 10^8$ [60]). Such systems have become a playground for quantum effects and quantum technologies, starting from early experiments in mechanical oscillator cooling, in which the phonon state of a mechanical oscillator is brought at or near its ground state, to much more challenging photon-conversion experiments today, in which mechanical oscillators play a crucial role in coherently converting photons from one wavelength to another [15, 24, 56].

In this thesis, we utilize this great progress in quantum mechanical oscillator technology to push along a different path: building a hybrid mechanical oscillator-NV system whose natural Hamiltonian gives rise to entangling operation between NV centers. Specifically, with two NV's in close proximity to a mechanical oscillator equipped with a magnetic oscillating mass, the NV's are naturally coupled to the motion via the changing magnetic field at the position of the NV centers as the magnetic mass oscillates. When such a system is built with sufficiently high magnetic field gradients (to induce the largest impact on the NV per unit displacement of the oscillator), low mechanical decoherence (to isolate the system from the mechanical resonator's external bath), and NV center coherence times, the system becomes a strong candidate as a platform for quantum computing and engineering with NV centers. Compared to other schemes, the system is more scalable, as interactions can be engineered with the

proper placement of mechanical oscillators with respect to NV centers. Such a system, however, is difficult to engineer, as it requires state-of-the-art results from those aforementioned qualities. Chapter 3 covers this effort to create two-qubit interactions with mechanical resonators in NV centers in great detail.

1.1.2 Levitating Micromagnets

Speaking further along the lines of new platforms for quantum simulation and computation, Chapter 4 of this thesis covers the initial studies into one such platform more nascent than NV centers: levitating magnets over superconductors. As a mechanical system, levitated magnets over superconductors have been studied extensively for their applicability within mechanical engineering [14], but few have studied pushing the limits of these levitated magnets towards quantum effects. Chapter 4 includes details towards miniaturizing such a setup, and details the current state-of-the-art in such experiments.

1.2 The NV center for Magnetic Field Sensing

As a spin, the NV center is naturally susceptible to magnetic fields via the Zeeman effect, and a large effort has been made over the past decade in maturing it as a magnetic field sensor. In this section, we outline three of the most relevant magnetometry schemes for this thesis: electron-spin resonance, XY-8 pulse sequence magnetometry,

and Spin Relaxation noise magnetometry.

1.2.1 Electron Spin Resonance

Among the simplest schemes for NV magnetometry is electron spin resonance (ESR), often used for easy measurements of DC magnetic fields. In NV centers, ESR experiments utilize a combination of the initialization, spin readout, and microwave manipulation properties mentioned in the previous section: red fluorescence is monitored as the frequency of an external microwave field is varied. For a typical random externally-applied microwave frequency, the NV center spin is unaffected; as a result, the measured red fluorescence would correspond to the NV center steady state fluorescence from being in the $|0\rangle$ sublevel. On the other hand, when the externally-applied microwave field is on resonance with an NV center spin transition, the resulting average red photon fluorescence changes. In addition to the steady initialization occurring due to the optical excitation, the externally-applied microwave field stimulates transitions between spin sublevels. As the fluorescence is maximized when in the $|0\rangle$ sublevel, the resulting red photon fluorescence is observed to have decreased under such resonance conditions. Finally, the identified transition frequency is readily mapped to the magnetic field strength at the point of the NV center (by multiplication with the electron gyromagnetic ratio, of course).

1.2.2 AC Pulse-Sequence Magnetometry

Although more complicated, the schemes presented here have the added bonus that they can measure the magnetic field strength in a frequency-sensitive manner. These schemes are generally termed "pulse sequences" because they rely on careful manipulations of the spin states of the NV center, usually utilizing short microwave pulses.

1.2.2.1 Hahn Echo

The simplest of such pulse sequences is the so-called Hahn Echo sequence. The following sequence of steps is taken with an NV center subject to an external AC magnetic field:

1. Initialize the NV center in the $|0\rangle$ state.
2. Apply a $\pi/2$ pulse.
3. Wait for a time τ.
4. Apply a π pulse.
5. Wait for a time τ.
6. Apply a $\pi/2$ pulse.
7. Measure the state.

During steps 3 and 5 — the so-called "free-precession" times — the quantum state of the NV center is not in an eigenstate and oscillates with a frequency proportional to the difference in energy between its $|0\rangle$ and $|1\rangle$ states. Importantly, the intermediate π pulse causes the oscillation in the second free precession time to exactly cancel

the precession in the first free precession time. With no external AC magnetic fields at all, the above would result in being in the $|1\rangle$ state. Even with a DC magnetic field, that change in energy in the $|1\rangle$ state would result in a different oscillation frequency during steps 3 and 5, but since the π pulse causes the exact opposite dynamics to occur, the result of the above is in being in the $|1\rangle$ state.

With an external AC magnetic field, the magnetic field has a chance to impact the first free precession time differently from the second. In fact, when the magnetic field in the first free precession time is exactly opposite to that in the second, there will be a net accumulated phase during steps 3 through 5 in the above, and the result of the procedure will not be such that the NV is in the $|1\rangle$ state. As a result, magnetic fields with a period of 2τ have a large impact on the result of the above procedure, and others generally have a smaller impact.

1.2.2.2 XY-8 pulse sequences

XY-8 pulse sequences differ from Hahn Echo in that they generally result in sharper frequency filtering while being relatively robust to pulse errors. Fundamentally, the sequence adds π pulses to the above to add further constraints on the set of external magnetic field frequencies that would cause a net phase accumulation, while also boosting the signal from them due to the longer phase accumulation time from them.

Further discussion can be found in Chapter 3 of this thesis.

1.2.3 Spin Relaxation Noise Magnetometry

Another method more recently investigated is that of using the spin relaxation time of an NV center as a probe of nearby magnetic field noise. Specifically, because the NV center typically has a long spin relaxation time, sources of magnetic field noise can easily become the leading-order source of spin relaxation. Combined with an NV center's unparalleled localization, and thus spatial resolution, one can put NV centers in the vicinity of such sources, often, and gain information of the strength of magnetic field noise at very high resolution. Such work is discussed in Chapter 2 of this thesis.

1.3 Future Applications and Outlook

Physics research is rooted uncovering, exploring, and understanding new natural phenomena, the early work necessary for technological development of any kind. In regard to making an impactful technology for the masses, a large fraction of the work necessary is in making the work simply easier to do — that is, such that it would not require physics PhD's to reproduce. For NV center research, the most basic NV center experimental setup, including focused green laser illumination and red fluorescence readout, is becoming more and more standard and easy to construct. Chapter 5 of this thesis is an example of research presented in this thesis that helps in this vein: a software package that allows for easy control of experiments, which, along with other the open-source tools written in our labs, can save a lot of effort for any person inter-

ested in doing NV research. The current state of software within experimental physics labs is outdated, and has undoubtedly lead to a huge amount of redundant work done by separate labs within the community. At this point, the community is large enough to start consolidating such work, and in doing so, saving setup time within the lab and providing better information about the work done within the lab.

In regard to the other two NV center thrusts of this thesis, each should be considered separately for its potential as a technology. In the case of noise magnetometers, a few important applications should be noted. The main decoherence mechanisms in superconducting qubits are not very well understood or (of course) controlled for, although several hypotheses exist, such as that of two-level fluctuators within oxide materials in the superconducting qubit. NV centers can act as a unique probe for some of the underlying sources of magnetic field noise. Furthermore, NV centers can also play a role in characterization of nanoscale circuits and uncover fascinating structure in exotic condensed matter phenomena, where spin and current noise can be externally sensed with sensitive magnetometers.

For quantum information processing, NV centers have an uphill battle against several other quantum computing platforms, but as of the time of this writing, progress in quantum computing continues to be slow but steady. As a result, there is still ample room to look into and push for new platforms for quantum simulation and computation, as there has been for almost two decades, especially given the promise of the NV center.

In both of these cases, NV centers continue to be utilized as a research subject and tool, but with continued promise for applications that make an impact on society.

2

Johnson Noise Near Metal Films

2.1 Introduction

Traditionally, Johnson noise is the noise due to the thermal motion of electrons. Johnson noise could be a limiting factor in many precision electronics. In this section, we discuss theoretical and experimental work in using NV centers to probe magnetic field noise outside of a metal, and thus the random motion of electrons within the metal. We demonstrate differing behavior in the case of electrons with long mean free paths, and thus demonstrate the utility of NV center T_1 relaxometry in probing exotic phenomena in condensed matter systems. For the full in-depth derivation, see Appendix B.

2.2 Experimental Results

Understanding electron transport, dissipation, and fluctuations at sub-micron length scales is critical for the continued miniaturization of electronic [34, 58] and optical devices[19, 39, 59], as well as atom and ion traps[13, 22, 23, 26, 31], and for the electrical control of solid-state quantum circuits[29]. While it is well-known that electronic transport in small samples defies the conventional wisdom associated with macroscopic devices, resistance-free transport is difficult to observe directly. Most of the measurements demonstrating these effects make use of ohmic contacts attached to sub-micron scale samples and observe quantized but finite resistance corresponding to the voltage drop at the contact of such a system with a macroscopic conductor[9, 18].

Techniques for non-invasive probing of electron transport are now actively explored[11, 12] because they can provide insights into electronic dynamics at small length scales. Our approach makes use of the electromagnetic fluctuations associated with Johnson noise close to a conducting surface, which can be directly linked to the dielectric function at similar length scales, providing a non-invasive probe of electronic transport inside the metal. Measurements of these fluctuations at micron length scales utilizing cold, trapped atoms showed excellent agreement with predictions based on diffusive electron motion[22, 26, 31], while millimeter length scale measurements utilizing superconducting quantum interference devices (SQUIDs) have been demonstrated for use as an accurate, contact free thermometer[49].

Our approach makes use of the electronic spin associated with nitrogen-vacancy defect centers in diamond (NVs) to study the spectral, spatial, and temperature dependence of Johnson noise emanating from conductors. The magnetic Johnson noise results in a reduction of the spin lifetime of individual NV electronic spins, thereby allowing us to probe the intrinsic properties of the conductor non-invasively over a wide range of parameters. Individual, optically resolvable, NV centers are implanted $\sim$15 nm below the surface of a $\sim$30-μm thick diamond sample. A silver film is then deposited on or positioned on the diamond surface (Fig. 1A). The spin sublevels $|m_s = 0\rangle$ and $|m_s = \pm 1\rangle$ of the NV electronic ground state exhibit a zero-field splitting of $\Delta = 2\pi \times 2.88$ GHz[6, 16, 36, 55]. The relaxation rates between the $|0\rangle$ and $|\pm 1\rangle$ states provide a sensitive probe of the magnetic field noise at the transi-

tion frequencies $\omega_{\pm} = \Delta \pm 2g\mu_B B_{||}/\hbar$, where $B_{||}$ is the magnetic field along the NV axis[41, 50] (Fig. 1B).

The impact of Johnson noise emanating from a polycrystalline silver film deposited on the diamond surface (Fig. 1C) is evident when comparing the relaxation of a single NV spin below the silver (red circles) to the relaxation of the same NV prior to film deposition and after removal of the silver (open blue squares and triangles, respectively). At room temperature and in the absence of external noise, the spin lifetime is limited by phonon-induced relaxation to $T_1^{\text{ph}} \approx 4$ ms. With the silver nearby, the lifetime of the $|m_s = 0\rangle$ state is reduced to $T_1 = 165$ μs, which we attribute to magnetic Johnson noise emanating from the film. To verify that the enhanced relaxation is due to magnetic noise, we compare the lifetime of the $|0\rangle$ state, which has magnetic dipole allowed transitions to both of the $|\pm 1\rangle$ states, to that of the $|-1\rangle$ state, which can only decay directly to the $|0\rangle$ state (Fig. 1D). As expected for relaxation induced by magnetic noise, the $|-1\rangle$ state has approximately twice the lifetime of the $|0\rangle$ state. This is in contrast to the observed lifetimes when limited by phonon-induced relaxation (Inset, Fig. 1D), where the $|0\rangle$ and $|\pm 1\rangle$ states have almost identical lifetimes[54]. In what follows we define T_1 as the lifetime of the $|m_s = 0\rangle$ state.

To test the scaling of Johnson noise with distance (d) to the metal, we deposit a layer of SiO_2 on the diamond surface with a gradually increasing thickness (Fig. 2A). We characterize the thickness of the SiO_2 layer as a function of position on the sample (Inset, Fig. 2B), and deposit a 60-nm polycrystalline silver film on top of the SiO_2.

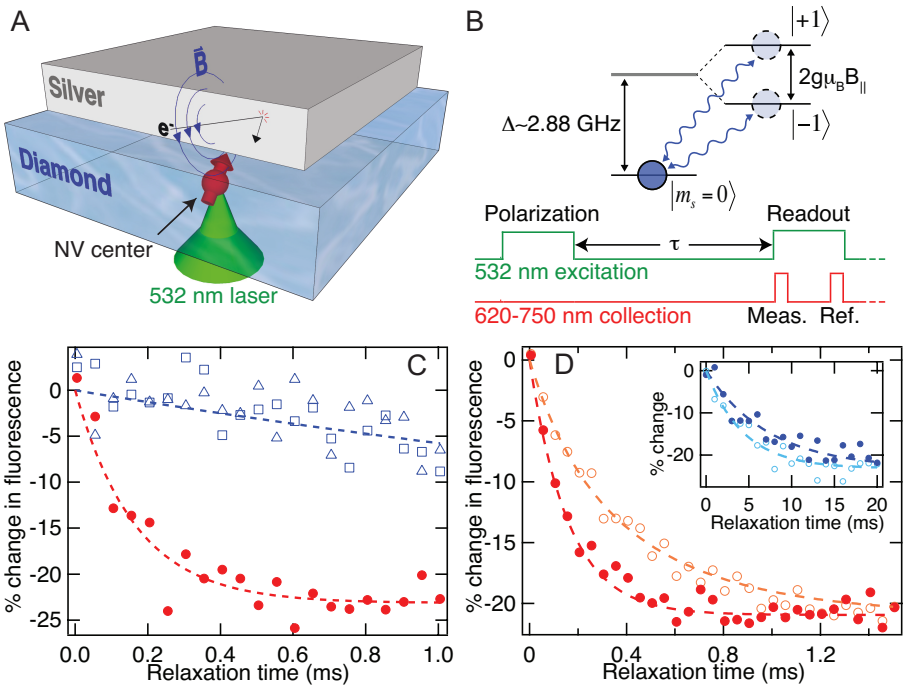

Figure 2.1: **Probing Johnson noise with single spin qubits. (A)** The thermally induced motion of electrons in silver generates fluctuating magnetic fields ($\vec{\mathbf{B}}$), which are detected using the spin of a single NV. The NV is polarized and read out through the back side of the diamond. **(B)** The NV spin is polarized into the $|m_s = 0\rangle$ state using a green laser pulse. Spin relaxation into the $|m_s = \pm 1\rangle$ states is induced by magnetic field noise at ~2.88 GHz. After wait time τ the population left in $|0\rangle$ is read out by spin-dependent fluorescence. All measurements shown were performed at low magnetic fields ($\Delta \gg g\mu_B B_{||}/\hbar$). **(C)** Spin relaxation data for the same single shallow implant NV before silver deposition (open blue squares), with silver deposited (red circles), and after the silver has been removed (open blue triangles). **(D)** Spin relaxation for a single NV close to a silver film prepared in the $|m_s = 0\rangle$ state (red circles), and in the $|m_s = -1\rangle$ state (open orange circles). **(Inset)** Spin relaxation for a single native NV in bulk diamond in the $|m_s = 0\rangle$ state (blue circles), and in the $|m_s = -1\rangle$ state (open light blue circles).

The conductivity of the silver film is measured to be 2.9×10^7 S/m at room temperature. By measuring the relaxation rates $\Gamma = 1/T_1$ of individual NVs at different positions along the SiO_2 ramp we extract the distance dependence of the noise (Fig. 2B), with the uncertainty in the distance dominated by the variation in the implanted depth of the NVs (taken to be 15±10 nm). To ensure that the measured rates are Johnson-noise limited, we measure the spin relaxation of 5-10 randomly selected NVs per location along the ramp, and plot the minimum observed rate at each location. As expected[22, 26, 31], the magnitude of the noise increases as the NVs approach the silver surface.

To investigate the dependence of the noise on temperature and conductivity, we deposit a 100-nm polycrystalline silver film on a diamond sample and measure the T_1 of a single NV beneath the silver over a range of temperatures (∼10-295 K). The measured relaxation rate for a single NV near the silver increases with temperature (red circles in Fig. 3A), as expected for thermal noise, but the scaling is clearly non-linear. This can be understood by recognizing that the conductivity of the silver film is also a function of temperature, and that the magnitude of the thermal currents in the silver depend on the conductivity. To account for this effect, a four point resistance measurement of the silver film is performed to determine the temperature dependence of the bulk conductivity of the silver film (Fig. 3B).

To analyze the dependance of the NV spin relaxation rate on distance, temperature, and conductivity, the model of ref.[23] is used, in which an electronic spin-1/2 qubit

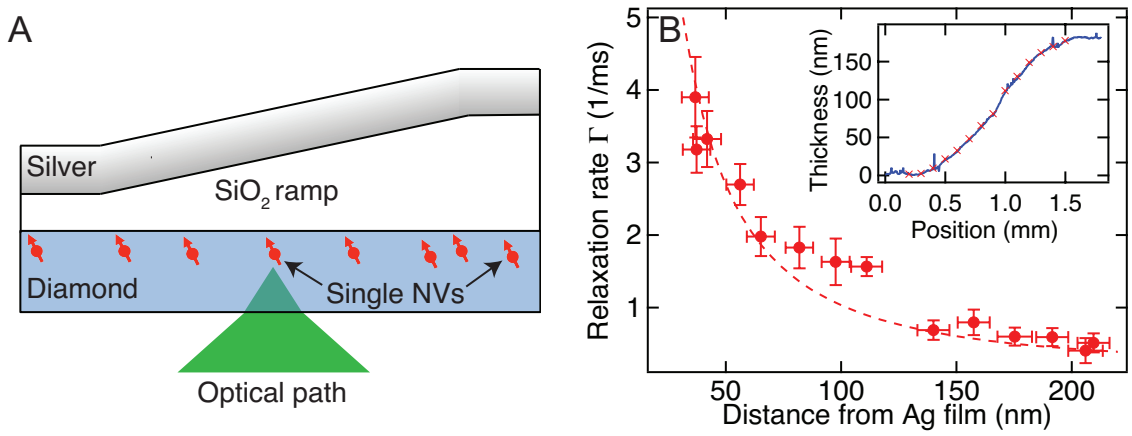

Figure 2.2: **Distance dependence of NV relaxation close to silver. (A)** A gradual SiO_2 ramp (slope of $\sim$.2 nm/micron) is grown on the diamond surface, followed by a 60 nm silver (Ag) film. **(B)** The NV relaxation rate is measured as a function of position along the ramp, which is then converted to distance to the film. At each point 5-10 NV centers are measured, and the minimum rate measured is plotted (red circles). The red dashed line shows the expected relaxation rate with no free parameters after accounting for the finite silver film thickness. **(Inset)** Thickness of the ramp as a function of lateral position along the diamond sample (blue curve). The red crosses correspond to the positions along the sample where the measurements were taken.

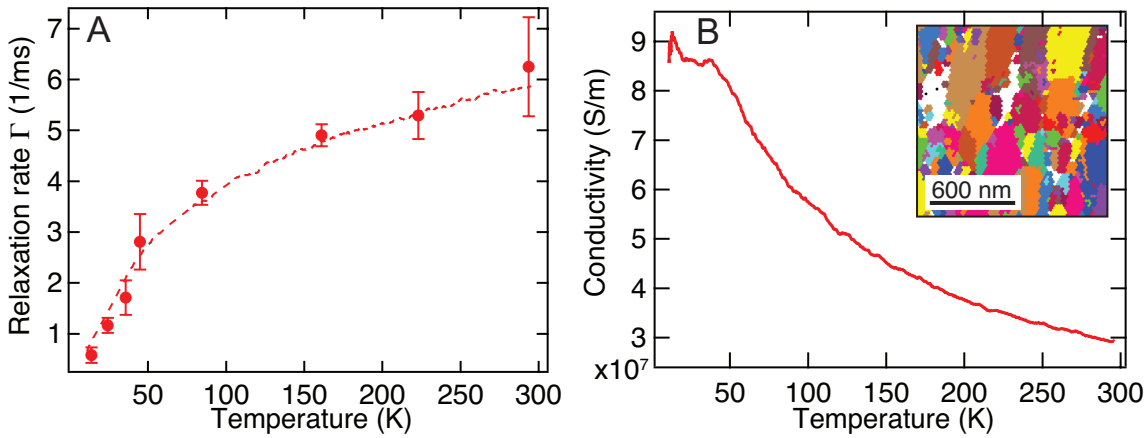

Figure 2.3: **Temperature dependence of NV relaxation close to polycrystalline silver. (A)** The measured relaxation rate T_1 of a single NV spin under a polycrystalline silver film as a function of temperature (red data points). The conductivity of the silver film as a function of temperature shown in **B** is included in a fit to Eq. 2, with the distance to the film as the single free parameter (red dashed line). The extracted distance is 31±1 nm. **(B)** The conductivity of the 100 nm thick polycrystalline silver film deposited on the diamond surface is measured as a function of temperature. **(Inset)** Grain boundaries within the polycrystalline silver film, imaged using electron backscatter diffraction (EBSD). The average grain diameter is 140 nm, with a standard deviation of 80 nm.

with Larmor frequency ω_L is positioned at a distance d from the surface of a metal. For silver at room temperature the skin depth at ω_L is $\delta \approx 1$ μm; consequently when $d <$100 nm we are in the "quasi-static" limit $d \ll \delta$. The thermal limit $k_B T \gg \hbar\omega_L$ is valid for all temperatures in this work. In this regime the magnetic noise spectral density perpendicular to the silver surface is given by

$$S_B^z = \frac{\mu_o^2}{16\pi} \frac{k_B T \sigma}{d}, \tag{2.2.1}$$

where σ is the temperature-dependent conductivity of the metal as defined by the Drude model. This scaling can be intuitively understood by considering the magnetic field generated by a single thermal electron in the metal at the NV position, $B_o = \frac{\mu_o e v_{th}}{4\pi d^2}$, where the thermal velocity $v_{th} \propto \sqrt{k_B T/m_e}$, m_e is the effective mass of electrons in silver and e is the electron charge. In the limit $d \ll \delta$ screening can be safely ignored, and the NV experiences the magnetic field spectrum arising from N independent electrons in a volume V, $S_B \propto V n \langle B_o \rangle^2 \tau_c$, where n is the electron density and τ_c is the correlation time of the noise, given by the average time between electron scattering events, $\tau_c = l/v_F$, where l is the electron mean free path and v_F is the Fermi velocity. Recognizing that the NV is sensitive to the motion of electrons within a sensing volume $V \propto d^3$, we arrive at the scaling given by Eq. 2.2.1, with $\sigma = \frac{n e^2 \tau_c}{m_e}$. Applying Fermi's golden rule and accounting for the orientation and spin-1 of the NV yields the relaxation rate for the $|m_s = 0\rangle$ state

$$\Gamma = \frac{1}{T_1} = \frac{3 g^2 \mu_B^2}{2\hbar^2} S_B^z \left(1 + \frac{1}{2}\sin^2(\theta)\right), \tag{2.2.2}$$

where $g \approx 2$ is the electron g-factor, μ_B is the Bohr magneton, and $\theta \approx 54.7°$ is the angle of the NV dipole relative to the surface normal vector. In Fig. 2B the inverse scaling with distance d predicted by Eq. 2.2.1 is clearly evident for NVs very close to the silver. At distances comparable to the silver film thickness Eq. 2.2.1 is no longer valid, but we recover excellent agreement with the no-free-parameters prediction of Eq. 2.2.2 by including a correction for the thickness of the silver film (red dashed line in Fig. 2B), which is measured independently. The measured relaxation rates as a function of temperature are also in excellent agreement with the predictions of Eq. 2.2.2 (red dashed line in Fig. 3A), while the extracted distance of 31±1 nm is consistent with the expected depth.

Remarkably, very different results are obtained when we replace the polycrystalline film with single-crystal silver. For this experiment, a 1.5-μm thick single-crystal silver film grown by sputtering onto silicon [8, 40] is placed in contact with the diamond surface. The measured conductivity of the single-crystal silver exhibits a much stronger temperature dependance (blue line in Fig. 4A) as compared to that of the 100-nm thick polycrystalline film. Fig. 4B presents the measured relaxation rate as a function of temperature for an NV in a region in direct contact with the single-crystal silver (blue squares). The dashed blue line corresponds to the temperature dependent rate predicted by Eq. 2.2.2, which strongly disagrees with the experimental results. Specifically, because the measured silver conductivity increases faster than the temperature decreases in the range from room temperature down to 40 K, Eq. 2.2.2 predicts the

relaxation rate should increase as the temperature drops, peaking at 40 K and then dropping linearly with temperature once the conductivity saturates. Instead, the T_1 of the NV consistently increases as the temperature drops, implying that at lower temperatures the silver produces considerably less noise than expected from Eq. 2.2.2. We observe similar deviation from the prediction of Eq. 2.2.2 for all 23 NVs measured in the vicinity of the single-crystal silver.

To analyze these observations, we note that the conventional theoretical approach[23] resulting in Eq. 2.2.2 treats the motion of the electrons in the metal as entirely diffusive, using Ohm's law, $\mathbf{J}(\mathbf{r}, t) = \sigma \mathbf{E}(\mathbf{r}, t)$, to associate the bulk conductivity of the metal with the magnitude of the thermal currents. While accurately describing the observed relaxation rates next to the polycrystalline material, where the resistivity of the film is dominated by electron scattering off of grain boundaries (Inset, Fig. 3B), this assumption is invalid in the single-crystal silver film experiments, particularly at low temperatures. Here, the measured conductivity of the single-crystal film indicate that the mean free path l is greater than one micron, significantly exceeding the sensing region determined by the NV-metal separation, and thus the ballistic motion of the electrons must be accounted for. Qualitatively, the correlation time of the magnetic noise in this regime is determined by the ballistic time of flight of electrons through the relevant interaction region $\tau_c \sim d/v_F$ (Fig. 4C). This results in a saturation of the noise spectral density and the spin relaxation rate Γ as either the NV approaches the silver surface or as the mean free path becomes longer at lower tem-

peratures, with the ultimate limit to the noise spectrum given by:

$$S_B^z \sim \frac{2\mu_o^2 k_B T}{\pi} \frac{ne^2}{m_e v_F}. \tag{2.2.3}$$

This regime of magnetic Johnson noise was recently analyzed theoretically[29] using the Lindhard form non-local dielectric function for the metal modified for finite electron scattering times[4, 21]. Comparison of this model (solid line in Fig. 4B) to the data, with distance again as the only free parameter, yields excellent agreement for all 23 measured NVs. Fig. 4D shows the measured T_1 times at 103 K and 27 K for each NV as a function of extracted distance (blue triangles). Of the 23 NVs measured, 15 are in a region of the diamond sample in direct contact with the silver. Excellent agreement between the non-local model (solid lines) and the data is observed for all 23 NVs at all 12 measured temperatures. Apparent in Fig. 4D is the saturation of the relaxation rate as the NV approaches the silver surface, and as the mean free path becomes longer at lower temperatures (dashed black line), as predicted by Eq. 3.

While ballistic electron motion in nanoscale structures has previously been studied and utilized[9, 18], our approach allows for non-invasive probing of this and related phenomena, and provides the possibility for studying mesoscopic physics in macroscopic samples. The combination of sensitivity and spatial resolution demonstrated here enables direct probing of current fluctuations in the proximity of individual impurities, with potential applications such as imaging of Kondo states and probing of novel two-dimensional materials[35], where our technique may allow for

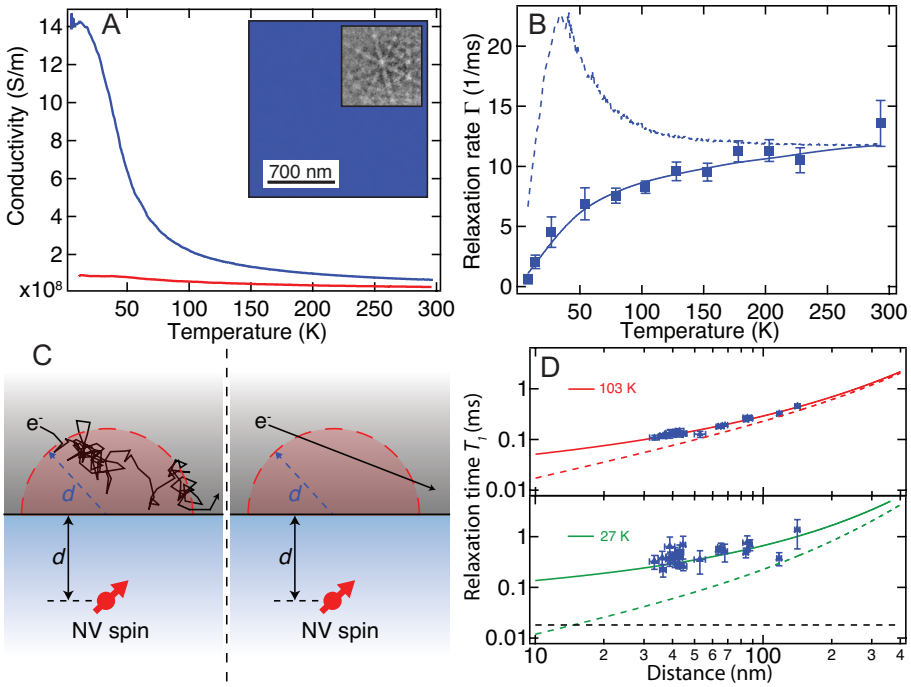

Figure 2.4: **Temperature dependence of NV relaxation close to single-crystal silver. (A)** Measured conductivity of single-crystal (blue curve) and polycrystalline (red curve, same as Fig. 3B) silver as a function of temperature. **(Inset)** Electron backscatter diffraction image of the single-crystal silver film showing no grain boundaries, and the observed diffraction pattern. **(B)** Relaxation of a single NV spin under single-crystal silver as a function of temperature (blue squares). Eq. 2 is fit to the data from 200-295 K (blue dashed line). A non-local model is fit to the data (blue solid line), the extracted distance between the NV and the silver surface is 36±1 nm. **(C)** Cartoon illustrating the relevant limits, where the noise is dominated by diffusive electron motion (left, $l \ll d$), and ballistic motion (right, $l \gg d$). **(D)** The same data as **B** was taken for 23 NVs at varying distances from the film. The T_1 of each NV at 103 K (top) and 27 K (bottom) is plotted against the extracted depth (blue triangles). The non-local model (solid colored lines) saturates at a finite lifetime determined by Eq. 3 (bottom, dashed black line), while the local model does not (dashed colored lines).

the spatially resolved probing of edge states[9]. Likewise, it could enable investigation of the origin of $1/f$ flux noise by probing magnetic fluctuations near superconducting Josephson circuits[3, 20]. Finally, as Johnson noise presents an important limitation to the control of classical and quantum mechanical devices at small length scales[13, 22, 23, 26, 31], the present results demonstrate that this limitation can be circumvented by operating below the length scale determined by the electron mean free path.

2.3 SOM

2.3.1 Experimental materials and methods

The experiments were performed using 30 micron thick electronic grade diamonds grown, thinned, and polished by Element Six with a natural isotopic abundance of carbon. Shallow NV centers were generated through Nitrogen-14 implantation at 6 keV energy at a density of $2\times10^9/\text{cm}^2$, followed by annealing at 800 °C. The single-crystal silver films were grown by sputtering at 300 °C onto a (111) oriented single-crystal silicon substrate [8, 40], with a deposition rate of ∼1.5 nm/s, as discussed in detail in section 2.3.2.1. The polycrystalline silver films were evaporated directly onto the diamond. A 5-nm layer of silica (SiO_2) was grown on the diamond surface prior to the metal deposition to preserve NV properties. Temperature dependence measure-

ments were performed in a Montana Instruments closed cycle cryostat.

2.3.1.1 Averaging, number of points, and wait times for relaxation measurements

All T_1 measurements in this work are composed of the average of many repeated sequences as described in Figure 1B of the main text. Number of averages, number of points, and the range of evenly spaced wait times for each figure are given in Table 2.1. All error bars shown in this work correspond to one standard deviation.

Figure(s)	Number of Averages	Number of points	Wait time range
1C	2×10^5	21	0 - 1 ms
1D, S4	2×10^5	31	0 - 1.5 ms
2B, S5	1×10^5	21	0 - 2 ms
3A	2×10^5	11	0 - 2 ms
4B, 4D, S6	2×10^5	21	0 - 1.5 ms for $\leq$ 103 K 0 - 0.6 ms for $>$ 103 K

Table 2.1: Number of averages, number of measured points, and range of evenly spaced wait times for the T_1 measurements presented in each figure.

2.3.2 Fabrication and metrology

2.3.2.1 Single-crystal silver deposition and characterization

The single-crystalline silver films were grown using direct current plasma sputtering (AJA International Orion 3)[8, 40]. The sputtering targets used were 99.99% pure silver (Kurt Lesker, Inc). Films were deposited onto prime-grade, degenerately doped

(111)-Si wafers (0.0015-0.005 Ω-cm). The substrates were ultrasonically cleaned in acetone, followed by a 2:1 sulfuric acid:hydrogen peroxide solution to eliminate organics. The substrates were then immersed in 49% hydrofluoric acid for 10–15 seconds to remove any native oxide. Next, the substrates were rapidly transferred into the sputtering chamber and the chamber was pumped down to minimize re-oxidation of the surface. Upon reaching a base pressure of about 5×10^{-7} Torr, the substrate was heated to 300 °C and silver was deposited at a rate of 1.5-1.7 nm/s.

Following the growth, multiple characterization techniques were used to test the quality of the deposited films. The crystallinity and surface quality of the films were probed via transmission electron microscopy (TEM) and atomic force microscopy (see Figure 2.5). The TEM scans confirm that the silver films are single-crystal, with lattice fringes apparent from the bulk to the surface. The AFM scans confirm that the films are ultra-smooth with typical root-mean-square roughness of ∼1 nm. Consistent with the TEM scans and electron backscatter diffraction imaging (see below), no grain boundaries were observed within the 10 μm × 10 μm scan region.

2.3.2.2 Characterization of silver film grain size

Crystal orientation and average grain size of the silver samples were measured with electron backscatter diffraction (EBSD). For the polycrystalline films, we use as reference a 100 nm film deposited on 5 nm of SiO_2 on (100) silicon. In the insets of Figures 3 and 4 of the main text, inverse pole figures of the electron backscatter diffrac-

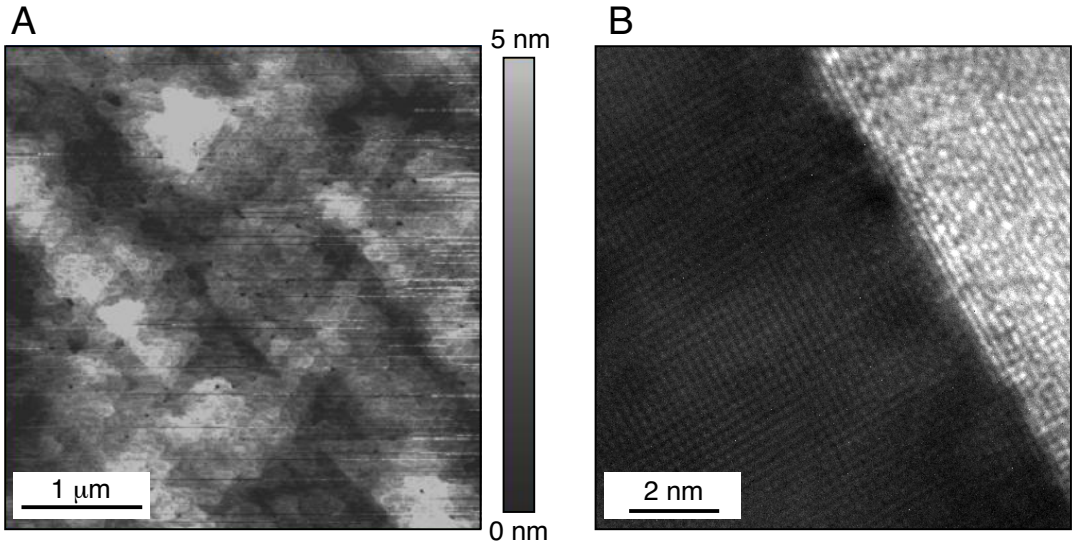

Figure 2.5: Single-crystal AFM and TEM characterization. **(A)** AFM image of a typical single-crystal silver surface grown for this work. The scan indicates a ∼1 nm RMS roughness over a 4 μm × 4 μm range, thus allowing for good diamond-silver contact. **(B)** A TEM image of a typical silver sample, where the growth direction is from left to right and the silver is capped with a titanium capping layer resulting in the brighter region on the right of the image. The image reveals single-crystallinity of the silver up to the surface.

tion data were post-processed to highlight grain boundaries. The areas in white are areas of large noise where the the crystal orientation could not be discerned with high confidence, while the other colors indicate different crystal orientations. The inverse pole figures from which those images are derived are given in Figure 2.6. EBSD data of the polycrystalline silver film indicated a very granular film, with an average grain diameter of 140 nm and a standard deviation of 80 nm. Grain diameter was approximated by taking the diameter of the circle with the same area as each grain. For the single-crystal films, EBSD data indicated the sample is a single-crystal from nanome-

ter to millimeter length scales, and confirmed a (111) exposed crystal surface for the single-crystal silver, as expected from the growth conditions.

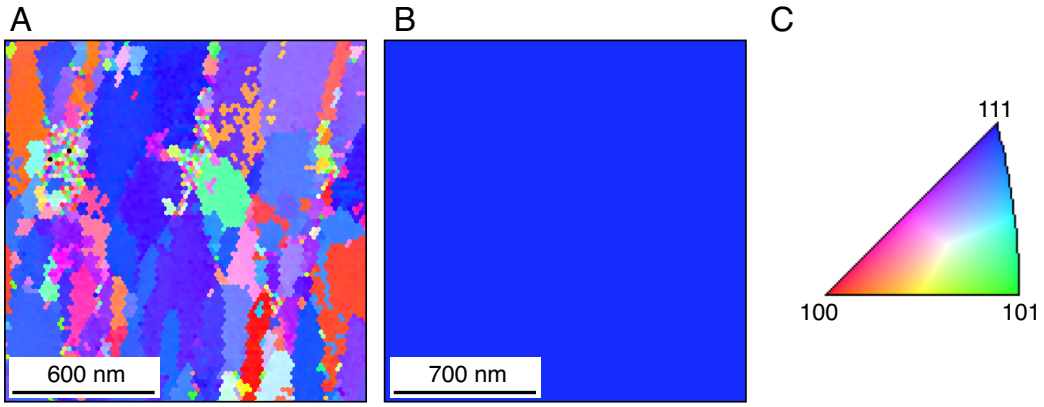

Figure 2.6: **Single-crystal and polycrystalline silver Inverse Pole Figures (IPF).** Using electron backscatter diffraction imaging in an SEM, we image the local crystal orientations of our silver films, and measure the average grain size. **(A)** Data for a 2 μm $\times$ 2 μm area of evaporated silver on 5 nm of SiO_2 on (100) silicon. The crystal variations along the direction perpendicular to the sample can cause mixed diffraction signals, and the crystal orientation fits in those regions have low confidence and result in an IPF with unphysical pixel-to-pixel variations in the crystal orientation (left region of image). **(B)** EBSD data for the same size region for single-crystal silver. No grain boundaries are visible. **(C)** Color scale conversion legend to map color to silver crystal orientation.

2.3.2.3 Diamond surface characterization

AFM and profilometer scans were performed on the implantantation-side surface of the diamond used for the single-crystal silver measurements, as shown in Figure 2.7. The diamond was found to have a local surface roughness of $\sim$ 1 nm RMS over a 10 μm $\times$ 10 μm range, and to have variations of $\sim$ 10-20 nm peak to peak at the $\sim$100

micron length scale across the entire sample. The NVs sampled from the spatial region over which the diamond was considered to be in contact with the silver were all within a single 40 μm $\times$ 40 μm field of view (see subsection 2.3.5.2 for details.)

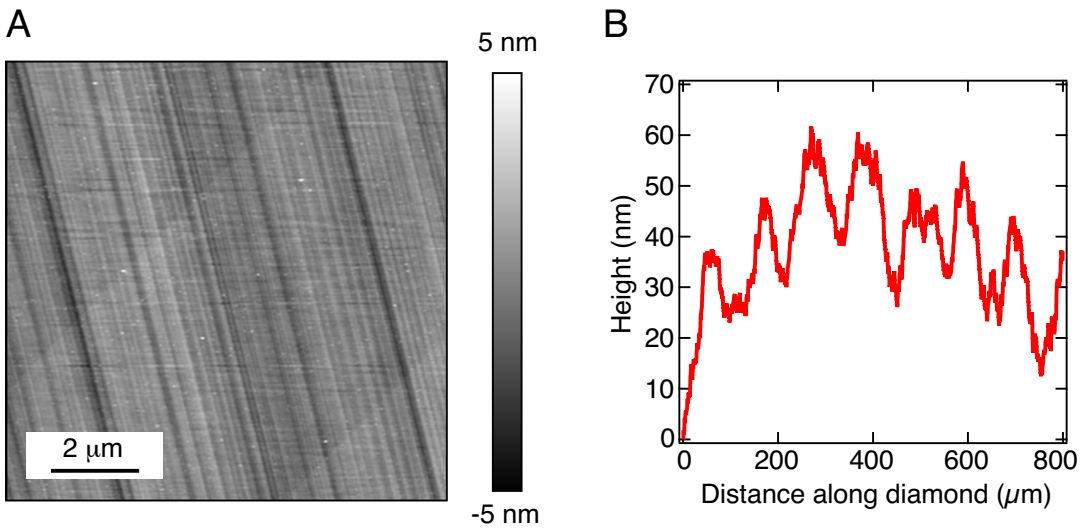

Figure 2.7: AFM and profilometer characterization of diamond surface. **(A)** An AFM image of the surface of the diamond used for the single-crystal silver measurements. The scan indicates a $\sim$1 nm RMS roughness over a 10 μm $\times$ 10 μm range, thus allowing for good diamond-silver contact. **(B)** A profilometer scan of the surface of the diamond sample.

2.3.2.4 Fabrication of devices for temperature-dependent studies

For the temperature dependence measurements under evaporated polycrystalline silver (Fig. 3 in the main text), a 5 nm layer of silica was deposited onto the diamond via CVD growth, and a 100 nm layer of silver was then deposited onto the silica film.

In the case of the measurements under single-crystal silver, direct-deposition tech-

niques to create single-crystal silver directly on diamond devices do not presently exist. Instead, the device used in this experiment was fabricated using optical contact bonding between the diamond and the single-crystal silver surfaces. The diamond sample was prepared for bonding by cleaning in a boiling 1:1:1 solution of nitric, sulfuric, and perchloric acids for at least one hour, directly prior to bonding. After growth, the single-crystal silver films were stored with a 50 nm capping layer of alumina to prevent surface oxidation. Directly prior to the bonding process, the alumina capping layer was stripped away in hydrofluoric acid. The diamond was then placed NV side down in contact with the freshly exposed silver surface. A drop of de-ionized water was placed on top of the diamond and allowed to wick in-between the diamond and the silver, and the the diamond was lightly pressed against the silver from above, while the two samples were blow-dried with a nitrogen spray gun, leaving the diamond bonded directly to the silver surface. This procedure was performed in a cleanroom, with careful attention to the cleanliness of the tweezers and sample holders. Several attempts were required to produce the final device used in this experiment, which demonstrated very robust bonding between the diamond and the silver, and survived multiple thermal cycles from 300-10 K.

2.3.3 Johnson Noise Theory

2.3.3.1 Spin decay rate near a conducting metallic half-space

We derive expressions for the lifetime of a spin interacting with magnetic Johnson noise above a metallic half space following the prescriptions of [23] and [29].

From Fermi's golden rule and the fluctuation-dissipation theorem, the decay rate from $|m_s = 0\rangle$ to $|m_s = 1\rangle$ for a spin-1 system at a distance z above the surface of a metal at temperature T, with level separation ω and magnetic dipole moment in the ith direction is then given by

$$\Gamma_{0\to1} = \frac{\mu^2}{\hbar^2} \coth\left(\frac{\hbar\omega}{2k_BT}\right) S_B^{ii}(z,\omega) \tag{2.3.1}$$

where

$$S_B^x(z,\omega) = S_B^y(z,\omega) = \frac{\hbar}{8\pi\epsilon_0 c^3}\mathrm{Re}\int_0^\infty dp \frac{p\left(\omega^2 r^p(p) + (p^2c^2-\omega^2)r^s(p)\right)}{\sqrt{\omega^2-p^2c^2}} e^{2iz\sqrt{\omega^2/c^2-p^2}} \tag{2.3.2}$$

$$S_B^z(z,\omega) = \frac{\hbar}{4\pi\epsilon_0 c^2}\mathrm{Re}\int_0^\infty dp \frac{p^3}{\sqrt{\omega^2/c^2-p^2}} e^{2iz\sqrt{\omega^2/c^2-p^2}} r^s(p), \tag{2.3.3}$$

and r^p and r^s denote the Fresnel Coefficients for plane waves incident on the material interface for p and s polarized light, respectively. We choose a coordinate system in which the z axis is perpendicular to the material interface; as $S_B^{\alpha\beta}$ is a diagonal tensor in this coordinate system, we drop one index and denote the diagonal elements by identifying $S_B^{ii} = S_B^i$. We have also assumed off-diagonal density matrix elements to

be 0, $\rho_{ij} = \langle i|\rho|j\rangle = \sum \delta_{ij}$, consistent with T_2^* of the NVs in our experiment being much faster than the population dynamics of system.

2.3.3.2 Reflection coefficients

Explicitly, the reflection coefficients for a single material boundary are given by

$$r^s(p) = \frac{k_1 - k_2}{k_1 + k_2} \tag{2.3.4}$$

$$r^p(p) = \frac{\epsilon_2 k_1 - \epsilon_1 k_2}{\epsilon_2 k_1 + \epsilon_1 k_2} \tag{2.3.5}$$

with

$$k_1 = \sqrt{\epsilon_1 \omega^2/c^2 - p^2} \tag{2.3.6}$$

$$k_2 = \sqrt{\epsilon_2 \omega^2/c^2 - p^2} \tag{2.3.7}$$

where we have assumed $\mu_i \approx 1$ in all space, consistent with the materials used in this study. In the case of a spin above a metal, the above coefficients are valid when the thickness of the metal greatly exceeds the skin depth or when the spin-metal distance is much less than the thickness. To take into account the finite thickness of the film, the reflection coefficients take the form

$$r^s(p) = \frac{k_1^2 - k_2^2}{k_1^2 + k_2^2 + 2ik_1k_2\cot(k_2a)} \tag{2.3.8}$$

$$r^p(p) = \frac{\epsilon_2 k_1 - \epsilon_1 k_2}{\epsilon_2 k_1 + \epsilon_1 k_2 + 2i\epsilon_2 k_1 k_2 \cot(k_2 a)}, \tag{2.3.9}$$

where a is the thickness of the film [30].

In our experiments with polycrystalline silver, finite thickness effects have a sig-

nificant impact on the noise power spectrum outside of the film. The distance and temperature dependence experiments, depicted in Figures 2 and 3 in the main text, used films with thicknesses $a = 60$ nm and $a = 100$ nm, respectively. The theoretical predictions shown in those figures incorporate these finite-thickness corrections. Conversely, in the case of the single-crystal films, which are much thicker ($a = 1.5$ μm), we find that the corrections due to finite thickness are negligible.

Furthermore, in the experiments involving polycrystalline silver, an extra 5 nm layer of SiO_2 lies between the diamond and the metal. Such a geometry can also be accounted for with the appropriate reflection coefficients. However, because $\mu \approx 1$ in diamond and SiO_2, the length scales z and electromagnetic field wave vectors $|\mathbf{k}| = \epsilon\omega/c$ such that $|\mathbf{k}|z \gg 1$, and the electromagnetic response is dominated by $|\epsilon_2| = |\epsilon_{\mathrm{Ag}}| \gg \{|\epsilon_{\mathrm{Diamond}}|, |\epsilon_{\mathrm{SiO2}}|\}$, the effects of the diamond medium and the silica layer are both negligible.

2.3.3.3 Quasi-static approximation

It is convenient to perform approximations to the integrals in equations (2.3.2) and (2.3.3) to gain insight into the decay rate behavior in different regimes. In particular, in the case of a full metallic half space, and in the regime where the electromagnetic wavelength is much larger than the skin depth of the metal, $\lambda \gg \delta$, and the skin

depth is much larger than the spin's distance to the metal, $\delta \gg z$,

$$S_B^x(z) = S_B^y(z) \approx \frac{\hbar\omega\sigma}{64\pi\epsilon_0^2 z} \tag{2.3.10}$$

$$S_B^z(z) \approx 2S_B^x \tag{2.3.11}$$

In this regime, known as the quasi-static regime, the decay rate, as described in equation (2.3.1), is proportional to $1/z$, and thus $T_1 = 1/\Gamma \propto z$.

2.3.3.4 NV magnetic dipole orientation

We also must account for the orientation of the magnetic dipole of our NV centers when calculating the expected decay rate. The decay rate from $|m_s = 0\rangle$ to $|m_s = 1\rangle$ for a spin-1 system with a quantization axis making an angle θ with $\hat{\mathbf{z}}$, the vector normal to the metal surface, in the quasi-static limit is given by

$$\gamma_{0\to1} = \frac{1}{\hbar^2}\coth\left(\frac{\hbar\omega}{2k_BT}\right)\sum g^2\mu_B^2|\langle 1|S_i|0\rangle|^2 S_B^i(z,\omega) \tag{2.3.12}$$

$$\approx \frac{g^2\mu_B^2}{\hbar^2}\frac{2k_BT}{\hbar\omega}\left(\frac{1}{2}\cos^2(\theta)S_B^x(z,\omega) + \frac{1}{2}S_B^y(z,\omega) + \frac{1}{2}\sin^2(\theta)S_B^z(z,\omega)\right) \tag{2.3.13}$$

$$\approx \frac{g^2\mu_B^2\mu_0^2 k_BT\sigma}{32\pi z\hbar^2}\left(1 + \frac{1}{2}\sin^2(\theta)\right). \tag{2.3.14}$$

where in our temperature and frequency range of interest ($T > 4$ K and $\omega < 20$ GHz), $\coth(\hbar\omega/2k_BT) \approx 2k_BT/\hbar\omega$, and we choose our coordinate system such that the spin is always in the $x - z$ plane. All diamond samples used in the experiment are cut such that all four possible NV dipole orientations make the same angle $\theta = \frac{1}{2}(180^\circ - \cos^{-1}(1/3)) \approx 54.7^\circ$ with $\hat{\mathbf{z}}$.

2.3.3.5 Three-level system dynamics

We also must account for the population dynamics of our three level spin-1 coupled to a magnetic noise bath. The rate equations for this system are given by

$$\partial_t \begin{pmatrix} \rho_{00} \\ \rho_{-1-1} \\ \rho_{11} \end{pmatrix} = \begin{pmatrix} -2\gamma & \gamma & \gamma \\ \gamma & -\gamma & 0 \\ \gamma & 0 & -\gamma \end{pmatrix} \begin{pmatrix} \rho_{00} \\ \rho_{-1-1} \\ \rho_{11} \end{pmatrix}, \tag{2.3.15}$$

which, for boundary conditions $\rho_{00}(t=0) = 1$, give the solution

$$\rho_{00}(t) = \frac{2}{3}\exp(-3\gamma t) + \frac{1}{3}. \tag{2.3.16}$$

Thus, the population decay from the $m_s = 0$ state is a factor 3 larger than the rate given by equation (2.3.14), and we arrive at

$$\Gamma \approx \frac{3\mu^2 g^2 \mu_B^2 k_B T \sigma}{32\pi\hbar^2 z}\left(1 + \frac{1}{2}\sin^2\theta\right), \tag{2.3.17}$$

which is equivalent to equation (2) given in the main text.

2.3.3.6 Non-local corrections to the decay rate

To take into account the ballistic nature of the electron motion in the silver, we follow [29] and introduce a non-local permittivity. In this regime we find $S_B^z \approx 2S_B^x$ still holds, so for simplicity in the discussion that follows we consider only S_B^z. With the Lindhard form modified for finite electron lifetime, the s polarized reflection coefficient becomes

$$r^s(k_x,k_y) \quad = \quad \frac{\frac{2iqc^2}{\pi\omega^2}\int_0^\infty \frac{d\kappa}{\epsilon_t(k,\omega)-c^2k^2/\omega^2}-1}{\frac{2iqc^2}{\pi\omega^2}\int_0^\infty \frac{d\kappa}{\epsilon_t(k,\omega)-c^2k^2/\omega^2}+1}, \tag{2.3.18}$$

with $k^2 = p^2 + \kappa^2$ and the transverse permittivity defined as

$$\epsilon_t(k,\omega) \quad = \quad 1 - \frac{\omega_p^2}{\omega(\omega+i\nu)} f_t((\omega+i\nu)/kv_f), \tag{2.3.19}$$

and the function f_t defined as

$$f_t(x) = \frac{3}{2}x^2 - \frac{3}{4}x(x^2-1)\ln\left(\frac{x+1}{x-1}\right), \tag{2.3.20}$$

and ω_p is the electron plasma frequency, ν is the electron scattering rate, ω is the frequency of radiation, and v_f is the Fermi velocity. In the above expressions, the nonlocality manifests itself through the k dependence of the permittivity. In order to derive an analytical expression for S_B^z in the limit $z \to 0$, we first rewrite the S_B^z in terms of the rescaled, dimensionless momentum $\tilde{p} = (v_f/\nu)p$ and introduce $\alpha = \frac{\nu}{\omega}\frac{c}{v_f}$:

$$S_B^z = \frac{\hbar}{4\pi\epsilon_0 c^2}\frac{\nu^3}{v_f^3}\mathrm{Re}\int_0^\infty d\tilde{p}\frac{\tilde{p}^3}{\sqrt{1/\alpha^2-\tilde{p}^2}} e^{i\frac{2\nu z}{v_f}\sqrt{1/\alpha^2-\tilde{p}^2}} r^s(\tilde{p}) \tag{2.3.21}$$

$$r^s(\tilde{p}) = \frac{2i\sqrt{1/\alpha^2-\tilde{p}^2}\int_0^\infty \frac{d\tilde{\kappa}}{\epsilon_t/\alpha^2-\tilde{p}^2-\tilde{\kappa}^2}-\pi}{2i\sqrt{1/\alpha^2-\tilde{p}^2}\int_0^\infty \frac{d\tilde{\kappa}}{\epsilon_t/\alpha^2-\tilde{p}^2-\tilde{\kappa}^2}+\pi}. \tag{2.3.22}$$

In the regime of our interest $\alpha \sim 10^6$, we can replace $\sqrt{1/\alpha^2-\tilde{p}^2}$ with $i\tilde{p}$ to good approximation. Also, by separating the real and imaginary parts of the numerator and the denominator of equation (2.3.22), it can be shown that when $\nu/\omega \sim 10^3 \gg 1$, the imaginary part of r^s is well-approximated by

$$\mathrm{Im}\,(r^s) \approx \frac{\tilde{p}}{\pi}\frac{1}{\alpha^2}\int_0^\infty \frac{\mathrm{Im}(\epsilon_t)d\tilde{\kappa}}{(\tilde{p}^2+\tilde{\kappa}^2)^2}. \tag{2.3.23}$$

Finally, the substitution of equation (2.3.23) into equation (2.3.21) and the change of variables $\tilde{p} = r\cos(\theta)$, and $\tilde{\kappa} = r\sin(\theta)$, and $\tan(\phi) = 1/r$ give us

$$S_B^z = \frac{\hbar}{4\pi^2\epsilon_0 c^4}\frac{\omega_p^2\omega}{v_f}\, C\left(2\nu z/v_f\right) \tag{2.3.24}$$

where the dimensionless function $C(a)$ is given by

$$C(a) = \int_0^{\pi/2}\int_0^{\pi/2} d\theta d\phi \frac{\cos^3(\theta) e^{-a\frac{\cos(\theta)}{\tan(\phi)}}}{\sin(\phi)\cos^2(\phi)}\frac{3}{2}\left(\frac{\pi/2-\phi}{\cos(\phi)} - \sin(\phi)\right). \tag{2.3.25}$$

The function $C(a)$ has a logarithmic divergence $C(a) \approx -\frac{\pi}{2}\ln(a)$ in the limit $a \to 0$. This originates from integration over infinitely large momentum p in the integral in equation (2.3.3). Therefore, we introduce a physical cut-off, which modifies the range of integration for ϕ from $[0, \pi/2]$ to $[\phi_c, \pi/2]$ with $\tan(\phi_c) \equiv \frac{\nu}{v_f k_{\text{cut}}}$. Using $k_{\text{cut}} = 2\pi/a_{\text{Ag}}$ with $a_{\text{Ag}} = 0.4$ nm, the lattice spacing of silver, we obtain well-defined behavior in the limit $z \to 0$, $C_{\text{cut}}(2\nu z/v_f) \approx 4.6\pi$, which leads to Eq. 3 in the main text.

2.3.4 Spectral dependance of Johnson noise

From equation (2.3.17), it is clear that we expect the noise spectrum of magnetic Johnson noise to be white for frequencies over which $\coth(\hbar\omega/2k_BT) \approx 2k_BT/\hbar\omega$. We verify this by applying an external magnetic field, $B_{||}$, along the NV axis to tune the NV spin transition frequencies

$$\omega_\pm = \Delta \pm 2g\mu_B B_{||}/\hbar \tag{2.3.26}$$

where $\omega_{\pm}$ denotes the transition frequency from the $|m_s = 0\rangle$ to the $|m_s = \pm 1\rangle$ states, Δ denotes the NV spin ground state zero-field splitting ($2\pi \times 2.88$ GHz), and $g\mu_B$ is the NV electronic spin magnetic moment. We measure the relaxation rate when the NV is initially polarized in the $|0\rangle$ state, and when it is initially polarized in the $|\pm 1\rangle$ states. Based on the rate equations given in section 1.2 (equation (2.3.15)), the population relaxation from the $|0\rangle$ state is given by equation 2.3.16, while the population relaxation from the $|\pm 1\rangle$ state takes the following form:

$$\rho_{\pm 1 \pm 1}(t) = \frac{1}{6}e^{-3\gamma t} + \frac{1}{2}e^{-\gamma t} + \frac{1}{3}. \tag{2.3.27}$$

We observe excellent agreement with these predictions, and simultaneously fit to the relaxation from the $|0\rangle$ and $|\pm 1\rangle$ states with only a single decay rate γ. A representative data set and fit are shown in Fig. 1D of the main text. The extracted rates γ at different magnetic fields, and therefore different NV transition frequencies, are shown in Figure 2.8. We find good agreement with the hypothesis of a white noise bath, with $\chi^2/N = .87$, for the $\omega = 2\pi \times 2.2 - 3.6$ GHz range.

2.3.5 NV T_1 statistics

For NVs implanted at shallow depth such as the ones used in this work, we occasionally observe short NV T_1 times for NVs under bare diamond (see Table 2.2). The origin of the fast decay is unclear. No spatial correlations in T_1 are observed for the NVs

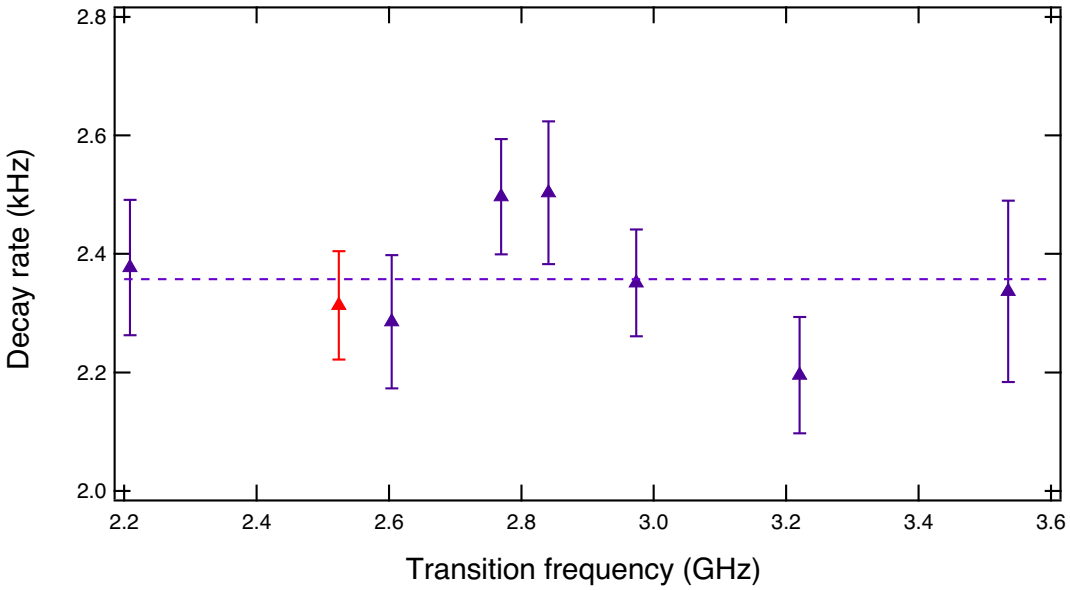

Figure 2.8: Johnson noise spectral dependance. We apply static magnetic fields to shift the NV spin transition frequencies. When polarized in the $|\ \pm\ 1\rangle$ state, the relaxation rate of the NV center is sensitive to the magnetic field noise at the frequency $\omega_{\pm}$ given by Eq. S26. The red triangle corresponds to the decay rate extracted from the data shown in Fig. 1D of the main text.

with reduced T_1 times.

2.3.5.1 Extraction of relaxation rates and distances under polycrystalline silver

As we would expect due to the variability in NV T_1 times under bare diamond, when measuring under silver we observe a spread in the T_1 times of the NVs, especially at larger distances from the silver, consistent with the variation we observe on bare diamond. This is because the Johnson noise only sets an upper limit on the NV spin lifetime, and other local sources of noise can still reduce it further. To compensate

Number of NVs	T_1
13	$\geq$ 2 ms
1	1.2 ms
1	500 μs
1	300 μs

Table 2.2: T_1 statistics for 16 of the NVs shown in Figure 4 of the main text (corresponding to the blue triangles in Figure 2.9D), in the absence of silver.

for this we measured 5-10 NVs at each point along the ramp, such that we can expect the maximum T_1 observed in at each point to be Johnson noise limited (10 NVs per points were measured for the 7 closest points measured from 20-80 nm, and 5 NVs per points for the other 7 points, from 100-200 nm). We then only include NVs with a spin-dependent fluorescence contrast within the expected range of 15-35%. The data plotted in Figure 2 in the main text is the inverse of the maximum T_1 measured at each point along the ramp.

In the theoretical prediction for the distance-dependent relaxation rate shown in Figure 2 of the main text, we include a correction to the lifetime predicted by equation (2.3.1) to account for the phonon-induced NV spin relaxation at room temperature, $T_1^{\text{ph}} = 6$ ms, consistent with our measured T_1 times under bare diamond and previous studies [25]. This is a significant correction only at larger distances from the film and only at room temperature [25], and has a negligible impact on the measurements and analysis presented in all other figures.

When estimating the distance to the film for the NVs plotted in Figure 2 in the

main text, the largest source of error is the variation in depth below the surface of the implanted NVs. As a result, we must also account for the statistical bias in NV depth introduced by selecting the maximum T_1 in each region. In particular, as most NVs have Johnson noise limited lifetimes, by taking the maximum T_1 measured we are likely selecting not only for an NV with a T_1 limited by Johnson noise, but also for the deepest NV in each region. To account for this, we assume the NV implantation depths are normally distributed, with a mean depth μ=15 nm and a standard deviation σ=10 nm [42]. Let $N_{\mu,\sigma}(x)$ denote the normal distribution representing the NV depth profile. If n NVs are randomly selected from this distribution, it can be shown that the probability the deepest NV selected has depth x is given by

$$P_{max}(x) = n\left(\int_{-\infty}^{x} N_{\mu,\sigma}(x')dx'\right)^{n-1} N_{\mu,\sigma}(x). \tag{2.3.28}$$

We use this new distribution to determine the expected value and standard deviation of the depth of the NV selected at each point along the ramp. For example, if we measured $n = 5$ NVs at one point along the ramp, from the above probability distribution function P_{max} we find that the expected value for the depth of the deepest NV measured is 27 nm with a standard deviation of 7 nm, while at a point where we measured $n = 10$ NVs the likely distribution of depths is 30 ± 6 nm. These depths are then added to thickness of the ramp at that point to give the total distance to the silver surface plotted in Figure 2 of the main text.

In the temperature-dependence measurements shown in Figure 3A, an NV-film distance of $d = 31 \pm 1$ nm is extracted from the fit to equation (2) in the main text. This is consistent with our expectations, as we expect a depth 15 ± 10 nm from implantation parameters, in addition to the 5-nm thick SiO_2 spacer layer.

2.3.5.2 NVs under single-crystal silver

In total, we measured the T_1 of 25 NVs close to the single-crystal silver sample at 12 temperatures, in three different spatial regions on the sample. Each region was 40 μm $\times$ 40 μm in size, and the regions were each spatially separated from each other by more than 100 μm. Of the 25 measured NVs, 16 were in region A (blue triangles in Figure 2.9D), where the diamond surface was observed to be in contact with the silver, 7 were in region B where a gap was expected to be growing between the diamond and the silver (pink squares in Figure 2.9D), and 2 were in region C, where the gap was expected to be fairly large (gray circles in Figure 2.9D).

The gap between the diamond and silver was qualitatively apparent based on a number of separate observations. We observed a variation in the brightness of the NVs in the different regions when exposed to the same laser power at the objective, which we attribute primarily to optical interference coming from the reflections off the silver and diamond surfaces. In addition, we measured reduced NV optical excited state lifetimes in region A (the region in contact with silver,) which we attribute to quenching from the silver (see Table 2.3). We also observed an accumulation of a

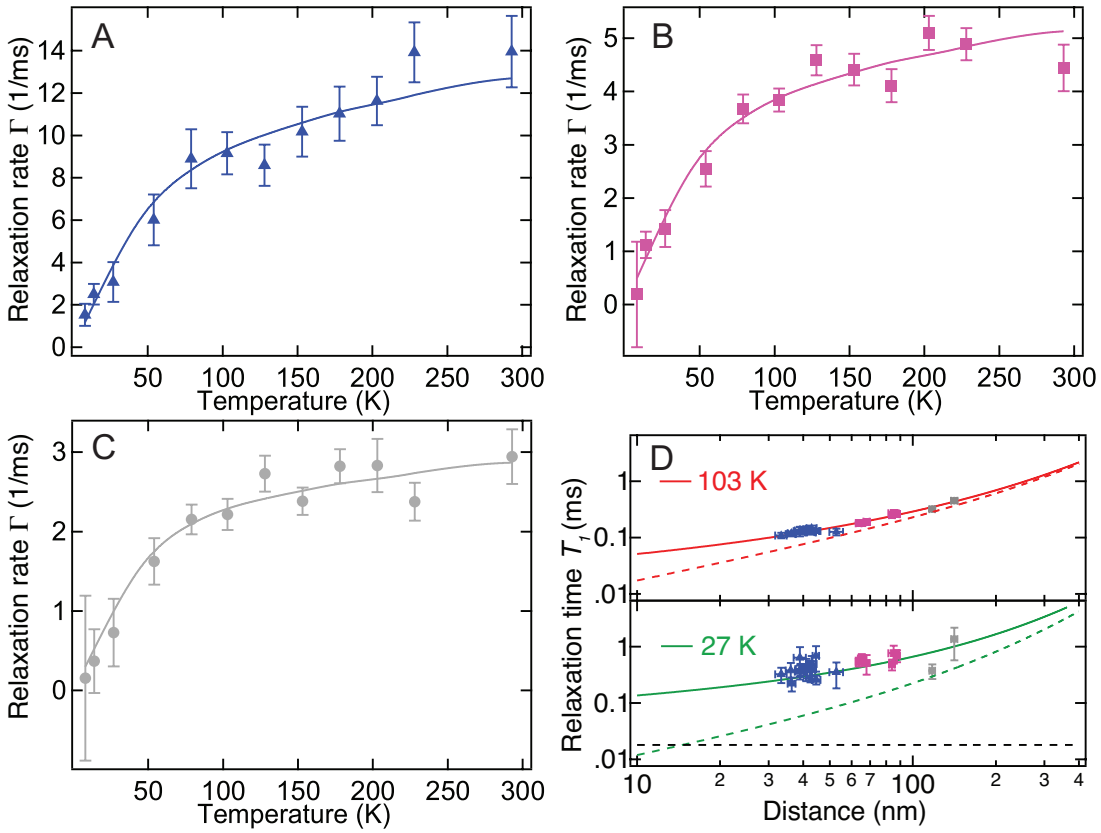

Figure 2.9: NV decay rates near single-crystal silver with non-local fits. **(A)** Data for an NV in the same region (region A) as the NV in Figure 4B of the main text. The extracted distance from the fit is $z = 33 \pm 2$ nm. This was the smallest extracted distance we observed for the single-crystal silver measurements. **(B)** Data for an NV in region B, where we expect NVs to be farther away from the silver film than in region A. The extracted distance from the fit is $z = 88 \pm 2$ nm **(C)** Data for an NV in region C, where we expect the largest separation between the NV and the metal film. The extracted distance is $z = 141 \pm 4$ nm. **(D)** The same data as in Figure 4D, measured T_1 versus extracted distance for two temperatures, 103 K (top) and 27 K (bottom), color coded by sample region (blue triangles in region A, pink squares in region B, gray circles in region C).

small amount of fluorescent background on the diamond surface over time in regions B and C, which was absent from region A, as would be expected if the diamond and silver were in direct contact there.

Region	Mean excited state lifetime
A	8.2 ns
B	12.5 ns
C	13.6 ns

Table 2.3: Mean optical excited state lifetimes by spatial region for the NVs show in Figure 4 of the main text and Figure 2.9D.

The T_1 time at room temperature of all 25 NVs was also subsequently measured after the silver sample was removed. Of these NVs, one NV in region A was rejected because the measured T_1 times under silver were not repeatable, and one NV in region B was rejected because it had very short T_1 times even at low temperatures (<300 μs at 8 K,) leaving 23 NVs that compose the dataset shown in Figure 4D of the main text and Figure 2.9D). The anomalous behavior of the two rejected NVs is not well understood, and could be the subject of further study.

3

Towards Strong Mechanics-NV Interactions

3.1 Introduction

An outstanding problem within the NV center community is that of being able to engineer a a strong interaction between separated NV centers. NV centers have boasted long coherence times, easy single-NV manipulation, state readout, and initialization, but have long not had scalable long range interactions — having such a mechanism would become an enabling technology that would allow the NV center to become a strong platform for quantum computing and simulation. One method to engineer such interactions is with the help of mechanical resonators [45, 52]. By placing a magnetically-functionalized mechanical resonator in the vicinity of two NV centers, the resulting interaction can give rise to an effective interaction between NV centers.

Unfortunately, however, the necessary requirements for such a system are difficult, and while this work does not achieve such a two-qubit interaction between NV centers, much of the necessary work in doing so is presented. This includes both demon-

strating high quality factor resonators with magnets deposited on them as well as reaching much higher couplings between resonator and NV centers than previously achieved.

For a derivation of the theory behind NV-NV engtanglement via magnetically-functionalized mechanical resonators, see Appendix C.

3.2 Experiment

A large effort in the past few years has gone towards trying to accomplish high cooperativities with these mechanical oscillators. While we hope to depend on the high decoherence and relaxation times of the NV center, the two main sources of uncertainty are that of the high mechanical Q factor under load and the high magnetic field gradients we require. In the following, we include details about the current state-of-the-art in magnetically functionalized mechanical resonators and magnetic materials for high magnetic field gradients.

3.3 Setup

The device fabrication is discussed in Figure 3.1, with exact recipes given in the Appendix.

For studies at low temperature, the entire device is placed on the coldfinger of a

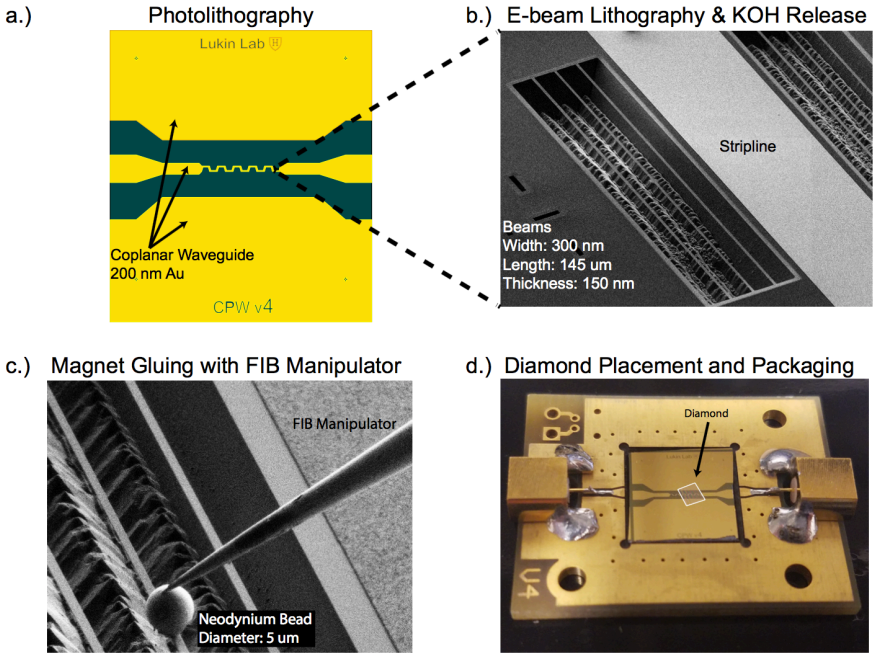

Figure 3.1: Diamond-Nanomechanics Device Fabrication Process. (a) First, a simple photolithography step creates a gold microwave coplanar waveguide on a silicon nitride-on-silicon substrate. (b) Electron-beam lithography is used to define long beams in the silicon nitride near the coplanar waveguide centerpin. These beams are underetched using a silicon KOH etch. (c) Next, a a FIB with manipulator is used to place down a spherical bead onto the beam; the bead is either stuck electrostatically or via a localized platinum deposition. In initial studies, stencil lithography was used to deposit metal via e-beam lithography (see Appendix). (d) A diamond is placed on top of the entire area with NV's close to its bottom surface. The entire device is wirebonded onto a separate PCB.

Montana cryostation. An interferometer is used for resonator readout.

3.4 High Quality Factor Loaded Resonators

One of the less explored frontiers in this research is understanding and verifying whether or not loaded resonators will result in a lower quality factors. For this study, we used doubly-clamped stressed Silicon Nitride mechanical resonators. In previous studies, such resonators have been shown to have high quality factors in vacuum conditions [57]; in addition, these mechanical resonators are promising for the current work in that they can be made to have low mass. However, tests under cryogenic temperatures and under load have not been investigated.

Here, we have demonstrated high mechanical quality factors under cryogenic conditions, even under magnetic load (see figure 3.2). For thin (300 nm) doubly-clamped resonators under cryogenic temperatures without magnet load, we measure quality factors of $> 1 \times 10^6$; at the time of this finding, this was not observed. Furthermore, we demonstrated quality factors above 4×10^5 for loaded mechanical resonators of larger thickness. Previous work has indicated that the larger thickness also plays a role in damping the resonator (in addition to the magnetic load), and thus these results were promising for use in coupling to NV centers.

At this point, the largest uncertainty in the experiment is that of the final coupling between NV centers and magnetic resonators, and so thinner resonators were not ex-

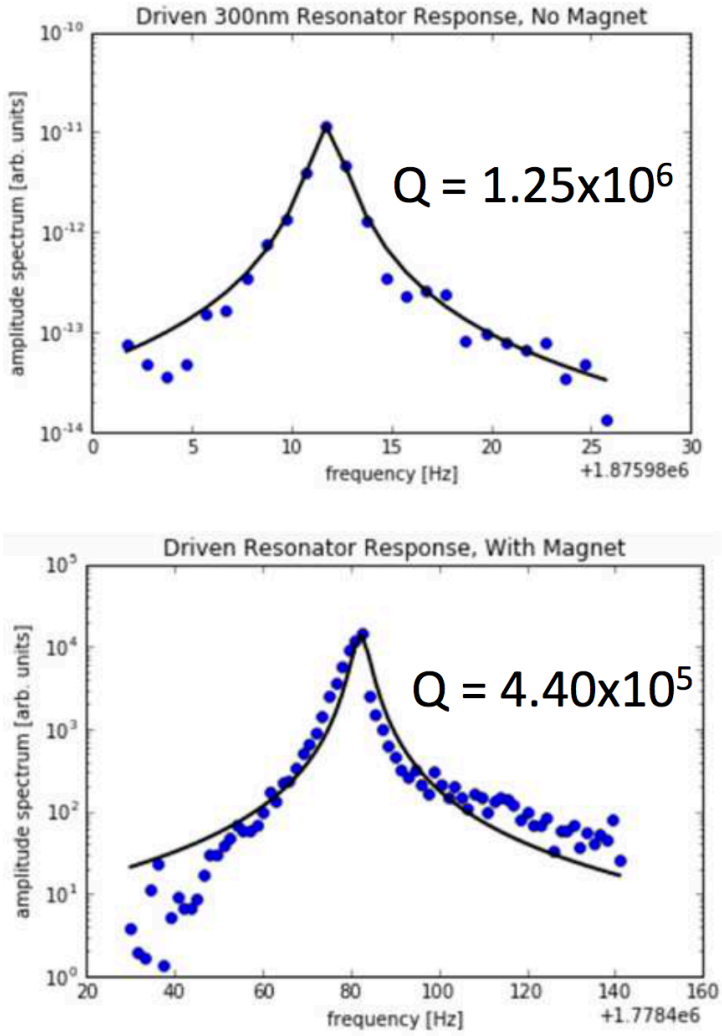

Figure 3.2: Resonator Quality Factors with and without Magnet Load. Under cryogenic conditions and with a nanomagnet placed in the center, the double-clamped silicon nitride resonators exhibited large quality factors ($> \quad 4 \times 10^5$). The above resonator is one that was thicker than necessary for the final experiment, and the quality factor may improve more upon using thinner quality factor resonators.

plored, although they are expect to achieve even higher quality factors.

3.5 Poor Gradients from Resonators with Deposited Cobalt magnets

The first devices utilized a magnet deposition procedure in which 7 nm Ti, $\approx$ 90 nm Co, and 10 nm Pt was deposited on the resonators; these were based on previous work in creating large-gradient fields [33]. Such devices, however, exhibited poor magnetic field gradients; see figure 3.3.

Notably, two clear issues persisted in these devices:

1. Poor magnetization. The cobalt magnets exhibited poor magnetization, and as a result, the magnetic fields emanating form them were not strong. This issue persisted despite attempts to magnetize the magnets in an external 3 T magnet. Unfortunately, similar issues have been seen with other magnets [32], and such issues are not easily diagnosed. Notably, XPS studies on larger magnets (fabricated in the same manner) indicated that the magnets were not becoming oxidized. Furthermore, there is no known technique for understanding the grain size of metal samples as small as those on resonators.
2. Large NV-Magnet distances. Although the diamond samples used in these studies are well polished (RMS $<$ 100 nm over large distances), keeping samples clean enough for less than a 2 um gap between diamond and resonator was difficult to achieve. Although never directly observed, we believe that the devices always had small dust or other similarly-sized contaminants between the diamond and device.

Furthermore, during this study, the evaporator used (Sharon EE-3) became unable to support pressures below $1 \times 10^{-}6$ Torr, and we also discovered that the green laser

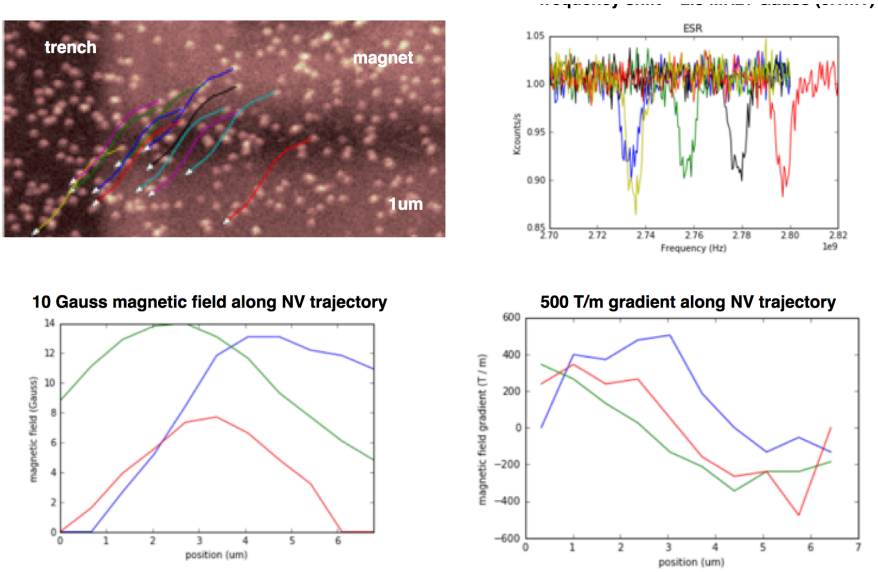

Figure 3.3: Poor Gradients from Cobalt Nanomagnets. (top-left) A confocal fluoresence image of the diamond over a magnetic bar. Arrows indicate the path the diamond makes as it is pushed on the surface of the device. (top-right) Exampe ESR spectrum of NV's tracked as they are passed over the magnetic bar. (bottom-left) Measured magnetic fields of NV's along their trajectories. (bottom-right) Inferred Magnetic field gradients along the given trajectories. The Magnetic field gradients do not exceed 500 T/m.

caused magnets to melt; unfortunately, evaporating the metal in another evaporator and using very low green light power did not result in larger magnetizations.

3.6 Improved Gradients with Resonators with Neodynium microbeads

One approach to dealing with the issues presented by the cobalt magnets is to try to used another magnetic material instead of cobalt. Here, we show improved coupling between Neodynium micromagnets and NV centers.

As discussed in figure 3.1, neodynium micromagnets are carefully placed down on mechanical resonators, and later magnetized with an external 3 T magnet.

The magnetic field gradient was measured in two ways. First, XY pulse sequences were used directly to become sensitive to specifically the resonance frequencies of the resonators; the resulting spin contrast as a function of pulse delay time is fit to a theoretical curve for the coupling between NV center and mechanical resonator (see figure 3.4).

Similar measurements were done more directly using ESR spectroscopy, but with an ensemble of NV's. See figure 3.5. In both cases, we observe high magnetic field gradients of $3-4\times10^3$ T/m, and a coupling of ≈ 1 Hz. Notably the diamond-resonator distance is still approximately 2 um.

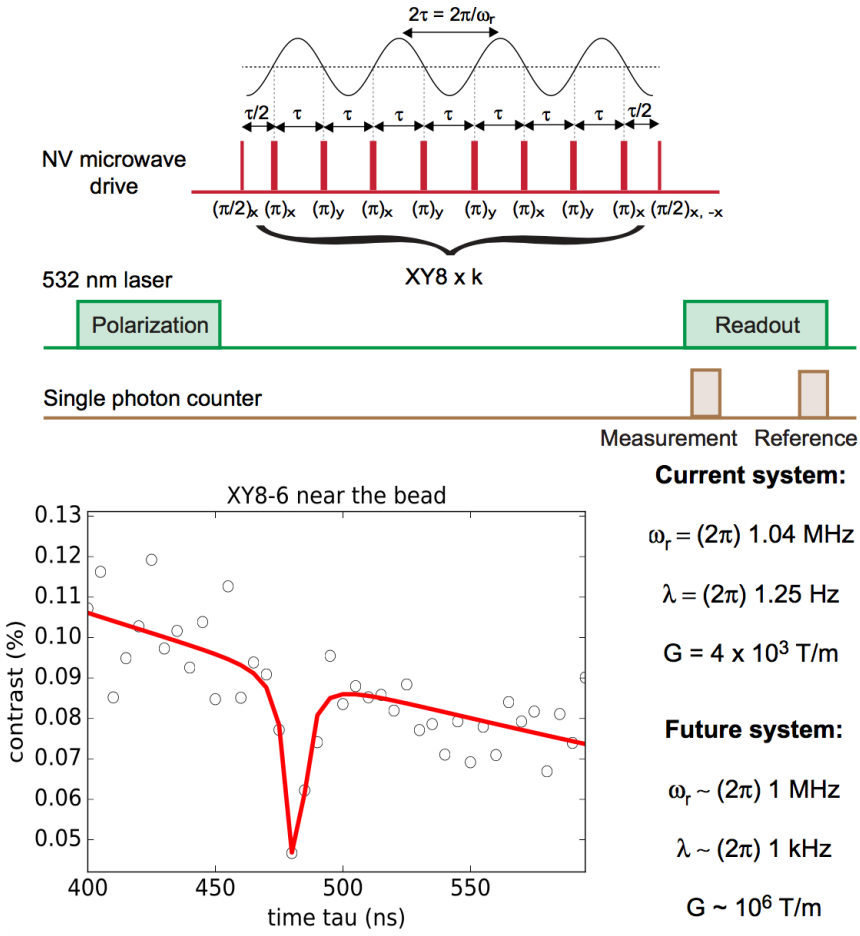

Figure 3.4: **Measuring the coupling between NV's and resonator via Pulse Sequences**. (top) An XY-8 pulse sequence is used to filter most frequencies of external magnetic field; in the case when the pulses are in unison with an external field, the resulting phase building results in spin contrast. (bottom) The resulting spin contrast is fit to a model indicating a high (4×10^3 T/m) magnetic field gradient.

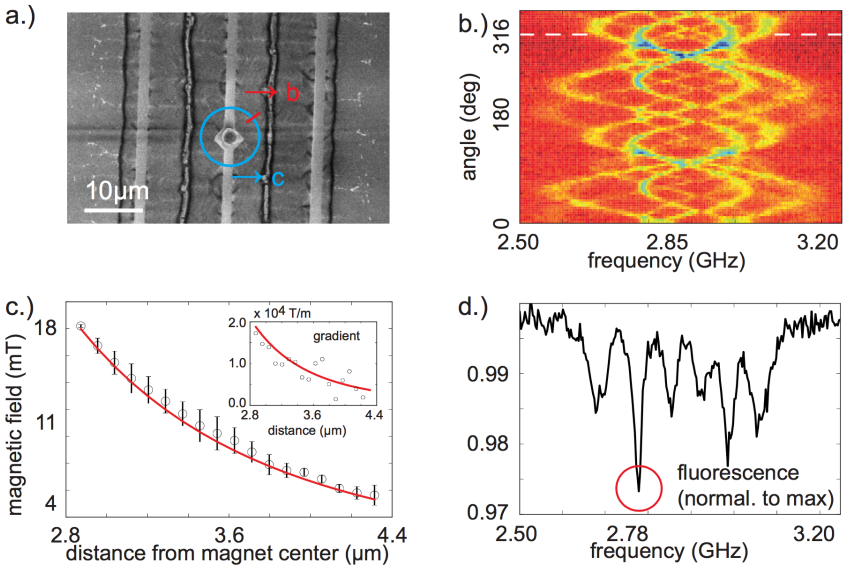

Figure 3.5: Measuring the coupling between diamond and resonator with an ensemble diamond. (a) A spherical micromagnet with diamond of 2.2 um is on a mechanical resonator. The blue outline indicates the positions along which ESR is measured (b) The resulting ESR scan. (c) The measured magnetic field field and magnetic field gradient as a function from distance to center, including dipole fit. (d) An example ESR spectrum.

3.7 Future Work and Conclusions

In this work, a strong effort was put towards creating high quality mechanical oscillators with high magnetic field gradients. The current work, however, still requires much larger cooperativities in order . There are two main thrusts in this project:

1. Continue improving cooperativies. The current work has not reached any fundamental limits in the final cooperativities that can be reached, and more work can be done in improving the magnetic field gradients. Such work would likely require improving the ferromagnets used in shape or material, and being able to bring NV centers closer to the magnets.

2. Consider other interesting applications. One interesting application that this work can lead to is that of mechanical resonator cooling — that is, utilizing the low-entropy (initialized) NV center to decrease the entropy in the mechanical oscillator state, and thus decrease its effective temperature (of that coupled mode). Such work is currently being investigated.

4

Initial Studies into Levitated Micromagnets

4.1 Introduction

A large subset of experimental quantum physics can be described as the study of gaining precise control over expertly isolated systems; the great plethora of systems studied gives insight into both completely new theories as well as new regimes of existing theories. One regime that is especially difficult to study is that of the behavior of spacial separated superpositions of massive objects, in which, for example, many fundamental decoherence mechanisms have recently been examined [43, 47].

Here, we study a promising new platform for such experiments: trapped, levitating magnets over superconductors [44, 48]. Such a platform is predicted to be very well isolated from its environment, and the leading order dissipation mechanisms are still not well understood. This platform has not yet been thoroughly studied experimentally, and thus making it a promising and exciting line of research.

Notably, the platform also is known to be promising for its extensions into hybrid

quantum systems, in which they can help mediate long-range interactions with NV centers, and as an ultra sensitive magnetometer [27].

4.2 Theory

The most basic theory of levitated magnets over type-II superconductors utilizes the so-called "Frozen Mirror Image Method" (or "Method of Frozen Images"), a small extension of the usual image dipole method taught in basic electromagnetism [28]. Consider a magnetic dipole with magnetization $\vec{m} = (m_x, m_y, m_z)$ some distance d above a normal metal occupying the $z < 0$ half space, after which the normal metal undergoes a transition into a type-II superconducting state. Our goal is to understand the resulting potential landscape for magnet to understand its dynamics.

4.2.1 Method of Frozen Images

A type-II superconductor will keep a memory of the initial magnetic field permeating through it. We approach the problem by substituting the superconductor with image dipoles that counter-act changes to the field in the lower half space. In the upper half space, we have that there are no free currents, and as a result we can define a magnetic scalar potential φ satisfying poisson's equation. Thus, in this particular setting, we can now focus on just finding image dipoles whose resulting magnetic field matches the perpendicular component of the magnetic field at the surface of the superconduc-

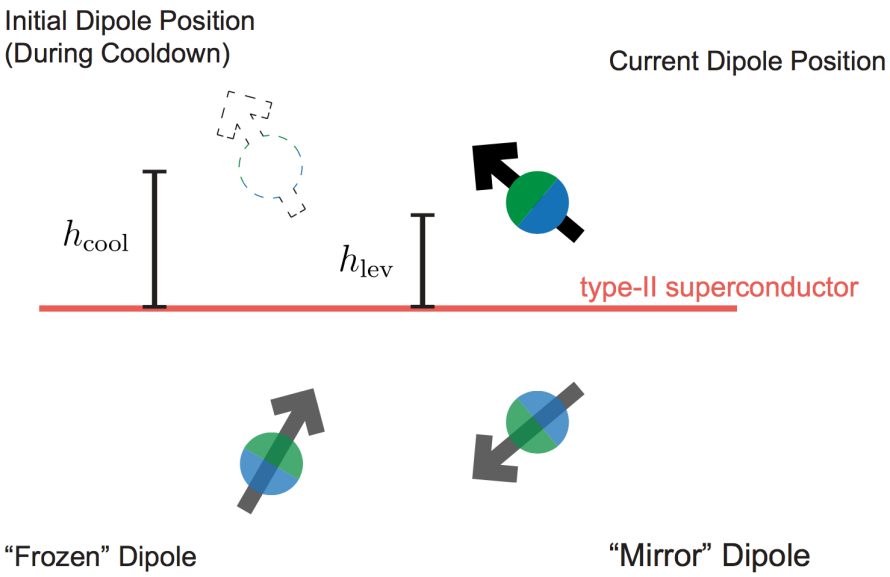

Figure 4.1: Method of Frozen Images. To model a dipole above a type-II superconductor, two image dipoles are used to derive the response field in the upper half space.

tor.

As a first step, if the dipole was originally cooled down at position $\vec{r}_{\text{cooldown}} = (0, 0, d)$ and is displaced to a position $\vec{r} = (x, y, z)$, we can cancel the perpendicular component of the magnetic field at the surface of the superconductor by placing an image charge at position $\vec{r}_{\text{mirror}} = (x, y, -z)$ with magnetization $\vec{m}_{\text{mirror}} = (m_x, m_y, -m_z)$. Notably, at this point, we have solved the problem in the case that the superconductor was type-I — that is, the superconductor expelling all of the magnetic field from permeating through it.

Next, we place another dipole at the position $-\vec{r}_{\text{frozen}} = (0, 0, -d)$ with magnetiza-

tion $\vec{m}_{\text{frozen}} = (-m_x, -m_y, m_z)$. The resulting perpendicular component at the surface of the superconductor is now the same as if the original dipole had never left its original "cooldown" position at $\vec{r}_{\text{cooldown}}$. Thus, we have found a set of image dipoles that satisfy the boundary conditions we were after, and thus can easily write the force on the (real) dipole to be the sum of the forces from each of the two image dipoles.

4.2.2 Potential

One is tempted to write the potential for the dipole, then, to be

$$V_{\text{wrong}}(\vec{r}, \vec{m}) = V_{\text{mirror}} + V_{\text{cooldown}} = V_{\text{d-d}}(\vec{r}, \vec{r}_{\text{mirror}}, \vec{m}) + V_{\text{d-d}}(\vec{r}, \vec{r}_2) \tag{4.2.1}$$

where $V_{\text{d-d}}$ denotes the usual magnetic dipole-dipole interaction. Unfortunately, this results in the incorrect answer; instead the correct potential is

$$V(\vec{r}, \vec{m}) = V_{\text{mirror}} + V_{\text{cooldown}} = \frac{1}{2} V_{\text{d-d}}(\vec{r}, \vec{r}_{\text{mirror}}, \vec{m}) + V_{\text{d-d}}(\vec{r}, \vec{r}_2), \tag{4.2.2}$$

where the factor of $1/2$ denote the fact that less work is done to the dipole as it is brought from far away since its mirror dipole is also moving with it. (One can compute the work done directly to get this factor of $1/2$) [53].

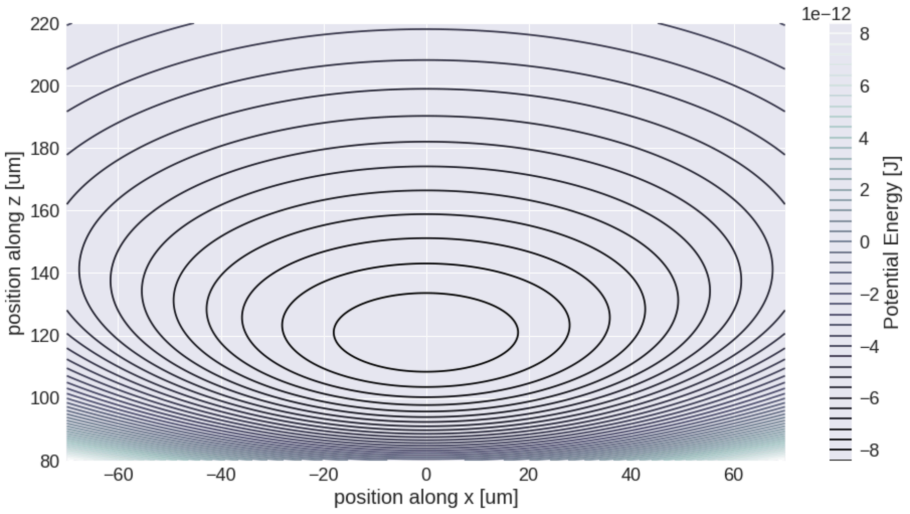

Figure 4.2: Example Trapping Potential for a Magnetic Dipole over a Type-II superconductor. The plot was derived assuming a cooldown height of 120 um.

4.2.3 Properties

There are a number of notable properties worth mentioning:

1. If the dipole never moves from its initial position or changes magnetization, then the derived image dipoles exactly cancel — exactly as one would expect, as the superconductor has no response if the original dipole does not move

2. The above would not be true for the case of a type-I superconductor; instead, the resulting single mirror dipole would cause a repulsive force no matter what orientation or position the real dipole had. Of course, it also wouldn't depend on the initial position of the dipole, either.

3. For a type-II superconductor, the resulting potential is actually a trapping potential — that is, any deviation from the dipole's original orientation or position results in a repulsive force.

Note that a good amount of theoretical work has been done in understanding trapped magnetic dipoles above type-I superconductors; the trapping is done by including a hole in the superconductor, causing a potential minimum in the x and y directions. Furthermore, gravity is included to include a force against the repulsive force of the superconductor, thus creating a 3D trap. While some early experimental work utilized a similar superconductor geometry, eventually the simpler setting of a full, smooth superconductor was utilized.

4.3 Experiment

4.3.1 Setup

To explore the dynamics of trapped magnetic dipoles over type-II superconductors, we utilized magnetized, spherical neodymium micromagnets (30-60 um diameter) over a commercial YBCO thin film (500 nm thickness). We used a custom-built apparatus that

- measures the motion of magnetic microbeads in any direction.
- properly controls for the cooldown height of the microbeads

A schematic of the setup is shown in figure 4.3.

Before placing a magnet on the membrane, a very thin ($\approx$ 7 nm) gold layer is applied to the silicon nitride membrane device to discourage strong adhesion between the magnets and silicon nitride or silicon. Furthermore, to ensure the YBCO film

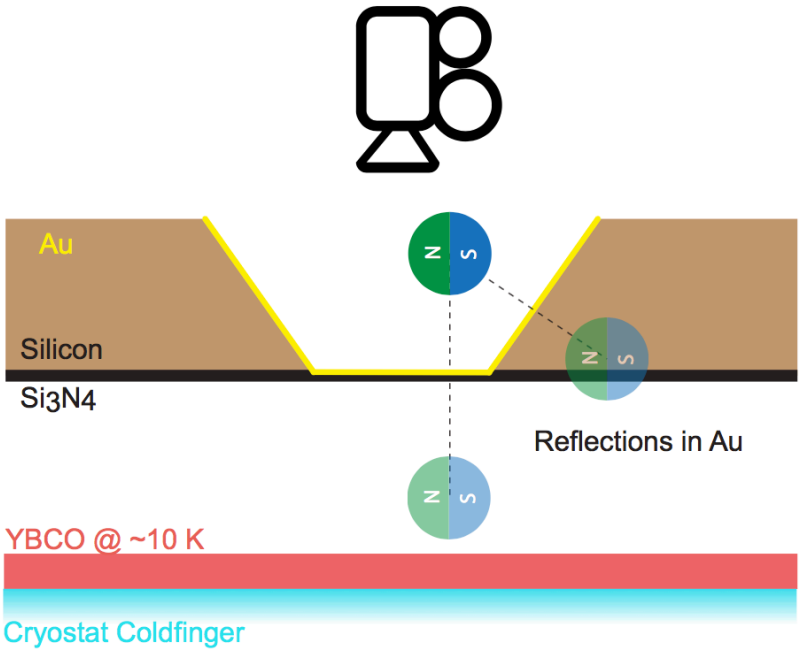

Figure 4.3: Levitated Magnet Setup. A single micron-scale bead is placed on a silicon nitride membrane. After the YBCO is cooled, the membrane is lowered until the bead comes off the membrane and is levitated and pinned. A microscope objective is mounted above the sample and data is taken with a camera. Notably, the smooth, sloped sides the membrane structure allow for imagining mirror images of the bead, allowing z-mode imaging.

and silicon nitride membrane device are parallel, the device is attached to a custom mount allowing for self-correction of small offset angles between the surfaces upon touchdown.

The silicon nitride membrane structure is created using the recipe given in Appendix A for patterned silicon nitride membranes, without the patterning steps. Following those steps, the devices are created by

1. Depositing 2 nm Ti and 7 nm Au onto the membrane pockets.
2. Placing magnets into membrane pockets utilizing a micromanipulator and tungsten tips.
3. A glass coverslip is glued on top of the pockets to ensure the magnets do not fall out.

4.3.2 Analysis

Video analysis was done in which the motion of the spherical magnets was automatically tacked frame-by-frame. The resulting brownian motion spectrum is given in figure 4.4. Notably, the high quality factor x, y, and z modes are well within the expected frequencies from the frozen image method.

Furthermore, one could excite the z mode and measure its frequency as it damps over time. This change in frequency is expected from the anharmonicity of the trap,

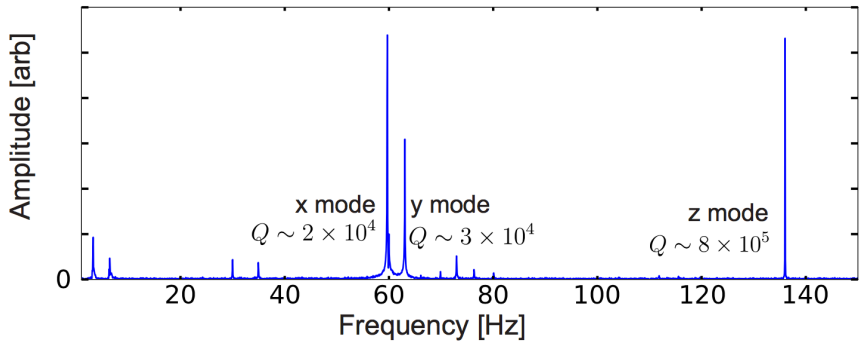

Figure 4.4: Levitated Magnet Motional Mode Spectrum. Applying a Fourier transform to the random motion of the bead reveals a number of motional modes, identified by later driving at these frequencies and studying the resulting video data.

and is expected to follow

$$\omega = \omega_0(1 + \gamma(A/z_0)^2) \tag{4.3.1}$$

with $\omega_0 = \mu\sqrt{3/8mz_0}$, A the amplitude of motion, z_0 the cooldown height, m the mass of the levitated magnet, and $\gamma \approx -2.58$ [28], for a dipole oriented along the z direction. Figure 4.5 shows strong agreement between the data and the expected anharmonicity

4.4 Future Work and Conclusion

We have demonstrated a novel experimental setup and a basic-level understanding of the motion of a levitating microsphere. There are a number of still unsettled ques-

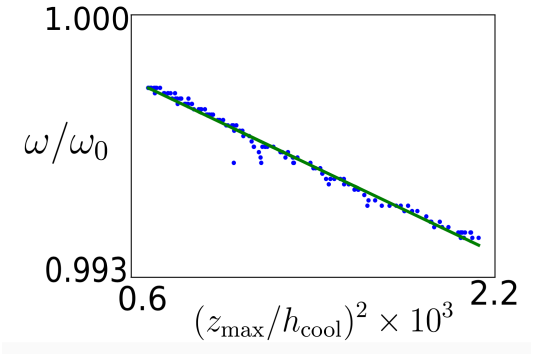

Figure 4.5: Levitated Magnet Z-mode Anharmonicity. The z-mode motion of the bead is found to have an amplitude-dependent frequency, consistent with the frozen image dipole model.

tions and clear lines for future work, some of the most pertinent are

1. A better understanding of the Brownian motion. The amplitude of the Brownian motion that the bead experiences is several orders of magnitude above what would be expected for an object in thermal equilibrium with its environment. Better understanding the possibly technical issues giving rise to the heightened Brownian motion would allow for cleaner future experiments.

2. Higher confidence matching of theory and experiment. Initial efforts, as discussed above, have given rise to a good match between theory and experiment, but there hasn't been enough study into a full match of all of the motional modes with the expected spectra from the method of frozen images.

3. Moving towards smaller beads. Smaller beads would result in high frequency modes; these modes are much more likely be decoupled from stray mechanical noise within a lab, and thus be more promising for most of the potential applications that necessitate strong decoupling with the environment

4. Integrating NV centers.

Such a system continues to be very promising for future development into quantum technologies and better understanding fundamental quantum effects.

5

pylabcontrol: Laboratory Equipment Control for Scientific Experiments

5.1 Introduction

A common struggle in an experimental physics lab is creating a computer platform for doing experiments — things like creating a computer interface to equipment, managing data I/O, and scripting common experimental control procedures, all with a high degree of trust, robustness, and reproducibility desired in a lab setting. Often, lab software is treated as a second-class citizen, and minimal effort is spent in creating a properly functioning experimental control platform. Unfortunately, this very often leads to both a lower quality of life in lab, having to deal with poorly documented half-working code, as well as an overall waste or resources as several people within a lab, or several labs around the world, re-implement very similar (if not identical) functionality of common equipment.

pylabcontrol is a software package that provides a streamlined tool for alleviating many of the pain points common in experimental physics labs. pylabcontrol

- provides a GUI for convenient experimental control
- interacts with any equipment that supports a python interface
- executes user-created scripts for complex experimental control procedures
- streamlines data acquisition, storage, and retrieval

pylabcontrol is built on python 3.6, and makes heavy use of PyQt5 for its GUI components. It properly utilizes version control (git), has a test suite for its core functionality, and contains full documentation. It is distributed under the GPLv3 license.

5.2 Philosophy

There are three main tenants to the philosophy behind pylabcontrol: smart default behavior, repeatability, and ease of use. Decisions about tradeoffs within the software often make reference to these tenants, along with general python development guidelines.

5.2.1 Smart Default Behavior

When creating an experimental control sequence or computer hardware interface from scratch, extra effort is required to develop certain clear but near-universal desirables, including

- autosaving data and experiment information, especially in the presence of software or hardware errors,

- an indication of progress during an experimental control sequence (e.g., via updating visualizations and/or progress bar),
- input validation

among others. pylabcontrol is built so that the above is handled gracefully within the software, with minimal effort required of a developer. This is largely achieved via inheritance from well-written base classes that do much of the heavy lifting, as is described in Usage.

5.2.2 Repeatability

One reason a large amount of effort has to go into repeating certain experiments is at least partially due to the fact that a very small portion of the information from the experiment is actually published. Furthermore, on a lower level, it is often the case that similar experiments need to be run in succession, or that experiments from months ago need to be referenced or re-run.

For easy of repeatability, pylabcontrol saves data and instrument/script information in a standardized manner. Data is always easy to to reference at a later time, and experiments can be reloaded and rerun at a later time.

This is done by creating a standard, common format for saving a script of instrument and script settings; settings are saved as json files within. Such settings are saved automatically during the execution of a script, but can also be saved separately at any time. These settings can then easily be imported into the provided GUI or be

easily parsed in future data analysis.

5.2.3 Ease of Use

Finally, a good amount of effort was put into creating software that was easy to use:

- Installation. Installation can be done using the standard python utility pip, and can be done in a single line.
- Documentation. Documentation for the code is fully available online.
- Minimal Coding. The extra overhead of utilizing the functionality in pylabcontrol is minimal to none compared to what otherwise would be the barebones code within a lab setting (see Usage).
- High-Quality reference code. A lot of effort has been put towards high-quality code, such that it can be easy to see how to code various different communication protocols and equipment. References to several different pieces of hardware can be found in the separate b26_toolkit package, where specific implementations of different hardware and Scripts can be found.
- Familiar, well established libraries. pylabcontrol uses matplotlib for its plotting, which is the current standard plotting library within python. Furthermore, it saves data in either json or csv formats, which are also among the most highly-used data formats for the sive of the data typically taken in smaller-scale physics labs. As such, many high-quality utilities already exist within python that can process the data.
- Automatic data I/O.

5.3 Prior Work

Several similar efforts have been undertaken in other labs [2, 10]. Notably, [2] has been expanded upon when moving to Google, but no updated libraries exist for general use and documentation of previous versions is centered mostly around the student developer's thesis. At the same time as this work, commercial software started to become available [AB], albeit closed-source.

Notably, much software for common equipment has already been implemented in python and is often available on Github; it is often easy to combine our software with pre-existing software (to control common optics equipment from Thorlabs, for example) so that research communities as a whole can be much more efficient and less time is spent on understanding each piece of equipment's peculiarities.

5.4 Installation

To install pylabcontrol, confirm python 3.6 or above is installed, and simply write

```
>> pip install pylabcontrol
```

in the command line or terminal. All dependencies should be automatically installed.

5.5 Usage

5.5.1 Typical lab workflow

In a typical lab, there are four main types of code written:

1. Instrument Communication Code. The most barebones code involves being able to interface with a piece of equipment.
2. Experimental Logic Flow Code (Scripts). Such scripts utilize the instrument communication code to perform experimental procedures automatically.
3. User Interface Code. Many labs use a combination of text-based scripts as well as a user interface for interacting with their hardware.
4. Data analysis.

pylabcontrol standardizes the first three, while supplementing data analysis with a simple method to import data.

5.5.2 Using pylabcontrol: Instruments

A barebones instrument has the following structure:

```
from pylabcontrol.core import Instrument


class ExampleInstrument(Instrument):

    _DEFAULT_SETTINGS = Parameter('instrument_param1', 0, float, 'this
        is the first parameter, used for ...')
```

```
_PROBES = \{'probe1' : 'a value to read off of the instrument'\}

def __init__():

   pass # to be filled with initialization code

def update():

   pass # to be filled with code that changes parameters

def read_probes():

   pass # to be filled with code that reads the state of a device,

      'probe1'
```

The above has the main ingredients for an instrument:

1. An initialization function, usually used to initialize a connection to an instrument
2. Parameters that describe the names of the control knobs one has on an instrument
3. An update function, to perform the logic necessary to actually change the parameter in the physical object. Usually, the code here would include whatever communication protocol is necessary to interact with the instrument.
4. Probes that describe quantities that are not changed about an instrument, but are read off of the instrument. For example, a pressure gauge would have pressures read off, but never set. the read_probes function would then describe how to read those probes.

Notably, the above contains exactly what would be a barebones implementation of an instrument in python even without pylabcontrol, thus exemplifying little overhead to using our code.

The above code could then be used in the following manner:

```
import ExampleInstrument


instrument_instance = ExampleInstrument()

instrument_instance.instrument_param1 = 5
```

as one might expect from a pythonic interface.

5.5.2.1 Using pylabcontrol: Parameters

Parameters used throughout scripts and instruments in a lab, and in pylabcontrol, they have their own class: the Parameter class. There are four fields for the class:

1. The parameter name.
2. The parameter value (or a dummy value if it needs to be evaluated at runtime).
3. The parameter data type. This can be a list of explicit values (e.g. [0, 1, 2]) , or an explicit datatype (int, float, etc.)
4. A string description of the parameter. (optional)

The above create a more robust value for use throughout a scientific experiment, like checking to make sure values of only certain types are accepted. Also, they make it easy to distinguish between actual instrument or script parameters and miscellaneous class variables.

5.5.3 Scripts

A barebones script might have the following structure:

```
from pylabcontrol.core import Script


class ExampleScript(Script):

   _DEFAULT_SETTINGS = Parameter('script_param1', 0, float, 'this is
       the first parameter, used for ...')

   _INSTRUMENTS = \{...\}

   _SCRIPTS = \{...\}

   def function():

      # to be filled with code that performs the script logic

      # example:

      self.data['voltage_sweep'] = voltage_sweep

      # ...
```

From the above, it is clear that scripts are made up of parameters (the default settings), the instruments that are necessary for the script, and subscripts the script might call upon. The script logic goes into the `function()` function.

Throughout the runtime of a script, data should be saved to the `data` class variable, and it will automatically be saved when calling `Script.save(save_path)`. Us-

ing the pylabcontrol GUI

5.5.3.1 optional Script uses

Using the Script base class allows for a number of useful usecases, including

- Plotting. By including a `plot(axis_list)` function that takes a length-2 list of matplotlib axis objects, the GUI will regularly plot the data during the runtime of the Script.
- Script Progress. One can include calls to `self.updateProgress(value)`, where `value` includes the current progress (in percentage) of the script. The GUI will then interpolate to find the expected amount of time remaining in the script. Data is plotted with each call.
- Logging. Often, text updates are useful within a script — instead of outputting to STDOUT with python's built-in print() function, one can use the self.log() function to give text updates during the runtime of a script. This would later be saved with the Script results, and can be useful to indicate the status of a script during its runtime. To use the functionality, utilized the `self.log(message)` function during the runtime of a script.

5.5.4 Data analysis

For data analysis, a typical use case for pylabcontrol looks something like

---

```
from pylabcontrol.core import Script
```

```
data_path = # to be filled with the path to the data

data_from_experiment = Script.load_data(data_path)
```

and the data that was taken during script runtime. No need to remember exactly how the data was saved!

5.6 GUI

pylabcontrol comes with a powerful, flexible GUI that is often the preferred method for running experiments in a lab — the GUI gives realtime insights during the runtime of a script. The GUI is also a convenient tool for making small changes to instruments without requiring the use of text code.

Running the GUI is as simple as going to a terminal or commandline and running

```
>> pylabcontrol
```

Instruments and Scripts can be imported into the GUI after first exporting them from .py files to json configuration files — this can be done by going to File-> Export Instruments or Scripts. Following that, Scripts and Instruments can be loaded as necessary using the load Instruments or Scripts button.

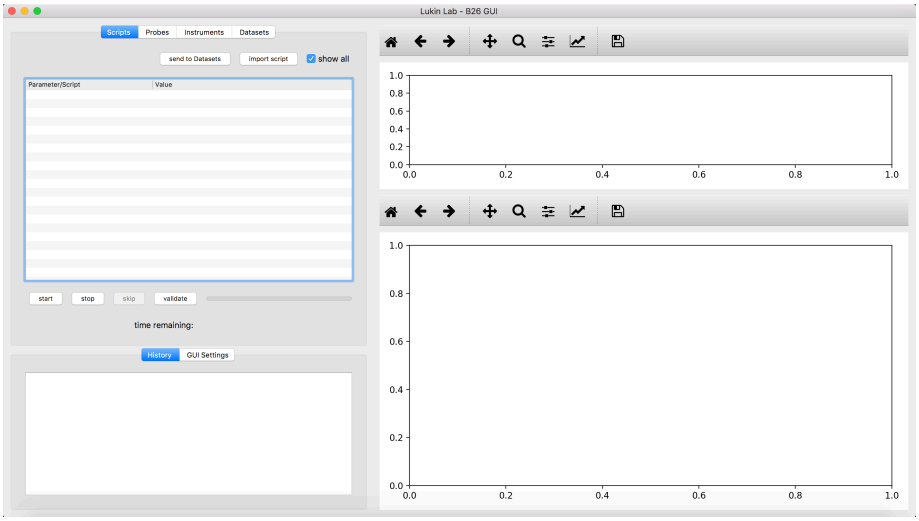

Figure 5.1: The pylabcontrol GUI. (top left) The Script, Probes. Instruments, and Datasets pane. Here, parameters of Scripts and Instruments can be quickly changed, and datasets can be looked at later. (bottom left) History and GUI settings. The History contains all output from the log, and GUI settings include paths for where scripts and current GUI settings are saved. (top right, bottom right) Plotting areas for scripts and datasets, including basic interactive tools (magnification, panning).

5.6.1 Advanced Features

While not strictly necessary, there are two other utility features that deserve a highlight: Datasets in the GUI and ScriptIterators.

Often one runs the same or a similar Script multiple times within a GUI, and has an interest in being able to compare data between separate runs of the Script. Of course, one could save each run of the script, and compare the resulting data either by directly comparing the automatically produced jpeg plots or doing data analysis in a separate program. However, one can often litter their harddrive with unnecessary saved Scripts or it can become cumbersome to perform separate data analyses after each (potentially quick) run of a script. Instead, one can send a finished scripts to the "Datasets" tab. Here, script data is saved and can be both referenced and saved later — thus, even after a script is run.

ScriptIterators allow a user to conveniently create combinations of scripts without the overhead of creating a whole new Script file. Often, there are fairly typical extensions to experimental sequences that might interest a user — for example, running a script multiple times. When importing a Script, a user can create a ScriptIterator; with barebones pylabcontrol, two possible ScriptIterators are possible: being able to run a script multiple times, and a parameter sweep script iterator. The latter allows the user to run a script over and over again while changing a single parameter within the Script.

It is also possible to create custom script iterators, as can be seen, for example, in the b26_tookit package.

5.7 Future Work

The current version of pylabcontrol is already very likely to be a much stronger software platform for experiments than is currently used inmost physics labs. That said, there are some clear avenues of improvement that are currently being considered, including

1. Plot settings in the GUI. Currently a Script can only output at most two different plots to the GUI; it is useful to change attributes of those plots during or after the runtime of a Script, or plot different data all together during the run of a Script. A typical example would be to be able to toggle between data from the average of many runs or data from a single run, for example. Currently, the GUI supports a limited amount of interactivity via matplotlib's interactive mode, but it is a far cry from the level of interactivity that would be desired in such a program. As such, the GUi can be expanded to include user-configurable plot settings for each Script, and the GUI can dynamically change the current data to plot based on those plot settings.
2. Less overhead for Instruments. Currently, it is necessary to include an empty `PROBES` field and a dummy `read_probes` function in order to create a barebones instrument. These should instead be taken care of by the Instrument class.
3. A client-server architecture. Currently, only the person that is utilizing the same computer that an instrument is plugged into can effectively develop code for it; if instruments were instead connected to a server, several clients can connect to the server to test these instruments.
4. Better external ScriptIterator integration. Currently, there is no simple way to create custom ScriptIterators.

Further current improvements can be found on the source code's github page.

5.8 Conclusion

Included here is much of the barebones functionality included with pylabcontrol; other very useful functionality (e.g. many of the GUI features) has not been discussed for the sake of brevity. Much of it can be found in the official documentation.

A

Appendix A: Cleanroom Recipes

A.1 Patterned Silicon Nitride Membranes

A.1.1 Resist Spinning

1. Wafer Prebake for Moisture Removal. Set the wafers to be processed on a hot plate at 180 C to bake away any residual water on the surface. Leave them there for 5 minutes.

   (a) Pro tip: Put aluminum foil down on the hot plate first if it is dirty

   (b) Note: The 5 minutes is pretty flexible

2. Wafer cleaning (optional). If the wafers are not clean, consider either sonication in acetone and isopropanol or a dynamic clean in which acetone and IPA are sprayed at the wafer while it spins on a spinner.

   (a) Pro tip: Wafers from SVM typically come quite clean, but this step doesnhurt either.

3. HMDS Spinning. Spin HMDS at any spin speed 2000-4000 RPM for 15-20 seconds

   (a) Pro tip: SiN can sometimes stick quite poorly to resist, so HDMS is a good idea.

   (b) Note: HDMS is supposed to be a single monolayer on the wafer, and often requires a much shorter spin time. It should be visually clear when the HDMS has finished spinning, as there will be no dynamic interference effects on the wafer during the spin.

4. HMDS post-bake. Bake the wafer for 1 minute at 115 C.

5. Resist Spinning. Spin 1813 resist on the wafers at 3500-4000 rpm (45 sec - 1 min)

(a) Pro tip: Don't use resist that has been left out in ambient conditions (i.e., not in the bottle and exposed to the flowing air) for more than 5-10 minutes.

(b) Pro tip: The wafers will likely be hot from the previous step — consider doing a full spin on the wafer so that it properly cools before applying the resist. This is a good tip to test a flaky spinner, as dealing with a wafer with unspun resist on it is a challenge.

(c) Pro tip: If the wafer comes out with uneven resist (often because of dust, for example), it is actually likely totally fine as long as you have relatively large (3 micron or more) features.

(d) Note: Edge bead removal is not necessary (and likely a bad idea).

(e) Note: Other resists would likely work perfectly fine as well, with a preference for thicker ones to ensure it does not get eaten away during later dry etching. Exact dry etching selectivity should be looked into to be precise.

(f) Sub-Pro tip: Any other resists used should be checked that they will work well with later dry etching machines, as dry etchers can reach high temperatures that cause some resists to bake onto the wafers.

6. Resist post-bake. Bake the resist at 115 C for 1 minute.

7. Store wafer. Store the wafer in a wafer carrier for exposure

   (a) Note: it might be a good idea to wrap the wafer carrier in aluminum foil to ensure it does not get exposed to too much UV light, but this might just be superstition.

Special note: In previous runs of this recipe, resist was spun on both sides of the wafer to ensure that both sides of the wafer are shielded from dust and contaminants, but the above recipe should work nonetheless.

A.1.2 Exposure

This lithography typically contains one side with small features, later to become the apertures through which material is deposited, and another side that acts as openings for silicon etchant (KOH) to eat away at the bulk silicon and expose those apertures from the other side of the wafer. The latter often has (relatively) large openings (>100 microns), while the former can have quite small features. In previous runs, the side with the smaller features was exposed first, but the order of exposure was not looked into in detail.

This process is a 2-sided (aligned) lithography process, but has very lax alignment requirements. Backside alignment to within 10 microns should be sufficient.

S1813 has a fairly wide exposure window (40-120 J/cm^2, I believe) that only needs to get tweaked if trying to write small (1-2 micron) features. Otherwise, I recommend exposing for 100 J/cm^2 total UV exposure

Pro tip: It is worth checking to see if the mask aligner lamp's intensity has been recently measured, as the intensity can vary by 4x over the lifetime of a UV bulb.

When exposing the side of the wafer that will act as openings for the silicon etchant, ensure that those rectangular openings have sides parallel to the major and minor flats of the silicon wafer. This doesn't need to be less than a degree of accuracy, but will screw things up if it is quite off.

A.1.3 Development

Unless you are going for especially small features, development should just work:

1. Developer Prep. Prepare two dishes (for example, two crystallization dishes from the equipment list), one with DI water and one with CD-26 developer (at least 1.5 cm up from the bottom of the dish).
2. Developer Dunk. Place the wafer in CD-26 for 1 minute
    (a) Pro tip: Aggravate the dish during development — i.e., swishing the fluid in different patterns. This helps make the development time more reproducible.
3. Wafer Rinse. Place the wafer in the water bath for 1 minute
    (a) Pro tip: if DI water taps are available, run the wafer under a DI water stream before placing it into the water bath, and CD-26 doesn't dissolve that well in water.
4. Blow dry.

A.1.4 SiN Etching

Misc. Comments:

Most RIE machines have a pre-clean process; a pre-clean is recommended.

To ensure that all of the SiN is etched away, typically recipes to etch SiN are overshot by 25-50 nm. Note: It doesn't matter if some Si is etched away.

Often grease or oil is used between the carrier wafer and wafer-to-be-etched to ensure good thermal conductivity — this may be recommended. Photoresists may bake on the wafer if they get too hot. (unremovably so).

A.1.5 Resist Removal

Resist can be removed in a variety of ways, two of which are mentioned here. The aggressive removal should be done in cases where the wafer has clear dirt that does not come off otherwise and the wafer should be especially clean (should be considered before KOH etching, for example, but isn't strictly necessary).

A.1.5.1 Normal Removal (Remover-PG)

1. Place wafer in a covered dish with remover-PG for 10 minutes at 80 C
2. Perform a typical wafer clean (some combination of DI, Acetone, Methanol, and IPA)
    (a) Pro tip: Blow dry out of DI or (preferably) IPA.

A.1.5.2 Aggressive Removal (Piranha)

1. Put wafer into container of Piranha etch for 10 minutes
    (a) Note: Use a 1:3 ratio of hydrogen peroxide to sulfuric acid. Don't use a higher ratio of hydrogen peroxide.

2. Perform a typical wafer clean (some combination of DI, Acetone, Methanol, and IPA)

    (a) Pro tip: Blow dry out of DI or (preferably) IPA.

A.1.6 Second Run

The above steps, including resist removal, should be re-done while exposing the other side's pattern. If the wafers look especially dirty, consider a piranha clean.

A.1.7 Si Etching in KOH

The following instructions roughly boil down to etching the entire wafer in an 80 C bath for approx 5 hours. It includes information about how to use a hotplate to do this, although Stanford does have wafer baths that might make this process simpler.

1. Start with a patterned wafer with no resist.
2. Preheat Water bath. Set up a hot plate with a large crystallization dish (a crystallization dish that can hold the smaller crystallization dish that can hold the wafer) and DI water (approx 2 cm from bottom). Set up the hot plate thermometer to be in the water, and set to 80 C.

    (a) Pro tip: Depending on the hotplate, the water can take a while to reach 80 C. I typically do this 20 min in advance.

3. Prepare KOH etchant solution. Combine (1) 100 mL DI water, (2) 20 g KOH pellets, and (3) 2 mL IPA. Place into water bath with watch glass on top.

   (a) Note: Be sure to still have the thermometer in contact with the water bath!

   (b) Pro tip: the 2 mL IPA is easily measured out with a pipette.

4. Etch Wafer. Place wafer, large feature side up, into the etchant solution for 3.5-5.5 hours, until clearly finished. Place a magnetic stirrer on top of the wafer (and turn on stirring). Place watch glass on top.

   (a) Pro tip: Bubbles should form in the exposed silicon areas.

   (b) Pro tip: Given the large variance in etch time (likely due to not directly measuring temperature of the solution), the etching is considered over when the stencils are clearly etched through. Note that it is fine to overetch quite a bit in this recipe, but underetching is not good (SiN does not etch at all in KOH). The wafers are ready when there are little to no bubbles forming in the areas and you can see through the newly created windows.

   (c) Pro tip: Not all windows will etch at exactly the same rate, and it is likely you will see a gradient across the wafer in etch times. (This is fine, wait until all are done.)

   (d) Pro tip: While the etch does not need to be supervised, it should be checked on at least every 30 minutes. For example, the water level may become low in the water bath and require refilling (even far before the wafer is expected to fully etched).

   (e) Pro tip: Read step 5 before the wafer is finished.

5. Place wafer into heated water bath. When etching is finishing, carefully remove the wafer from the KOH bath and transfer to a 80 C DI water bath (in a pre-heated crystallization dish on another hotplate, for example). Turn off the heating.

(a) Pro tip: If the wafer is transferred to room temperature water, weird crystals grow on it. It is important to transfer it to hot water.

(b) Pro tip: Try to remove the wafer by only either (a) sliding it out of solution by pulling the wafer out with a velocity mostly parallel to the surface of the wafer and (b) when necessary, lifting it in the direction perpendicular to the wafer very slowly.

6. Blow Dry out of IPA or another DI water bath.

A.2 Silicon Nitride Doubly-Clamped Beams

1. Spin ZEP resist on SiN on Si wafer
2. Using an E-beam tool, expose two rectangles separated by the resonator width, each having length equal to the length of the resonator.

   (a) Note: This may require a reasonable amount of tuning to get the features right.

3. Develop ZEP resist. (1 min in O-xylene, 30 seconds in IPA)
4. Check features are as expected!
5. Using a dry SiN etch tool, etch exposed SiN
6. Using the Si KOH etch recipe in the previous section, etch for $\approx$ 45 minutes

A.3 Resonator Magnet Integration

Using the tools of the previous section, magnets can be deposited on the resonators creating a device as show in figure A.1. A mask is placed over the resonators carefully using a mask aligner; the mask aligner UV light then cures UV glue. The whole package is taken to an evaporator; post evaporation, the mask is carefully taken off.

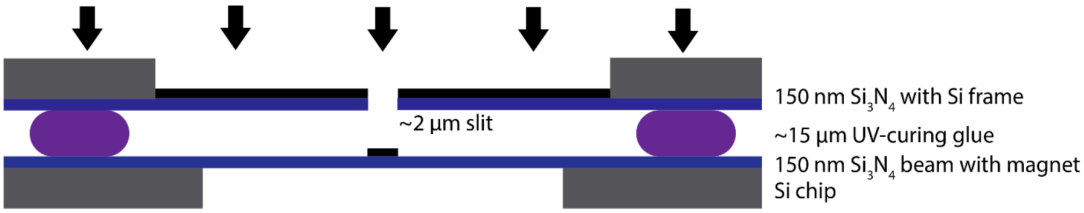

Figure A.1: **Magnet Fabrication on Mechanical Resonators** A stencil mask is carefully placed using UV curing glue above the mechanical resonators. Metal is evaporated onto the mask and exposed resonator area.

A.4 Material Ramp

The ramp fabrication is described below.

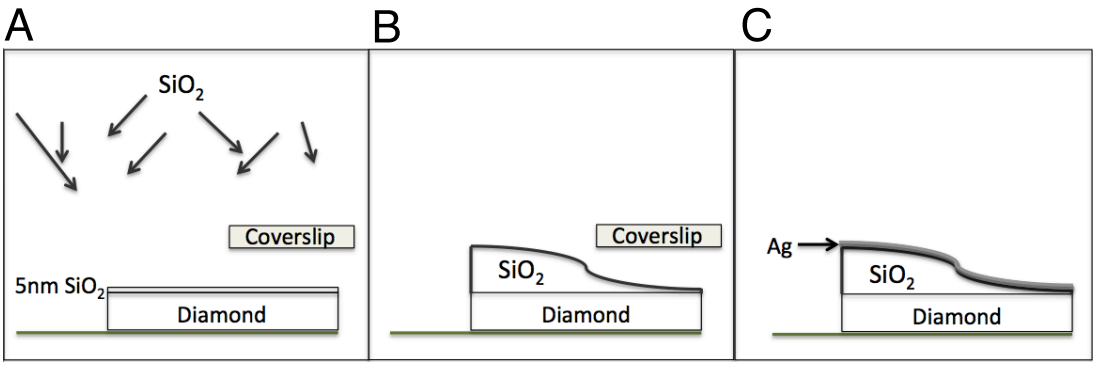

Figure A.2: **Silica ramp fabrication procedure. (A,B)** Following a 5 nm uniform CVD pre-deposition of SiO_2, a silica layer of gradually increasing thickness is fabricated on a diamond sample by placing a raised coverslip (raised $\sim$ 300 μm) over the diamond, and growing the silica layer via an anisotropic CVD process. **(C)** A final 60 nm layer of silver is deposited on the ramp, so that NV centers at different points along the diamond are different distances away from the silver film.

B

Appendix B: In-depth Theoretical Derivation of Johnson Noise from Material Half-spaces

B.1 Overview

We wish to find the spin relaxation rate induced by magnetic field noise from a nearby metallic half-space at finite temperature. Intuitively, thermally excited current noise (i.e., Johnson Noise) radiates magnetic fields; these uncontrolled magnetic fields couple to the spin and are a spin relaxation mechanism. We assume a spin splitting ω_L, coming from an external magnetic field and/or an inherent anisotropy in the electron wave function inducing a quantization axis and splitting. The calculation will have 3 main ingredients:

1. The Fluctuation-Dissipation Theorem
2. Calculation of the Electromagnetic Green's Function of the system's geometry
3. Time-dependent perturbation theory (Fermi's golden rule)

B.2 Fluctuation-Dissipation Theorem

The F-D Theorem seems like sort of a magical thing to me, and despite spending a bit of time reading up on it, it's still not quite intuitive for me. Regardless: it states that for a system in thermal equilibrium (our metal in this problem), the cross-spectral density of the fluctuations of some observable, $\mathbf{F}$, is related to the imaginary part of

the Fourier-transformed susceptibility, $\chi(\omega)$:

$$\mathbf{S}_F^{i,j} = \epsilon_0 \hbar \omega^2 \coth\left[\frac{\hbar\omega}{2k_B T}\right] \mathrm{Im}[\chi(\omega)] \tag{B.2.1}$$

where

$$\mathbf{S}_F^{i,j} = \int_{-\infty}^{\infty} d\tau \langle \mathbf{F}_i(\mathbf{r}, t+\tau)\mathbf{F}_j(\mathbf{r}, t)\rangle e^{i\omega\tau} \tag{B.2.2}$$

From a high-level point-of-view, the F-D theorem tells us that to know our thermal noise spectrum we only need to understand the system's reaction to an external force when it isn't in a thermal state. I've seen some references say something along the lines of "A system at zero temperature will react to an external force the same way it would if that external force were instead thermally induced." In my reading, I've basically seen it as a shortcut in the calculations like are done in the note. More specifically, one could enumerate the current excitations in the metal (quantum mechanically, quantize the currents in a metal), weigh the excitations with the proper thermal populations, and calculate what the expectations and variances of certain observables will be due to those currents. The F-D theorem is in this sense a shortcut so that we don't have to do this. It is similarly applied to the case of Brownian motion and the classic Johnson Noise calculation.

The observables we care about in our system are the electric and magnetic fields[1];

[1]Well, really the magnetic fields, but we get the electric field results for free along the way,

in what follows, I will only mention the electric field, but the results in this section analogously hold for magnetic fields. In our case, for example, we could write

$$\langle \mathbf{E}(\mathbf{r},t)\rangle_t = \langle \mathbf{E}(\mathbf{r},t)\rangle_{f=0} + \int_{-\infty}^{t} \mathbf{f}(\tau)\chi(t-\tau)d\tau \tag{B.2.3}$$

for some zero-force fluctuations $\langle \mathbf{E}(\mathbf{r},t)\rangle_{f=0}$, susceptibility χ, and generalized force f. This statement is powerful for us in this situation because we have a good grasp of the ingredients necessary in the terms above. Specifically, first we know that there should be no net average electric field as we average over time but apply no perturbation:

$$\langle \mathbf{E}(\mathbf{r},t)\rangle_{f=0} = 0 \tag{B.2.4}$$

The susceptibility χ is actually a well-known parameter in classical E&M, but it's rarely called the susceptibility. Read on!

---

so we might as well

B.3 A Glimpse of The Electromagnetic Green's Function

First, we assume that the "force" we apply to our system can be translated into an applied current distribution[2]. However, the catch here is that the electric field at point r depends on the current everywhere in space. To reflect this,

$$\langle \mathbf{E}(\mathbf{r},t)\rangle_t = \int_{-\infty}^{t} d\tau \int_r d^3\mathbf{r}\ \chi(\mathbf{r},\tau)\mathbf{j}(\mathbf{r},t-\tau) \tag{B.3.1}$$

Let's get one thing straight: yes, there should be a contribution from the charge distribution as well. However, we expect charge fluctuations to not be the dominant source of our noise. Current excitations are far more prevalent at the temperatures we are working in than plasmonic excitations. Furthermore, at the end of the day we care about magnetic field fluctuations, and to first order, those are just given by the currents in the metal.

In its current generality, equation B.3.1 allows for the current density at all previous points in time to influence what the current electric field is. We simplify matters by assuming that the electric field responds instantaneously to changes in the current

[2]At the end of the day, really the only things that can be the source of E-M fluctuations are charge or current distributions, and if you are picky, a specially dependent polarization and magnetization

density:

$$\langle E(\mathbf{r},t)\rangle_t = \int_{\mathbf{r}} d^3\vec{r}\,\chi(\mathbf{r},t)\mathbf{j}(\mathbf{r},t) \tag{B.3.2}$$

Now, we assume that the electric field distribution at the current time can be fully described by the current distribution at this point in time, and as such, although we include the possibility for the response of the system to depend on the current distribution at all earlier times, we don't need to include it in our problem. Instead, however, we *do* need to include that the electric field at any point r in space depends on the current density *everywhere*, and so the response of the system is given by

$$\langle \mathbf{E}(\mathbf{r},t)\rangle_t = \int d^3\mathbf{r}\ \mathbf{G}(\mathbf{r},t)\mathbf{j}(\mathbf{r},t) \tag{B.3.3}$$

Finally, I cheated along the way here and had a silly implicit assumption: in its current form, the x-component of the electric field is only affected by the x-component of the current density; from Maxwell's equations, this simplification is not typically the case, so let's go ahead and generalize the Green's function to correctly reflect Maxwell's equations:

$$\langle \mathbf{E}(\mathbf{r},t)\rangle_t = \int d^3\mathbf{r}\ \overleftrightarrow{G}(\mathbf{r},t)\mathbf{j}(\mathbf{r},t) \tag{B.3.4}$$

Now, at this point I tried to be well-motivated and stuck with equations that one can readily find in references. For our particular problem, however, it is more convenient

to define our observable to be the Fourier transform of the electric field. Importantly, since Maxwell's equations are linear differential equations, we can similarly define a Green's function response of the system in frequency space (that will necessarily be a different function than the above Green's function — it's not even the Fourier Transform of the above Green's function). Thus, we take the liberty of writing same expression with $\omega \leftrightarrow \tau$,

$$\langle E(\mathbf{r},t)\rangle_t = \int d^3\mathbf{r}\ \overleftrightarrow{G}(\mathbf{r},\omega)\mathbf{j}(\mathbf{r},\omega) \tag{B.3.5}$$

The last point I want to make is that this Green's function contains all of the information about the geometry of the system. In particular, we can interpret the above equation as "the electric field at a point $\vec{r}$ is the sum of the contributions of the electric field from a current source at all positions $\vec{r}$, weighted by the proper amount $\overleftrightarrow{G}(\vec{r},t)$."

B.4 Putting it All Together

Finally, after setting up the problem correctly, we can use the F-D theorem to write

$$\overleftrightarrow{S}_F = \epsilon_0\hbar\omega^2 \coth\left(\frac{\hbar\omega}{2k_BT}\right) \mathrm{Im}\ \overleftrightarrow{G}(\vec{r},t) \tag{B.4.1}$$

Note I used a different tensor notation than in my statement of the F-D theorem; it can equivalently be indexed by two variables i, j.

B.5 The Electromagnetic Green's Function

Although the F-D theorem let us skip a lot of calculations to find what this spectrum is going to be, one calculation we do need to do is actually figure out the Green's Function for our particular geometry. Note to reader: this will be a bit annoying.

B.6 Green's Function Primer

Let's find the Green's function of the E-M field of a current dipole in a homogenous environment. This is just typically quoted in papers, but this simpler calculation will turn out to be the first step in doing this calculation.

First, we note that it is actually easier to start with the vector potentials rather than the $\mathbf{E}$ and $\mathbf{B}$ fields explicitly.; we assume these are "harmonic", such that $\mathbf{A}(\mathbf{r},t) = \mathbf{A}(\mathbf{r})\exp(i\omega t)$ and $\phi(\mathbf{r},t) = \phi(\mathbf{r})\exp(i\omega t)$. The electric and magnetic fields are written

$$\mathbf{E}(\mathbf{r}) = i\omega\mathbf{A}(\mathbf{r}) - \nabla\phi(\mathbf{r}) \tag{B.6.1}$$

$$\mathbf{B}(\mathbf{r}) = \frac{1}{\mu}\nabla\times\mathbf{A}(\mathbf{r}). \tag{B.6.2}$$

We will use the Lorentz gauge:

$$\nabla\cdot\mathbf{A}(\mathbf{r},t) = \epsilon\mu\frac{d}{dt}\phi(\mathbf{r},t) = i\omega\epsilon\mu\phi(\mathbf{r}). \tag{B.6.3}$$

We want to find the response from a point dipole; this will be derived by the source-field equations with a constant neutral background ($\rho(\mathbf{r}) = 0$). We can write

$$\begin{aligned}
\frac{1}{\mu}\nabla \times \nabla \times \mathbf{A}(\mathbf{r}) &= \frac{d}{dt}\overbrace{D(\mathbf{r})}^{\epsilon E(\mathbf{r})} + j(\mathbf{r}) && \text{(B.6.4)}\\
\frac{1}{\mu}(\nabla(\nabla \cdot \mathbf{A}) - \nabla^2\mathbf{A}) &= \epsilon\frac{d}{dt}(-\nabla\phi(\mathbf{r}) + i\omega\mathbf{A}(\mathbf{r})) + \mathbf{j}(\mathbf{r}) && \text{(B.6.5)}\\
\frac{1}{\mu}((i\omega\mu\epsilon)\nabla\phi - \nabla^2\mathbf{A}) &= i\omega\epsilon\nabla\phi(\mathbf{r}) - \omega^2\mathbf{A}(\mathbf{r}) + \mathbf{j}(\mathbf{r}) && \text{(B.6.6)}\\
(\nabla^2 - \omega^2\epsilon\mu)\mathbf{A}(\mathbf{r}) &= \mathbf{j}(\mathbf{r}) && \text{(B.6.7)}\\
(\nabla^2 - k^2)\mathbf{A}(\mathbf{r}) &= j(\mathbf{r}) && \text{(B.6.8)}
\end{aligned}$$

The last line is the Helmholtz equation. We note that k here is the wave vector as modified by the medium's permeability and susceptibility ($k \neq \omega/c$ but $k = \omega\sqrt{\mu_r\epsilon_r}/c = \omega n/c$). To find the Green's function, we finally get to write

$$\mathbf{j}(\mathbf{r}) = \delta(\mathbf{r} - \mathbf{r}_0)\hat{\mathbf{n}}. \qquad \text{(B.6.9)}$$

i.e., we have an oscillating dipole in the $\hat{n}$ direction.

We find the Green's function in the usual way: first, we think of the delta function as being everywhere 0 except at the origin where weird things happen. Thus, we solve the differential equation for when there is no current at all (i.e., $j(r) = 0$, and this is the solution over the domain where we understand the delta function is 0). Then,

we impose the appropriate discontinuities in $\nabla A(r = 0)$ using a linear combination of these solutions. I had done this in a "Mathematical Methods of Physics" class, but I think most people have seen this in regard to solving for the quantum mechanical bound states of a particle in a delta function potential. The two solutions[3] are

$$G_A(r, r') = \frac{\exp(\pm ik|r - r_0|)}{4\pi|r - r_0|}, \tag{B.6.10}$$

where we usually call the solution with the minus sign the "retarded" Green's function and the one with the plus sign the "advanced" green's function, as one has a time dependence of an excitation radiating outwards and one has the time dependence such that the wave radiates towards the dipole. Of course, that's a statement about the dynamics of the waves, and we've thrown the time-dependence under the rug by initially just imposing $\mathbf{A}(\mathbf{r}, t) = \mathbf{A}(\mathbf{r}) \exp(i\omega t)$, but if you include it becomes clear. Otherwise, I also haven't derived these solutions, but here's a sketch of the derivation: write ∇^2 explicitly in spherical coordinates, work out the simplification algebra, and then solve a simpler diff eq.

Now that we know what the response of the vector potential is due to a point dipole, we can easily get the electric field and magnetic field response out of it; we'll discuss later why we decided to take this round-about approach instead of just writing down the response equations for an electric or magnetic field from Maxwell's equations and

[3] Two solutions since it's a second order diff. eq.

doing similar calculations to those above to find their Green's function. We can write

$$\mathbf{E}(\mathbf{r}) = \mathbf{A}(\mathbf{r}) - \nabla\phi(\mathbf{r}) \tag{B.6.11}$$

$$\mathbf{E}(\mathbf{r}) = i\omega\mu\mathbf{G}_A(\mathbf{r},\mathbf{r_0}) + \mu\nabla(\frac{1}{\epsilon\mu i\omega}\nabla\cdot\mathbf{G}_A(\mathbf{r},\mathbf{r_0})p) \tag{B.6.12}$$

$$= i\omega(\mu\mathbf{G}_A(\mathbf{r},\mathbf{r}') + \nabla(\nabla\mathbf{G}_A(\mathbf{r},\mathbf{r}'))) \tag{B.6.13}$$

where we used the Lorentz gauge and set

$$\phi(r) = \frac{1}{\epsilon\mu i\omega}(\nabla\cdot A(r))) \tag{B.6.14}$$

Note that originally we did not (explicitly) write that $G_A(r,r')$ is a vector; going back, it's easy to see that the vector potential will always point *in the direction* of $j(r)$, and as such we understand $\nabla G_A(r,r') = \nabla G_A(r,r')\vec{n}_j$.

Now we finally got to a result that papers generally just quote:

$$E(r) = i\omega(\overleftrightarrow{I} + \frac{1}{k^2}\nabla\nabla)G_A(r,r'). \tag{B.6.15}$$

This is what people call the "dyadic" Green's function.

In our system, we think of it as a dipole in one material (with ϵ_1, μ_1) some distance (in the z direction) over a material interface (material 2 with ϵ_2, μ_2). Unfortunately, we currently have $E(r)$ written in terms of spherical waves, and that's a little tricky

to deal with in this geometry.

I'll take a short break to just mention that this problem — the propagation of E-M waves from a dipole near a dielectric boundary — was a big deal in the early 20th century, as people were interested in understanding why radio waves seemed to travel so far. Sommerfeld came up with one solution to this problem that showed that there exist long-lived surface waves that propagate between the media, and he concluded that the radio waves propagated far along these surface waves. In the end, he was wrong — radio waves bounce off of the ionosphere, and these seem like they propagate long distances along the earth.

Anyway, back to the problem: in order to deal with scattering of spherical waves off of the dielectric interface, we use a transformation that turns our spherical waves into a superposition of plane waves[4]:

$$\frac{e^{ik\sqrt{x^2+y^2+z^2}}}{\sqrt{x^2+y^2+z^2}} = \frac{i}{2\pi}\int_{-\infty}^{\infty} \frac{e^{i(k_x x + k_y y + ik_z|z|)}}{k_z} dk_x dk_y, \tag{B.6.16}$$

where we enforce that the real and imaginary parts of $k_z = \sqrt{k^2 - k_x^2 - k_y^2} = \sqrt{k^2 - k_{||}^2}$ stay positive[5]. We can then plug this into our expression for the electric field; we find that the result is

[4] Originally derived by Weyl

[5] This is a weird condition that comes from a contour integral when deriving the fourier components (i.e., plane wave components) of a spherical wave)

$$G_E(r,r') = \frac{i}{2\pi}\int_{-\infty}^{\infty} i\omega \frac{1}{k^2 k_z} \begin{pmatrix} k^2-\partial_x^2 & \partial_x\partial_y & \partial_x\partial_z \\ \partial_y\partial_x & k^2-\partial_y^2 & \partial_y\partial_z \\ \partial_z\partial_x & \partial_z\partial_y & k^2-\partial_z^2 \end{pmatrix} e^{i(k_x(x-x_0)+k_y(y-y_0)+ik_z|z-z_0|)} dk_x dk_y \quad (B.6.17)$$

$$= \frac{-\omega^2}{2\pi}\int_{-\infty}^{\infty} \frac{1}{k^2 k_z} \begin{pmatrix} k^2-k_x^2 & -k_x k_y & \mp k_x k_z \\ -k_y k_x & k^2-k_y^2 & \mp k_y k_z \\ \mp k_z k_x & \mp k_z k_y & k^2-k_z^2 \end{pmatrix} e^{i(k_x(x-x_0)+k_y(y-y_0)+ik_z|z-z_0|)} dk_x dk_y \quad (B.6.18)$$

where the $\mp$ signs in the matrix represent the cases when $z > z_0$ and $z < z_0$, respectively.

Here is the general issue now: we want to know what the reflection of these plane waves will be off of the interface; in general, we know how to do this with Fresnel Coefficients and we should be all set and done. The issue arises when you realize that in order to use those coefficients you need to represent a plane wave as either having its polarization in the plane of incidence (p polarization) and perpendicular to the plane (s polarization). The issue, then, is to figure out how we can split up the above plane waves into s and p waves.

I would like to mention that I haven't really found a good source for how this is done, but plenty about how it is possible. Here is my take:

Note that the original operator that acted on the vector potential spherical wave to

turn it into an electric field had the form

$$P \propto (\overleftrightarrow{I} + \frac{1}{k^2}\nabla\nabla) \tag{B.6.19}$$

which we later found to just be

$$P \propto (\overleftrightarrow{I} - \frac{1}{k^2}\mathbf{k}_{\mp}{\mathbf{k}_{\mp}}^{T}) \tag{B.6.20}$$

If you give that expression a second look, you notice that it is in the form of a projection operator. In particular, it projects the spherical wave into a subspace that is *n*ot along the $\mathbf{k}_{\mp}$ direction. We actually expect this of waves emanating from a current source — the waves propagate along the k direction, and the E and B fields should be perpendicular to the direction of propagation.

With that motivation at hand, we then seek to write the above projection operator into two parts; one part projecting onto the s polarization and one part projecting onto the p polarization. To do so, we consider the geometry of the system and find that the vectors can be written:

$$\mathbf{p} = \frac{1}{k\sqrt{k_x^2+k_y^2}}\begin{pmatrix} k_z k_x \\ k_z k_y \\ k_x^2+k_y^2 \end{pmatrix} \tag{B.6.21}$$

$$\mathbf{p}\mathbf{p}^T = \frac{1}{k^2(k_x^2+k_y^2)}\begin{pmatrix} k_x^2 k_z & k_x k_y k_z & \mp k_x(k_x^2+k_y^2) \\ k_x k_y k_z & k_y^2 k_z & \mp k_y(k_x^2+k_y^2) \\ \mp k_x(k_x^2+k_y^2) & \mp k_y(k_x^2+k_y^2) & (k_x^2+k_y^2)^2/k_z \end{pmatrix} \tag{B.6.22}$$

$$\mathbf{s} = \vec{p}\times\vec{k}_{\mp}/|\vec{p}\times\vec{k}_{\mp}| \tag{B.6.23}$$

$$\mathbf{s}\mathbf{s}^T = \frac{1}{k_z(k_x^2+k_y^2)}\begin{pmatrix} k_y^2 & -k_x k_y & 0 \\ -k_x k_y & k_x^2 & 0 \\ 0 & 0 & 0 \end{pmatrix} \tag{B.6.24}$$

Thus we can write

$$\mathbf{G}(r,r_0) = \frac{-\omega^2}{2\pi}\int_{-\infty}^{\infty}\frac{1}{k^2 k_z}\begin{pmatrix} k^2-k_x^2 & -k_x k_y & \mp k_x k_z \\ -k_y k_x & k^2-k_y^2 & \mp k_y k_z \\ \mp k_z k_x & \mp k_z k_y & k^2-k_z^2 \end{pmatrix} e^{i(k_x(x-x_0)+k_y(y-y_0)+ik_z|z-z_0|)}dk_x dk_y \tag{B.6.25}$$

$$= \frac{-\omega^2}{2\pi}\int_{-\infty}^{\infty}(\mathbf{p}\mathbf{p}^T+\mathbf{s}\mathbf{s}^T)e^{i(k_x(x-x_0)+k_y(y-y_0)+ik_z|z-z_0|)}dk_x dk_y \tag{B.6.26}$$

And now we can include the dielectric boundary conditions! :

$$\mathbf{G}_{\mathrm{ref}}(r,r_0) \to \frac{-\omega^2}{2\pi}\int_{-\infty}^{\infty}(r_p(k_x,k_y)\mathbf{p}\mathbf{p}^T + r_s(k_x,k_y)\mathbf{s}\mathbf{s}^T)e^{i(k_x(x-x_0)+k_y(y-y_0)+ik_z|-z-z_0|)}dk_x dk_y \tag{B.6.27}$$

with Fresnel coefficients

$$r^s(k_x,k_y) = \frac{\mu_2\sqrt{k_1^2-(k_x^2+k_y^2)}-\mu_1\sqrt{k_2^2-(k_x^2+k_y^2)}}{\mu_2\sqrt{k_1^2-(k_x^2+k_y^2)}+\mu_1\sqrt{k_2^2-(k_x^2+k_y^2)}} \tag{B.6.28}$$

$$r^p(k_x,k_y) = \frac{\epsilon_2\sqrt{k_1^2-(k_x^2+k_y^2)}-\epsilon_1\sqrt{k_2^2-(k_x^2+k_y^2)}}{\epsilon_2\sqrt{k_1^2-(k_x^2+k_y^2)}+\epsilon_1\sqrt{k_2^2-(k_x^2+k_y^2)}} \tag{B.6.29}$$

where $k_1 = \omega\sqrt{\epsilon_1\mu_1}/c = \omega n_1/c$ and similarly for k_2. Note that upon introducing the Fresnel coefficients, we also changed the direction the wave was propagating by changing $z \to -z$. Whew. Now we just need to (a) simplify the integral and (b) find the imaginary part. To simplify the integral, we change variables to cylindrical coordinates, $(k_x,k_y,k_z) \to (k_\rho\cos(\phi), k_\rho\sin(\phi), k_z)$ and write

$$G(r,r_0) \to \frac{-\omega^2}{2\pi}\int_0^{\infty}\int_0^{2\pi}(r_p(k_\rho)\vec{p}\vec{p}^T + r_s(k_\rho)\vec{s}\vec{s}^T)e^{i(k_\rho\cos(\phi)(x-x_0)+k_\rho\sin(\phi)(y-y_0)+ik_z(z+z_0))}k_\rho d\phi dk_\rho \tag{B.6.30}$$

where we noted that the reflection coefficients will only depend on k_ρ and with

$$\vec{p}\vec{p}^{T} = \frac{1}{k_1^2}\begin{pmatrix} k_z\cos^2(\phi) & k_z\sin(\phi)\cos(\phi) & \mp k_\rho\cos(\phi) \\ k_z\cos(\phi)\sin(\phi) & k_z\sin^2(\phi) & \mp k_\rho\sin(\phi) \\ \mp k_\rho\cos(\phi) & \mp k_\rho\sin(\phi) & k_\rho^2/k_z \end{pmatrix} \tag{B.6.31}$$

$$\vec{s}\vec{s}^{T} = \frac{1}{k_z}\begin{pmatrix} \sin^2(\phi) & -\sin(\phi)\cos(\phi) & 0 \\ -\sin(\phi)\cos(\phi) & \cos^2(\phi) & 0 \\ 0 & 0 & 0 \end{pmatrix} \tag{B.6.32}$$

Some of the integrals to be evaluated above are 0, but many of them are given by Bessel Functions. In our case, we care about the Green's Function response at the point of the dipole; plugging in $\mathbf{r} = \mathbf{r}_0$, the tensor becomes symmetric:

$$G(r_0, r_0) \rightarrow \frac{-\omega^2}{2\pi} \int_0^\infty r^p(k_\rho) \frac{1}{k_1^2} \begin{pmatrix} k_z\pi & 0 & 0 \\ 0 & k_z\pi & 0 \\ 0 & 0 & 2\pi k_\rho^2/k_z \end{pmatrix} e^{2ik_z z_0} \tag{B.6.33}$$

$$+r^s(k_\rho) \frac{1}{k_z} \begin{pmatrix} \pi & 0 & 0 \\ 0 & \pi & 0 \\ 0 & 0 & 0 \end{pmatrix} e^{2ik_z z_0}\, dk_\rho \tag{B.6.34}$$

$$= \frac{-\omega^2}{2} \int_0^\infty \frac{1}{k_z k_1^2} \begin{pmatrix} r^p k_z^2 + r^s k_1^2 & 0 & 0 \\ 0 & r^p k_z^2 + r^s k_1^2 & 0 \\ 0 & 0 & 2r^p k_1^2 \end{pmatrix} e^{2ik_z z_0}\, dk_\rho \tag{B.6.35}$$

$$= -\frac{c^2}{2} \int_0^\infty \frac{1}{\sqrt{1-k_\rho^2}} \begin{pmatrix} r^p k_z^2 + r^s k_1^2 & 0 & 0 \\ 0 & r^p k_z^2 + r^s k_1^2 & 0 \\ 0 & 0 & 2r^p k_1^2 \end{pmatrix} e^{2ik_z z_0} dk_\rho \tag{B.6.36}$$

$$= g_{||}(kz) \begin{pmatrix} 1 & 0 & 0 \\ 0 & 1 & 0 \\ 0 & 0 & 0 \end{pmatrix} + g_\perp(kz) \begin{pmatrix} 0 & 0 & 0 \\ 0 & 0 & 0 \\ 0 & 0 & 1 \end{pmatrix} \tag{B.6.37}$$

In the last line, we use notation from Henkel et. al. Taking the imaginary part of the above expression, we find that I have apparently made a mistake in some of the constants above. We need to compare the above with the function given in Henkel et.

al.,

$$g_{||}(kz) = \frac{3}{2}\,\mathrm{Re}\int_0^\infty du \frac{u}{v(u)}(r^s(u) + (u^2-1)r^p(u))e^{2ikzv(u)} \quad \text{(B.6.38)}$$

$$g_{\perp}(kz) = \frac{3}{4}\,\mathrm{Re}\int_0^\infty du \frac{u^3}{v(u)}r^p(u)e^{2ikzv(u)} \quad \text{(B.6.39)}$$

B.7 Electric Dipole to Magnetic dipole

We can map the problem of finding the appropriate Green's function for an electric dipole to that of a magnetic dipole by simply making the substitutions

$$\mathbf{E} \leftrightarrow \mathbf{B} \quad \text{(B.7.1)}$$

$$\epsilon \leftrightarrow \mu \quad \text{(B.7.2)}$$

$$\mu \leftrightarrow \mathbf{m} \quad \text{(B.7.3)}$$

where the last identification is between the magnetic moment $\mathbf{m}$ and the electric dipole moment μ. This substitution is kosher because Maxwell's equations become symmetric if we set $\rho_e = 0$, i.e., there are no free charges.

B.8 The Loss Rate

We can write our Green's function as the sum of two contributions; that of the metal slab and that of the (magnetic) dipole a distance z away from it. The blackbody radiation from the slab simply follows Plank's law, and is a diagonal matrix with entries

$$\left(S_E^{bb}\right)_{i,j} = \frac{\delta_{i,j}\omega^3}{6\pi\epsilon_0 c^3}\coth(\frac{\hbar\omega}{2k_BT}) \tag{B.8.1}$$

Note that it does not depend on the position r beneath the slab.

The calculation of the contribution from the dipole is done by decomposing the dipole's emission into plane waves and calculating the plane wave's scattering off of the metal. Using the coordinate system where z is perpendicular to the metal, the spectrum tensor contribution from the radiating dipole field is also diagonal,

$$\left(S_E^{\text{dipole}}\right)_{i,j} = \delta_{z,i}\delta_{z,j}\overbrace{\frac{3}{4}\,\mathrm{Re}\int_0^\infty \frac{u\,du}{v(u)}e^{2ikzv(u)}(r_s(u)+(u^2-1)r_p(u))}^{g_\perp(kz)} \tag{B.8.2}$$

$$+(\delta_{x,i}\delta_{x,j}+\delta_{y,i}\delta_{y,j})\overbrace{\frac{3}{2}\,\mathrm{Re}\int_0^\infty \frac{u^3\,du}{v(u)}e^{2ikzv(u)}r_p(u)}^{g_{||}(kz)} \tag{B.8.3}$$

with $v(u)$ being the function

$$v(u) = \sqrt{1-u^2} \tag{B.8.4}$$

and r denoting the Fresnel coefficients

$$r_p(u) = \frac{\epsilon v - \sqrt{\epsilon - u^2}}{\epsilon v + \sqrt{\epsilon - u^2}} \tag{B.8.5}$$

$$r_s(u) = \frac{v - \sqrt{\epsilon - u^2}}{v + \sqrt{\epsilon - u^2}} \tag{B.8.6}$$

Note that there is a suppressed dependence on ω in epsilon; in every material, there is a different dielectric response depending on the frequency of the radiation. For us, what we really care about is ϵ in the microwave frequency range. These frequencies are low enough that they are still dominated by the divergence of the DC dielectric constant in metals, and can be given as

$$\epsilon_r(\omega) \approx 1 + \frac{i}{\epsilon_0 \rho \omega} \tag{B.8.7}$$

where ρ is the DC resistivity.

These green's functions are unwieldy, and so Henkel et. al. estimate them; for our purposes, we are interested in the regime $z << \delta << \lambda$, in which we can estimate

$$g_\perp(kz) \approx 2g_{||}(kz) \approx \frac{3}{16(kz)^3} \operatorname{Im} \frac{\epsilon - 1}{\epsilon + 1} \tag{B.8.8}$$

All that was listed here is for electric fields; the same calculations find that the green's functions for the magnetic field is actually almost identical, with the substi-

tution $r_p(u) \leftrightarrow r_s(u)$.

B.9 Master Equation

We model the relaxation as a coupling to a Markovian bath with dynamics governed by the usual Master equation in Lindblad form; we consider both stimulated emission processes as well as excitation processes:

$$\dot{\rho} = -\frac{g^2}{\hbar^2} \sum_{i,j} \frac{S_F^{ij}(\vec{r},\omega)}{2} \left(s_i^{(-)} s_j^{(+)} \rho + \rho s_i^{(-)} s_j^{(+)} - 2 s_j^{(+)} \rho s_i^{(-)} \right) \tag{B.9.1}$$

Note that we write this master equation in the Heisenberg picture, hence the free evolution term is missing above. Our relaxation rate will very much depend on what the magnitude of the magnetic field noise is at our spin spitting frequency:

$$S_F^{i,j} = \int_{\infty}^{\infty} d\tau \langle F_i(\vec{r}_1, t+\tau) F_j(\vec{r}_2, t) \rangle e^{i\omega\tau} \tag{B.9.2}$$

where the F in the subscript of S signifies the field we are interested in.

B.10 Spin Relaxation Rate

Our first consideration when considering what the spin relaxation rate is simply understanding the coupling in our system. For us, the magnetic fields will couple with the magnetic dipole moment of the spin, and so we can write

$$V(r,t) = g\mu S \cdot B(r,t) \tag{B.10.1}$$

where the external magnetic fields are the fluctuating fields. In the context of Fermi's Golden Rule, we are then interested in matrix elements of the form

$$|\langle f|V(r,t)|i\rangle|^2 = (g\mu)^2\langle f|S\cdot B|i\rangle \tag{B.10.2}$$

$$= (g\mu)^2 \textstyle\sum_\alpha \langle f|S_\alpha|i\rangle B_\alpha \tag{B.10.3}$$

The dependence on B here will be replaced with the spectrum of the magnetic field at that point.

There are a couple of technicalities that come into play here, in regard to our specific system of interest: NV centers. In particular, an NV center is an effective spin-1 system, so that we must consider the rates from an initial polarized state (all in $|0\rangle$) to both the other options ($|1\rangle$ and $|-1\rangle$). Also, the NV's quantization axis is not parallel to the any of the axes defined in our problem.

For the latter, if we assume (wlog) the spin's quantization axis is in the x-z plane of our working coordinate system, we find

$$\langle m_f|S_x|m_i\rangle = \frac{1}{2}\cos(\theta)\left(\langle m_f|S'_+|m_i\rangle + \langle m_f|S'_-|m_i\rangle\right) + \sin(\theta)\langle m_f|S'_z|m_i\rangle \quad \text{(B.10.4)}$$

$$\langle m_f|S_y|m_i\rangle = \frac{i}{2}\left(\langle m_f|S'_-|m_i\rangle - \langle m_f|S'_+|m_i\rangle\right) \quad \text{(B.10.5)}$$

$$\langle m_f|S_z|m_i\rangle = -\frac{1}{2}\sin(\theta)\left(\langle m_f|S'_+|m_i\rangle + \langle m_f|S'_-|m_i\rangle\right) + \cos(\theta)\langle m_f|S'_z|m_i\rangle \quad \text{(B.10.6)}$$

with primed operators denoting the spin operators with the axes defined with respect to the quantization axis, and unprimed operators denoting the spin operators in our coordinate system. Here θ denotes the angle the quantization axis makes with our z-axis (perpendicular to the metal). In our diamond, NV centers have 4 different orientations; there are only two angles the NV can make with the z axis, however: $\cos^{-1}(1/3)$ and $\pi - \cos^{-1}(1/3)$.

B.11 The loss rate

Our loss rate is given by

$$
\begin{aligned}
\Gamma_{i\to f} &= \sum_{\alpha,\beta} \frac{\langle i|\mu_\alpha|f\rangle\langle f|\mu_\beta|i\rangle}{\hbar^2} S_B^{\alpha,\beta}(r;-\omega_{f,i}) && \text{(B.11.1)}\\
&= \frac{(\mu_B g)^2}{\hbar^2} \sum_{\alpha,\beta} \langle i|\mu_\alpha|f\rangle\langle f|\mu_\beta|i\rangle S_B^{bb}(\omega_L) h_{\alpha,\beta}(kz) && \text{(B.11.2)}\\
&= \frac{(\mu_B g)^2}{\hbar^2} \frac{S_E^{bb}(\omega_L)}{c^2} \sum_{\alpha} |\langle i|S_\alpha|f\rangle|^2 h_{\alpha,\alpha}(kz) && \text{(B.11.3)}\\
&= \frac{\mu_B^2 g^2 \hbar \omega_L^3}{3\pi\epsilon_0 c^5 \hbar^2 (1-e^{-\hbar\omega_L/k_B T})} \sum_{\alpha} h_{\alpha\alpha}(kz) |\langle f|S_\alpha|i\rangle|^2 && \text{(B.11.4)}\\
&\approx \frac{\mu_B^2 g^2 \omega_L^3}{3\pi\epsilon_0 c^5 \hbar (1-(1-\hbar\omega/k_B T))} \sum_{\alpha} h_{\alpha\alpha}(kz) |\langle f|S_\alpha|i\rangle|^2 && \text{(B.11.5)}\\
&\approx \frac{\mu_B^2 g^2 \omega_L^2 k_B T}{3\pi\epsilon_0 c^5 \hbar^2} \left(\frac{3}{16 k^3 \delta^2 z}\right) \sum s_{\alpha,\alpha} |\langle f|S_\alpha|i\rangle|^2 && \text{(B.11.6)}\\
&= \frac{\mu_B^2 g^2 \omega_L^2 k_B T}{3\pi\epsilon_0 c^5 \hbar^2} \left(\frac{3}{16 kz (2\epsilon_0 \rho \omega_L)}\right) \sum s_{\alpha,\alpha} |\langle f|S_\alpha|i\rangle|^2 && \text{(B.11.7)}\\
&= \frac{\mu_B^2 g^2 \omega_L k_B T}{32\pi\epsilon_0^2 \rho c^5 \hbar^2 kz} \sum s_{\alpha,\alpha} |\langle f|S_\alpha|i\rangle|^2 && \text{(B.11.8)}\\
&= \frac{\mu_B^2 g^2 \mu_0^2 k_B T}{32\pi\rho\hbar^2 z} \sum s_{\alpha,\alpha} |\langle f|S_\alpha|i\rangle|^2 && \text{(B.11.9)}
\end{aligned}
$$

Now, we consider specifically the transition from $m_S = 0$ to $m_S = 1$,

$$
\begin{aligned}
|\langle 0|S_x|1\rangle|^2 &= |\frac{1}{2}\cos(\theta)\left(\langle 1|S'_+|0\rangle + \langle 1|S'_-|0\rangle\right) + \sin(\theta)\langle 1|S'_z|0\rangle|^2 && \text{(B.11.10)}\\
&= |\frac{1}{2}\cos(\theta)(\sqrt{2})|^2 && \text{(B.11.11)}\\
&= \frac{1}{2}\cos^2(\theta) && \text{(B.11.12)}\\
|\langle 0|S_y|1\rangle|^2 &= |\frac{i}{2}(\langle 0|S'_-|1\rangle - \langle 0|S'_+|1\rangle)|^2 && \text{(B.11.13)}\\
&= \frac{1}{4}|\sqrt{2}|^2 && \text{(B.11.14)}\\
&= \frac{1}{2} && \text{(B.11.15)}\\
|\langle 0|S_z|1\rangle|^2 &= |-\frac{1}{2}\sin(\theta)\left(\langle 1|S'_+|0\rangle + \langle 1|S'_-|0\rangle\right) + \cos(\theta)\langle 1|S'_z|0\rangle|^2 && \text{(B.11.16)}\\
&= \frac{1}{2}\sin^2(\theta) && \text{(B.11.17)}
\end{aligned}
$$

where we made good use of the relation

$$
S_\pm|s, m_s\rangle = \sqrt{s(s+1) - m(m\pm 1)}|s, m_s \pm 1\rangle. \qquad \text{(B.11.18)}
$$

Plugging this in, we get

$$\Gamma_{i\to f} = \frac{\mu_B^2 g^2 \mu_0^2 k_B T}{32\pi\rho\hbar^2 z} \sum s_{\alpha,\alpha} |\langle f|S_\alpha|i\rangle|^2 \tag{B.11.19}$$

$$= \frac{\mu_B^2 g^2 \mu_0^2 k_B T}{32\pi\rho\hbar^2 z} \left(\frac{1}{2}\cos^2(\theta) + \frac{1}{2} + 2\frac{1}{2}\sin^2(\theta)\right) \tag{B.11.20}$$

$$= \frac{\mu_B^2 g^2 \mu_0^2 k_B T}{32\pi\rho\hbar^2 z} \left(1 + \frac{1}{2}\sin^2(\theta)\right) \tag{B.11.21}$$

We note that the angle with the vertical for our NVs is given by $\theta = \frac{1}{2}\cos^{-1}(1/3)$, so that

$$\sin^2(\theta) = \sin^2(\frac{1}{2}\cos^{-1}(1/3)) \tag{B.11.22}$$

$$= \frac{1 - \cos(\cos^{-1}(1/3))}{2} \tag{B.11.23}$$

$$= \frac{1}{3}. \tag{B.11.24}$$

Combining our results,

$$\Gamma_{i\to f} = \frac{\mu_B^2 g^2 \mu_0^2 k_B T}{32\pi\rho\hbar^2 z} \left(1 + \frac{1}{2}\sin^2(\theta)\right) \tag{B.11.25}$$

$$= \frac{7\mu_B^2 g^2 \mu_0^2 k_B T}{192\pi\rho\hbar^2 z}. \tag{B.11.26}$$

For completeness, we can do the last steps if we had started for their expressions, and

gotten

$$\Gamma_{i\to f} = \frac{\mu_B^2 g_S^2 \omega_L^2 k_B T}{3\pi\epsilon_0\hbar^2 c^5}\sum_\alpha (h_{\alpha,\alpha}+1)|\langle f|S_\alpha|i\rangle|^2 \tag{B.11.27}$$

$$= \frac{\mu_B^2 g_S^2 \omega_L^2 k_B T}{3\pi\epsilon_0\hbar^2 c^5}\left((\frac{3}{16kz(2\epsilon_0\rho\omega_L)}+1)(\frac{1}{2}\cos^2(\theta)+\frac{1}{2})+(2\frac{3}{16kz(2\epsilon_0\rho\omega_L)}+1)\frac{1}{2}\sin^2(\theta)\right) \tag{B.11.28}$$

$$= \frac{\mu_B^2 g_S^2 \omega_L^2 k_B T}{3\pi\epsilon_0\hbar^2 c^5}\left((\frac{3}{16kz(2\epsilon_0\rho\omega_L)}+1)(\frac{5}{6})+(2\frac{3}{16kz(2\epsilon_0\rho\omega_L)}+1)\frac{1}{6}\right) \tag{B.11.29}$$

$$= \frac{\mu_B^2 g_S^2 \omega_L^2 k_B T}{3\pi\epsilon_0\hbar^2 c^5}\left(\frac{7}{64kz\epsilon_0\rho\omega_L}+1\right) \tag{B.11.30}$$

$$= \frac{7\mu_B^2 g^2 \mu_0^2 k_B T}{192\pi\rho\hbar^2 z}+\frac{\mu_B^2 g_S^2 \omega_L^2 k_B T}{3\pi\epsilon_0\hbar^2 c^5} \tag{B.11.31}$$

Finally, we note that the calculations done in Henkel et. al. are the rate given that the particle will leave the trap once it has slipped out. As such, we can write their rate equations (in the interaction picture) such that

$$\partial_t\rho_{00} = -\gamma\rho_{00} \tag{B.11.32}$$

which of course has solutions

$$\rho_{00}(t) = \rho_{00}(t=0)\exp(-\gamma t) \tag{B.11.33}$$

Instead, we have in our system

$$\partial_t \rho_{00} = -\gamma_0 \rho_{00} + \gamma_1(\rho_{11} + \rho_{-1-1}) \tag{B.11.34}$$

$$\partial_t \rho_{\pm 1 \pm 1} = -\gamma_1 \rho_{\pm 1 \pm 1} + \frac{\gamma_0}{2}\rho_{00} \tag{B.11.35}$$

Note that the above rates are such that probability is preserved over time, $\partial_t \sum_i \rho_{ii} = 0$. First we note that we expect our interactions to be such that in equilibrium $\rho_{ii} = 1/3$; this imposes $\gamma_1 = \gamma_0/2$. Then,

$$\partial_t \begin{pmatrix} \rho_{00} \\ \rho_{-1-1} \\ \rho_{11} \end{pmatrix} = \begin{pmatrix} -\gamma_0 & \gamma_0/2 & \gamma_0/2 \\ \gamma_0/2 & -\gamma_0/2 & 0 \\ \gamma_0/2 & 0 & -\gamma_0/2 \end{pmatrix} \begin{pmatrix} \rho_{00} \\ \rho_{-1-1} \\ \rho_{11} \end{pmatrix} \tag{B.11.36}$$

Looking for exponentially decaying solutions, we consider the eigenvalues of the above matrix. We find there is only one decaying solution that involves population in ρ_{00}, and it decays at a timescale of $3\gamma_0/2$. As such, because of the presence of these two other states that can contribute amplitude to the ρ_{00} state, we decay faster by a factor of (3/2). In particular, the solution with $\rho_{00}(t = 0) = 1$ has the solution given in the following:

$$\vec{\rho}(t) = A\exp(-3\gamma_0 t/2)\begin{pmatrix}-2\\1\\1\end{pmatrix} + B\exp(-\gamma_0/2)\begin{pmatrix}0\\-1\\1\end{pmatrix} + C\begin{pmatrix}1\\1\\1\end{pmatrix} \quad \text{(B.11.37)}$$

(B.11.38)

We look for constants such that

$$-2A + C = 1 \quad \text{(B.11.39)}$$

$$A - B + C = 0 \quad \text{(B.11.40)}$$

$$A + B + C = 0, \quad \text{(B.11.41)}$$

for which we have $A = -(1/3), B = 0, C = 1/3$, and

$$\rho_{00}(t) = \frac{2}{3}\exp(-3\gamma_0 t/2) + \frac{1}{3} \quad \text{(B.11.42)}$$

Thus, we get the result that the decay rate will be (3/2) the rate it would be if there was no probability amplitude "flow" from the two other states back to 0. Thus

we get

$$\boxed{\Gamma_{i\to f} \to \frac{7\mu_B^2 g^2 \mu_0^2 k_B T}{128\pi\rho\hbar^2 z} + \left(\frac{\mu_B^2 g_S^2 \omega_L^2 k_B T}{2\pi\epsilon_0 \hbar^2 c^5}\right)}. \tag{B.11.43}$$

C

Appendix C: In-Depth Theory of Spin-Spin Interactions via Mechanical Resonators

C.1 Theory

There are two main important portions of the theory: that of the NV-NV entanglement scheme, and that of the resonator cooling.

C.1.1 NV-NV Entanglement, No Noise

On the most basic level, two NV's would interact with a resonator with the following Hamiltonian describing the dynamics:

$$H = \omega_{\mathrm{NV}} \sum_i S_z^i + \omega_{\mathrm{res}} a^\dagger a + g\mu_B x_0 \frac{\partial B}{\partial r} \sum_i S^z (a^\dagger + a) \tag{C.1.1}$$

That is, in addition to the single NV and mechanical resonator terms, the mechanical resonator displaces its equilibrium position based on the state of the NV center. Put another way, the NV center feels a different energy splitting depending on the state of the resonator. It should be clear already that there are few choices in improving the interaction strength, at least between an NV and resonator: having large field gradient and/or large zero-point motion.

Of course, other NV centers will also "feel" this change in the resonator equilibrium point, but the interaction can be made clearer. Unless otherwise specified, we will denote focus on there being just two NV centers in the above Hamiltonian, and we

work in a rotating frame such that

$$H = \Delta(S_1^z + S_2^z) + g\left[a(S_1^+ + S_2^+) + a^\dagger(S_1^- + S_2^-)\right]. \tag{C.1.2}$$

Let

$$A = \frac{g}{\Delta}\left(aS^+ - a^\dagger S^-\right). \tag{C.1.3}$$

Then, we can perform a unitary operation $e^A H e^{-A} = H_{\text{eff}}$ to find

$$H_{\text{eff}} = \left(\Delta + \frac{g^2}{\Delta} + 2\frac{g^2}{\Delta}a^\dagger a\right)(S_1^z + S_2^z) + \frac{g^2}{\Delta}(S_1^+ S_2^- + S_1^- S_2^+). \tag{C.1.4}$$

Note we now have a clear picture of the flip-flop between NV centers in the time evolution of this Hamiltonian (second term above).

C.1.2 NV-NV Entanglement, With Unwanted External Interactions

While the physics above indicates that two NV's interacting with a single-mode resonator should become entangled in time, a big issue within the majority of currently-studied quantum systems is their interactions with unwanted degrees of freedom in the environment of the system, resulting in unwanted dynamics and (usually) a loss of entanglement between quantum systems.

One of the simplest ways of including such effects is via a master equation; if we identify the two main main sources of interaction that of the resonator with its environment (with strength κ) and the NV centers and their environment (with strength γ), we can write

$$\dot{\rho} = -i[H, \rho] + \kappa(\bar{n}_{\text{th}} + 1)\mathcal{D}[a]\rho + \kappa\bar{n}_{\text{th}}\mathcal{D}[a^\dagger]\rho + 2\gamma(\mathcal{D}[S_1^z]\rho + \mathcal{D}[S_2^z]\rho), \tag{C.1.5}$$

with $\mathcal{D}[A]\rho = A\rho A^\dagger - \frac{1}{2}\{A^\dagger A, \rho\}$, and each use of $\mathcal{D}$ indicating another form of dissipation. The first dissipation term indicates the loss of energy from the resonator to the environment, and the second two indicate the dephasing of the NV centers.

On can show that two qubit gate errors (in particular, a SWAP gate between NV centers) will result in an error

$$\text{error } \approx \alpha\frac{\gamma\Delta}{g^2} + C\frac{\kappa_{\text{th}}}{\Delta}, \tag{C.1.6}$$

for some constant C and κ_{th} the thermally enhanced resonator dissipation rate $\kappa_{\text{th}} = \kappa(2\bar{n}_{\text{th}}+1)$. After optimizing for the best possible detuning Δ, one finds that the error goes as

$$\text{error } \approx \frac{\kappa_{\text{th}}\gamma}{g^2} \tag{C.1.7}$$

This is the inverse of the **cooperativity**, perhaps the most important parameter we attempt to optimize in our experiment. Notably, our gate fidelity will increase with large enough cooperativity. Intuitively, the cooperativity is higher with high coupling, but lower depending on the strength of dephasing and resonator dissipation.

References

[AB] AB, L. C. S. S.

[2] Ansmann, M. (2009). *Benchmarking the Superconducting Josephson Phase Qubit: The Violation of Bell's Inequality*. PhD thesis, University of California Santa Barbara.

[3] Anton, S. M., Birenbaum, J. S., O'Kelley, S. R., Bolkhovsky, V., Braje, D. A., Fitch, G., Neeley, M., Hilton, G. C., Cho, H.-M., Irwin, K. D., Wellstood, F. C., Oliver, W. D., Shnirman, A., & Clarke, J. (2013). Magnetic flux noise in dc squids: Temperature and geometry dependence. *Physical Review Letters*, 110, 147002.

[4] Ashcroft, N. W. & Mermin, N. D. (1976). *Solid State Physics*. Holt, Rinehart and Winston.

[5] Aspelmeyer, M., Kippenberg, T., & Marquardt, F. (2014). Cavity optomechanics. *Reviews of Modern Physics*.

[6] Balasubramanian, G., Chan, I. Y., Kolesov, R., Al-Hmoud, M., Tisler, J., Shin, C., Kim, C., Wojcik, A., Hemmer, P. R., Krueger, A., Hanke, T., Leitenstorfer, A., Bratschitsch, R., Jelezko, F., & Wrachtrup, J. (2008). Nanoscale imaging magnetometry with diamond spins under ambient conditions. *Nature*, 455(7213), 648–651.

[7] Bar-Gill, N., Pham, L., Jarmola, A., Budker, D., & Walsworth, R. (2013). Solid-state electronic spin coherence time approaching one second. *Nature Communications*, 4(1743).

[8] Baski, A. A. & Fuchs, H. (1994). Epitaxial-growth of silver on mica as studied by afm and stm. *Surface Science*, 313, 275–288.

[9] Beenakker, C. & van Houten, H. (1991). Quantum transport in semiconductor nanostructures. *Solid state physics*, 44(1), 228.

[10] Binder, Stark, J. M., Tomek, A., Scheuer, N., Frank, J., Jahnke, F., Müller, K. D., Schmitt, C., Metsch, S., Unden, M. H., Gehring, T., Huck, T., Andersen, A., Rogers, U. L., Jelezko, L. J., & Fedor (2017). Qudi: A modular python suite for experiment control and data processing. *SoftwareX*.

[11] Bleszynski-Jayich, A. C., Shanks, W. E., Peaudecerf, B., Ginossar, E., von Oppen, F., Glazman, L., & Harris, J. G. E. (2009). Persistent currents in normal metal rings. *Science*, 326(5950), 272–275.

[12] Bluhm, H., Koshnick, N. C., Bert, J. A., Huber, M. E., & Moler, K. A. (2009). Persistent currents in normal metal rings. *Physical Review Letters*, 102, 136802.

[13] Brownnutt, M., Kumph, M., Rabl, P., & Blatt, R. (2014). Ion-trap measurements of electric-field noise near surfaces.

[14] C. Moon, F. (1994). *Superconducting Levitation: Applications to Bearing and Magnetic Transportation*. Wiley-VCH.

[15] Chan, J., Alegre, T. M., Safavi, A., Hill, J., Krause, A., Groblacher, S., Aspelmeyer, M., & Painter, O. (2011). Laser cooling of a nanomechanical oscillator into its quantum ground state. *Nature*.

[16] Childress, L., Gurudev Dutt, M., Taylor, J., Zibrov, A., Jelezko, F., J, W., Hemmer, P., & Lukin, M. (2006). Coherent dynamics of coupled electron and nuclear spin qubits in diamond. *Science*, 314, 281.

[17] Childress, L. I. (2007). *Coherent manipulation of single quantum systemsin the solid state*. PhD thesis, Harvard University.

[18] Datta, S. (1997). *Electronic transport in mesoscopic systems*. Cambridge university press.

[19] Falk, A. L., Koppens, F. H. L., Yu, C. L., Kang, K., de Leon Snapp, N., Akimov, A. V., Jo, M.-H., Lukin, M. D., & Park, H. (2009). Near-field electrical

detection of optical plasmons and single-plasmon sources. *Nature Physics*, 5(7), 475–479.

[20] Faoro, L. & Ioffe, L. B. (2008). Microscopic origin of low-frequency flux noise in josephson circuits. *Physical Review Letters*, 100, 227005.

[21] Ford, G. W. & Weber, W. (1984). Electromagnetic interactions of molecules with metal surfaces. *Physics Reports*, 113(4), 195–287.

[22] Harber, D., McGuirk, J., Obrecht, J., & Cornell, E. (2003). Thermally induced losses in ultra-cold atoms magnetically trapped near room-temperature surfaces. *Journal of Low Temperature Physics*, 133(3-4), 229–238.

[23] Henkel, C., Pötting, S., & Wilkens, M. (1999). Loss and heating of particles in small and noisy traps. *Applied Physics B*, 69(5-6), 379–387.

[24] Higginbotham, A., Burns, P., Urmey, M., Peterson, R., N.S. Kampel, B. B., Smith, G., Lehnert, K., & Regal, C. (2018). Harnessing electro-optic correlations in an efficient mechanical converter. *Nature Physics*, 14, 1038–1042.

[25] Jarmola, A., Acosta, V. M., Jensen, K., Chemerisov, S., & Budker, D. (2012). Temperature- and magnetic-field-dependent longitudinal spin relaxation in nitrogen-vacancy ensembles in diamond. *Physical Review Letters*, 108, 197601.

[26] Jones, M. P. A., Vale, C. J., Sahagun, D., Hall, B. V., & Hinds, E. A. (2003). Spin coupling between cold atoms and the thermal fluctuations of a metal surface. *Physical Review Letters*, 91, 080401.

[27] Kimball, D. F. J., Sushkov, A. O., & Budker, D. (2016). Precessing ferromagnetic needle magnetometer. *Physical Review Letters*, 116(19).

[28] Kordyuk, A. A. (1998). Magnetic levitation for hard superconductors. *Journal of Applied Physics*, 83(1), 610–612.

[29] Langsjoen, L. S., Poudel, A., Vavilov, M. G., & Joynt, R. (2012). Qubit relaxation from evanescent-wave johnson noise. *Physical Review A*, 86, 010301.

[30] Langsjoen, L. S., Poudel, A., Vavilov, M. G., & Joynt, R. (2014). Electromagnetic fluctuations near thin metallic films. *Physical Review B*, 89, 115401.

[31] Lin, Y., Teper, I., Chin, C., & Vuletic, V. (2004). Impact of the casimir-polder potential and johnson noise on bose-einstein condensate stability near surfaces. *Physical Review Letters*, 92, 050404.

[32] Longenecker, J. G. (2013). *HIGH-GRADIENT NANOMAGNET-ON-CANTILEVER FABRICATION FOR SCANNED PROBE DETECTION OF MAGNETIC RESONANCE*. PhD thesis, Cornell University.

[33] Longenecker, J. G., Mamin, H. J., Senko, A. W., Chen, L., Rettner, C. T., Rugar, D., & Marohn, J. A. (2012). High-gradient nanomagnets on cantilevers for sensitive detection of nuclear magnetic resonance. *ACS Nano*, 6(11), 9637–9645.

[34] Lundstrom, M. (2003). Moore's law forever? *Science*, 299(5604), 210–211.

[35] Maher, P., Wang, L., Gao, Y., Forsythe, C., Taniguchi, T., Watanabe, K., Abanin, D., Papić, Z., Cadden-Zimansky, P., Hone, J., Kim, P., & Dean, C. R. (2014). Tunable fractional quantum hall phases in bilayer graphene. *Science*, 345(6192), 61–64.

[36] Maze, J., Stanwix, P., Hodges, J., Hong, S., Taylor, J., Cappellaro, P., Jiang, L., Dutt, M., Togan, E., Zibrov, A., & Lukin, M. (2008). Nanoscale magnetic sensing with an individual electronic spin in diamond. *Nature*, 455(7213), 644–647.

[37] McCabe, G., Ren, H., Luo, J., Cohen, J., Zhou, H., Sipahigil, A., Mirhosseini, M., & Painter, O. (2019). Phononic bandgap nano-acoustic cavity with ultra-long phonon lifetime. *ArXiv e-prints*, arXiv:1901.04129.

[38] Neumann, P., Beck, J., Steiner, M., Rempp, F., Fedder, H., Hemmer, P. R., Wrachtrup, J., & Jelezko, F. (2010). Single-shot readout of a single nuclear spin. *Science*.

[39] Novotny, L. & Hecht, B. (2012). *Principles of nano-optics*. Cambridge university press.

[40] Park, J. H., Ambwani, P., Manno, M., Lindquist, N. C., Nagpal, P., Oh, S. H., Leighton, C., & Norris, D. (2012). Single-crystalline silver films for plasmonics. *Advanced Materials*, 24, 3988–3992.

[41] Pelliccione, M., Myers, B. A., Pascal, L., Das, A., & Bleszynski Jayich, A. C. (2014). Two-dimensional nanoscale imaging of gadolinium spins via scanning probe relaxometry with a single spin in diamond.

[42] Pezzagna, S., Naydenov, B., Jelezko, F., Wrachtrup, J., & Meijer, J. (2010). Creation efficiency of nitrogen-vacancy centres in diamond. *New Journal of Physics*, 12(6), 065017.

[43] Pikovski, I., Zych, M., Costa, F., & Brukner, C. (2015). Universal decoherence due to gravitational time dilation. *Nature Physics*, (pp. 668–672).

[44] Pino, H., Prat-Camps, J., Sinha, K., Venkatesh, B. P., & Romero-Isart, O. (2018). On-chip quantum interference of a superconducting microsphere. *Quantum Science and Technology*, 3(2).

[45] Rabl, P., Kolkowitz, S. J., Koppens, F. H. L., Harris, J. G. E., Zoller, P., & Lukin, M. D. (2010). A quantum spin transducer based on nanoelectromechanical resonator arrays. *Nature Physics*, 6(8), 602–608.

[46] Rios, J. M. (2010). *Quantum manipulation of nitrogen-vacancy centers in diamond: from basic properties to applications*. PhD thesis, Harvard University.

[47] Romero-Isart, O. (2011). Quantum superposition of massive objects and collapse models. *Physical Review A*, 84(5).

[48] Romero-Isart, O., Clemente, L., Navau, C., Sanchez, A., & Cirac, J. I. (2012). Quantum magnetomechanics with levitating superconducting microspheres. *Physical Review Letters*, 109(14).

[49] Rothfuß, D., Reiser, A., Fleischmann, A., & Enss, C. (2013). Noise thermometry at ultra low temperatures. *Applied Physics Letters*, 103(5), 052605.

[50] Schäfer-Nolte, E., Schlipf, L., Ternes, M., Reinhard, F., Kern, K., & Wrachtrup, J. (2014). Tracking Temperature Dependent Relaxation Times of Individual Ferritin Nanomagnets with a Wide-band Quantum Spectrometer.

[51] Schmid, S., Malm, B., & Boisen, A. (2011). Quality factor improvement of silicon nitride micro string resonators. *2011 IEEE 24th International Conference on Micro Electro Mechanical Systems*.

[52] Schuetz, M. J. A., Giedke, G., Vandersypen, L. M. K., & Cirac., J. I. (2017). High-fidelity hot gates for generic spin-resonator systems. *Physical Review A*, 95(052335).

[53] Taddei, M. M., Mendes, T. N. C., & Farina, C. (2009). Subtleties in energy calculations in the image method. *European Journal of Physics*, 30, 965–972.

[54] Taminiau, T. H., Cramer, J., van der Sar, T., Dobrovitski, V. V., & Hanson, R. (2014). Universal control and error correction in multi-qubit spin registers in diamond. *Nature Nanotechnology*, 9(3), 171–176.

[55] Tetienne, J., Hingant, T., Kim, J., Diez, L. H., Adam, J.-P., Garcia, K., Roch, J.-F., Rohart, S., Thiaville, A., Ravelosona, D., & Jacques, V. (2014). Nanoscale imaging and control of domain-wall hopping with a nitrogen-vacancy center microscope. *Science*, 344(6190), 1366–1369.

[56] Teufel, J., Donner, T., Li, D., Harlow, J., Altman, M., Cicak, K., Sirois, A., Wittaker, J., Lehnert, K., & Simmonds, R. (2011). Sideband cooling of micromechanical motion to the quantum ground state. *Nature*, 475, 359–363.

[57] Unterreithmeier, Q. P., Faust, T., & Kotthaus, J. P. (2010). Damping of nanomechanical resonators. *Physical Review Letters*, 105(027205).

[58] Weber, B., Mahapatra, S., Ryu, H., Lee, S., Fuhrer, A., Reusch, T. C. G., Thompson, D. L., Lee, W. C. T., Klimeck, G., Hollenberg, L. C. L., & Simmons, M. Y. (2012). Ohm's law survives to the atomic scale. *Science*, 335(6064), 64–67.

[59] Xu, Q., Schmidt, B., Pradhan, S., & Lipson, M. (2005). Micrometre-scale silicon electro-optic modulator. *Nature*, 435(7040), 325–327.

[60] Yuana, M., Cohen, M. A., & Steele, G. A. (2015). Silicon nitride membrane resonators at millikelvin temperatures with quality factors exceeding 108. *Applied Physics Letters*.